

Spring 5-11-2019

# Prediction of Paper Coating Mechanical Behavior Based on Particle-scale Models

Daniel H. Varney

University of Maine, dan.varney@omya.com

Follow this and additional works at: <https://digitalcommons.library.umaine.edu/etd>



Part of the [Chemical Engineering Commons](#)

---

## Recommended Citation

Varney, Daniel H., "Prediction of Paper Coating Mechanical Behavior Based on Particle-scale Models" (2019). *Electronic Theses and Dissertations*. 2997.

<https://digitalcommons.library.umaine.edu/etd/2997>

This Open-Access Thesis is brought to you for free and open access by DigitalCommons@UMaine. It has been accepted for inclusion in Electronic Theses and Dissertations by an authorized administrator of DigitalCommons@UMaine. For more information, please contact [um.library.technical.services@maine.edu](mailto:um.library.technical.services@maine.edu).

**PREDICTION OF PAPER COATING MECHANICAL BEHAVIOR BASED ON  
PARTICLE-SCALE MODELS**

By

Daniel H. Varney

B.S. ChE University of Maine, 1984

A DISSERTATION

Submitted in Partial Fulfillment of the

Requirements for the Degree of

Doctor of Philosophy

(In Chemical Engineering)

The Graduate School

The University of Maine

May 2019

Advisory Committee:

Dr. Douglas W. Bousfield, Professor of Chemical & Biomedical Engineering, Advisor

Dr. Albert Co, Associate Professor of Chemical & Biomedical Engineering

Dr. Douglas J. Gardner, Professor of Forest Operations, Bioproducts, and Bioenergy

Dr. Hemant Pendse, Chairman and Professor of Chemical & Biomedical Engineering

Dr. Mehdi Tajvidi, Associate Professor of Renewable Nanomaterials

**PREDICTION OF PAPER COATING MECHANICAL BEHAVIOR BASED ON  
PARTICLE-SCALE MODELS**

By

Daniel H. Varney

Dissertation Advisor: Dr. Douglas W. Bousfield

An Abstract of the Dissertation Presented  
in Partial Fulfillment of the Requirements for the  
Degree of Doctor of Philosophy  
(In Chemical Engineering)

May 2019

The mechanical properties of pigmented coatings are important for a number of situations; including coated paper, architectural paints, and structures in flexible lithium ion batteries. Coated paper and board undergo a variety of post coating application processes which have the potential to cause serious quality problems such as cracking, picking, and crack-at-the fold (CAF). Because a large number of parameters are known to influence the results, fundamental models are needed to help describe these processes and link them to the coating formulations and to the defects.

A discrete element method (DEM) computer model was developed to describe the pigment level deformation of the coating layer. The model is based on calculating the forces between particles as they move relative to each other and undergo tension or compression. For the case of tension, a non-linear stress-strain relationship was developed that is similar to the behavior seen for pure binder films – data for the pure binder are inputs into the model. In the case of compression, a repulsive force is used that is linear with strain. This thesis is the first time that a DEM was used

to model bending, to include the influence of starch, and to model two coating layers. The model was compared to recent experimental results in the literature for free-standing coating films using different ratios of pigment to binder and also various combinations of latex and starch in the binder systems.

The two dimensional version of the model was set up using uniform spherical particles to represent the paper coating pigments. For both tension and three-point bending, the model was able to predict cracking in accordance with the experimental data. The model's results followed the same trends and were of the same order of magnitude as the lab data. However, differences between the two sets of data did exist, which could be attributed to such causes as issues when making the coating films in the lab, starch impacting the packing, assuming only cohesive failure, the use of spherical particles, and the assumptions made for the simulated packing. The two-dimensional model also was used to simulate the printing event via an out-of-plane tension event and by applying a moving force boundary condition. Picking correlated to both the experiments and the models for the strain-at-failure (STF) and not for the elastic modulus or for the ultimate stress. The two-dimensional model also was applied to two layer coatings. The model agreed with the literature in that the starch-rich layers of high coat weight were more prone to cracking. Furthermore, the two-layer model agreed with pilot and mill results by predicting less cracking with a thick, flexible bottom layer and a thin, stiff top layer.

The three-dimensional model using the packing distribution of uniform spheres, of bimodal size distributions, and of full particle size distributions improved the predictions relative to the two-dimension cases. The results with uniform spheres showed the modulus, maximum stress, and

strain-at-failure to be well predicted except for the maximum stress being underpredicted for cases near the critical pigment volume concentration (CPVC). In addition, the strain-at-failure tended to be overpredicted. When the model used the bimodal and full distributions for packing, the predictions improved. The model overpredicted the modulus and underpredicted the maximum stress, but the predictions were close in some cases, especially when using the full distribution. In addition, the STF showed good agreement between the predictions and the lab data when starch was part of the binder system. Discrepancies still exist between the model predictions and the experimental data, and these differences can be attributed to many factors including the method of packing. The model showed the modulus and the maximum stress to increase directly with the packing density. These results are in accord with the expectation that a tighter initial packing leads to higher local strains, which lead to increased modulus and stress.

## **DEDICATION**

I would like to dedicate this thesis to my wife Andrea and to our daughter Sarah. Without your love, support, and friendship; I would not have had the motivation to pursue this degree. We have had many ups and downs during these last few years, but we have persevered and are stronger as a result. I am very grateful for both of you and am proud to be your husband and your father. In my humble opinion, what is life without a family.

## ACKNOWLEDGEMENTS

I would like to thank first and foremost my advisor Dr. Douglas W. Bousfield. His constant support, encouragement, optimism, and expertise made completion of this thesis possible. The opportunity he gave me to pursue this degree is something for which I will always be grateful. In addition, I would like to express my gratitude to my advisory committee (Dr. Albert Co, Dr. Douglas J. Gardner, Dr. Hemant Pendse, and Dr. Mehdi Tajvidi) for their support and input while I worked on this research project. In addition, I am appreciative of the help and input provided by Dr. Martti Toivakka and Dr. Patrick Gane.

I also would like to extend my thanks to the Paper Surface Science Program industry sponsors. Their financial assistance and suggestions were instrumental to the completion of this work. And, last but not least, I am appreciative of the efforts of those researches whose experimental data was used to validate the model.

# TABLE OF CONTENTS

DEDICATION .....	ii
ACKNOWLEDGEMENTS .....	iii
LIST OF TABLES .....	viii
LIST OF FIGURES .....	ix
LIST OF EQUATIONS .....	xviii
CHAPTER 1 – INTRODUCTION .....	1
1.1 Motivation .....	1
1.2 Objectives .....	1
1.3 Literature Review .....	2
1.4 Basic Concepts of the Model .....	3
1.5 Structure of this Dissertation .....	4
CHAPTER 2 – DISCRETE ELEMENT METHOD TO MODEL IN-LINE TENSION EVENTS FOR SINGLE LAYER TWO DIMENSION SYSTEMS OF UNIFORM SPHERES .....	6
2.1 Abstract .....	6
2.2 Introduction .....	6
2.3 Development of Current DEM Model .....	12
2.4 Comparison of Model to Experimental Data .....	21
2.5 Conclusions .....	30

CHAPTER 3 – DISCRETE ELEMENT METHOD TO MODEL THREE-POINT BENDING EVENTS FOR SINGLE LAYER TWO DIMENSION SYSTEMS OF UNIFORM SPHERES .....	31
3.1 Abstract .....	31
3.2 Introduction .....	31
3.3 Model Description .....	33
3.4 Results and Discussion .....	36
3.5 Conclusions .....	41
CHAPTER 4 – DISCRETE ELEMENT METHOD TO MODEL OUT-OF-PLANE TENSION AND THREE-POINT BENDING EVENTS FOR SINGLE LAYER TWO DIMENSION SYSTEMS OF UNIFORM SPHERES .....	42
4.1 Abstract .....	42
4.2 Introduction .....	42
4.3 Model Development .....	44
4.4 Comparison to Experimental Data .....	53
4.4.1 Bending Simulations .....	54
4.4.2 Picking Simulations .....	60
4.5 Conclusions .....	62
CHAPTER 5 – DISCRETE ELEMENT METHOD TO MODEL THREE-POINT BENDING EVENTS FOR TWO LAYER TWO DIMENSION SYSTEMS OF UNIFORM SPHERES .....	64
5.1 Abstract .....	64
5.2 Introduction .....	64

5.3 Model Development .....	67
5.4 Simulation Results .....	72
5.5 Comparison to Experimental Data .....	78
5.6 Conclusions .....	80
 CHAPTER 6 – DISCRETE ELEMENT METHOD TO MODEL INLINE TENSION AND THREE-POINT BENDING EVENTS FOR SINGLE LAYER THREE DIMENSION SYSTEMS OF UNIFORM SPHERES .....	
	82
6.1 Abstract .....	82
6.2 Introduction .....	82
6.3 Model Description .....	84
6.4 Results .....	92
6.5 Conclusions .....	103
 CHAPTER 7 – DISCRETE ELEMENT METHOD TO MODEL INLINE TENSION AND THREE-POINT BENDING EVENTS FOR SINGLE LAYER THREE DIMENSION SYSTEMS WITH BIMODAL AND FULL PARTICLE SIZE DISTRIBUTIONS OF SPHERICAL PARTICLES .....	
	104
7.1 Abstract .....	104
7.2 Introduction .....	105
7.3 Model Description .....	107
7.4 Particle Size Distributions .....	111
7.5 3D Packings .....	112
7.6 Modeling of In-line Tension and of Three-Point Bending .....	115
7.7 Results – In-line Tension .....	118

7.8 Results – Three-Point Bending .....	125
7.9 Impact of Packing Density on Mechanical Properties .....	131
7.10 Conclusions .....	134
CHAPTER 8 – SUMMARY AND FUTURE WORK .....	136
8.1 Summary .....	136
8.2 Future Work .....	138
REFERENCES .....	140
APPENDIX – CONSIDERATION OF ADHESIVE FAILURE .....	145
BIOGRAPHY .....	148

## LIST OF TABLES

Table 4.1 Properties of the pure binder films from tensile tests .....	54
Table 4.2 Pigment Volume Concentrations (PVC) – original experimental values vs. PVC values when starch is considered as a pigment .....	57
Table 5.1 Properties of the pure binder films from tensile tests .....	73
Table 6.1 Mechanical properties of particle free films composed of mixtures of starch and latex .....	86
Table 7.1 Mechanical properties of particle free films composed of mixtures of starch and latex .....	109

## LIST OF FIGURES

Figure 2.1 Two particles with a connecting binder bridge .....	13
Figure 2.2 The binder bridge volume element for integration .....	13
Figure 2.3 Example initial configurations of particles .....	17
Figure 2.4 Tensile simulation with DEM model .....	18
Figure 2.5 Composite deformation of initial structure .....	19
Figure 2.6 Typical results for $A^*=0.0288$ and $B=34.7$ and a binder with a strain-to-failure of 100% .....	22
Figure 2.7 Elastic Modulus comparison between model and Zhu data over a range of latex percentages of the total binder and with a PVC at the CPVC of 0.635 .....	24
Figure 2.8 Ultimate tensile stress comparison between model and Zhu data over a range of latex percentages of the total binder and with a PVC at the CPVC of 0.635 .....	25
Figure 2.9 Strain-to-failure comparison between model and Zhu data over a range of latex percentages of the total binder and with a PVC at the CPVC of 0.635 .....	25
Figure 2.10 Elastic modulus and ultimate tensile comparison between model and Zhu data over a range of latex percentages of the total binder and with a PVC near 0.4 .....	26
Figure 2.11 Elastic modulus and ultimate tensile comparison between model and Zhu data over a range of latex percentages of the total binder and with a PVC near 0.8 .....	27
Figure 2.12 Elastic modulus comparison between model and Raman data (for the one latex used in her study) .....	28
Figure 2.13 Elastic modulus reported by Prall (2000) and the model predictions .....	29

Figure 3.1 Typical bending simulation showing grip particles and particles that will move upward .....	35
Figure 3.2 Bending results of a coating layer with $A^*=0.03$ , $B=34.7$ , and strain-to-failure of 24% .....	37
Figure 3.3 Force on left and right grip particles as a function of bending strain for the conditions in Figure 3.2 .....	37
Figure 3.4 Similar to Figure 3.2 but grip particles are not allowed to move in either the x or y directions .....	38
Figure 3.5 Similar to Figure 3.3 but for grip particles not allowed to move in either the x or y directions .....	38
Figure 3.6 Final result for a low PVC case (left) and high PVC case (right), top are high starch content and bottom are pure latex, using parameters from Zhu <i>et al.</i> (2014) .....	39
Figure 3.7 Flexural stress verse strain for binder properties of $A=1.6$ , $B=2$ , and strain-to-failure of 200% .....	41
Figure 4.1 Typical nonlinear response from tension simulation [Varney & Bousfield (2016a)] .....	45
Figure 4.2 Boundary conditions for a bending simulation. ....	46
Figure 4.3 Picking simulation by applying an out-of-plane velocity in the pull up zone .....	48
Figure 4.4 Conditions to simulate the exit of a printing nip .....	49
Figure 4.5 Typical bending results for 62 PVC (20pph binder) for binder properties that resemble 40% latex and 60% starch .....	50
Figure 4.6 Typical results of the picking simulation for pure latex binder properties and PVC of 62 (20 pph binder) .....	51

Figure 4.7 Typical picking results when the ends of the coating layer are fixed for similar binder properties as in Figure 4.6 .....	52
Figure 4.8 Results for two binder systems at various net displacements .....	53
Figure 4.9 Flexural modulus as a function of the latex content of the binder system for two pigment volume concentrations .....	55
Figure 4.10 Maximum stress as a function of the latex content of the binder system at two pigment volume concentrations .....	55
Figure 4.11 Strain-at-failure as a function of the latex content of the binder for two pigment volume concentrations .....	56
Figure 4.12 Flexural modulus as a function of the latex content of the binder system for two pigment volume concentrations and with starch as a pigment (62 PVC corresponds to 20 parts of binder and 78 PVC corresponds to 10 parts of binder) .....	58
Figure 4.13 Maximum stress as a function of latex content of the binder system for two pigment volume concentrations and with starch as a pigment (62 PVC corresponds to 20 parts of binder and 78 PVC corresponds to 10 parts of binder) .....	58
Figure 4.14 Strain-at-failure as a function of latex content of the binder system for two pigment volume concentrations and with starch as a pigment (62 PVC corresponds to 20 parts of binder and 78 PVC corresponds to 10 parts of binder) .....	59
Figure 4.15 Maximum dimensional picking stress against pull up zone width for four binder systems .....	61
Figure 4.16 Maximum dimensionless picking stress against pull up zone width for four binder systems .....	61
Figure 5.1 Typical non-linear response from tension simulation [from Varney and	

Bousfield (2016a)] .....	68
Figure 5.2 Boundary conditions for a bending simulation .....	69
Figure 5.3 Typical results for 62 PVC (20 pph binder) with binder properties that resemble 60% latex and 40% starch in the top layer and 80% latex and 20% starch in the bottom layer .....	72
Figure 5.4 Simulated flexural modulus as a function of the bottom layer height and various bottom layer/top layer binder systems .....	74
Figure 5.5 Simulated maximum stress as a function of the bottom layer height and various bottom layer/top layer binder systems .....	74
Figure 5.6 Simulated strain-at-failure as a function of the bottom layer height and various bottom layer/top layer binder systems .....	75
Figure 5.7 Position plot for 62 PVC (20 pph binder) with binder properties that resemble 100% latex in the bottom layer (100L/0S) and 60% latex plus 40% starch in the top layer (60L/40S) .....	77
Figure 5.8 Position plot for 62 PVC (20 pph binder) with binder properties that resemble 60% latex plus 40% starch in the bottom layer (60L/40S) and 100% latex in the top layer (100L/0S) .....	77
Figure 5.9 Position plot for 62 PVC (20 pph binder) with binder properties that resemble 60% latex plus 40% starch in the bottom layer (60L/40S) and 80% latex plus 20% starch in the top layer (80L/20S) .....	78
Figure 5.10 Position plot for 62 PVC (20 pph binder) with binder properties that resemble 60% latex plus 40% starch (60L/40S) in a single layer (i.e., one starch rich layer equal in height to the two-layer scenarios) .....	78

Figure 6.1 Idealized system of two spherical pigments connected together by a binder bridge .....	86
Figure 6.2 Near neighbor criteria with $R_n=1.0$ .....	87
Figure 6.3 Simulation set up for the 2D model for the three point bending case for 30x300 matrix (the particles are pushed up from the bottom in the “push up” zone) .....	89
Figure 6.4 3D situation for uniform spheres packed in a 10x10x100 cell .....	89
Figure 6.5 Flexural strain and stress predicted by the simulation (left) and crack of the coating layer (right) for a 2D example .....	91
Figure 6.6 Bending deformation in 3D mode, showing the connections between particles for a typical case .....	92
Figure 6.7 Flexural modulus vs. C-factor at various values of damping factor using monodisperse spherical particles .....	93
Figure 6.8 Flexural maximum stress vs. C-factor at various values of damping factor using monodisperse spherical particles .....	93
Figure 6.9 Flexural strain at failure vs. C-factor at various values of damping factor using monodisperse spherical particles .....	94
Figure 6.10 Elastic modulus of coating layers in tension for PVC = 63% for various values of the starch and latex content in the binder system .....	95
Figure 6.11 Predictions of the stress at failure for the coating layers in tension for PVC = 63% for various levels of latex and starch in the binder system .....	96
Figure 6.12 Predictions of the stress at failure for the coating layers in tension for PVC = 63% for various levels of latex and starch in the binder system .....	96
Figure 6.13 Predicted and measured flexural modulus for the coating layer near PVC of 63% for binder components of various levels of starch and latex .....	97

Figure 6.14 Maximum stress at failure for coating layers near PVC of 63% for various levels of latex and starch in the binder composition .....	98
Figure 6.15 Predicted and measured strain at failure for coating layers near PVC of 63% for various levels of latex and starch in the binder composition .....	98
Figure 6.16 Flexural modulus predictions and experimental results of Najafi <i>et al.</i> (2018) .....	99
Figure 6.17 Maximum stress predictions for two different PVC values and the predictions .....	100
Figure 6.18 The strain at failure predictions and data for two PVC values .....	100
Figure 6.19 Comparison of $R_n$ value on model modulus predictions for the PVC 63% case .....	101
Figure 6.20 Comparison of model predictions for maximum stress for two values of $R_n$ .....	102
Figure 6.21 Comparison of predictions of strain at failure for two values of $R_n$ .....	102
Figure 7.1 Idealized system of two spherical pigments connected together by a binder bridge .....	107
Figure 7.2 Near neighbor criteria with $R_n = 1.0$ .....	110
Figure 7.3 Void fraction of bimodal mixes as a function of size ratio and of volume fraction of large constituent [from Brouwers (2011)] .....	112
Figure 7.4 Representation of bimodal distribution of spherical particles with 50% large particles and small particle radius of 0.2 (large diameter is always 1.0) .....	113
Figure 7.5 Representation of bimodal distribution of spherical particles with 50% large particles and small particle radius of 0.3 (large diameter is always 1.0) .....	113
Figure 7.6 Representation of bimodal distribution of spherical particles with 50% large particles and small particle radius of 0.4 (large diameter is always 1.0) .....	113
Figure 7.7 Representation of bimodal distribution of spherical particles with 65% large particles and small particle radius of 0.2 (large diameter is always 1.0) .....	113

Figure 7.8 Representation of bimodal distribution of spherical particles with 65% large particles and small particle radius of 0.3 (large diameter is always 1.0) .....	114
Figure 7.9 Representation of bimodal distribution of spherical particles with 65% large particles and small particle radius of 0.4 (large diameter is always 1.0) .....	114
Figure 7.10 Representation of bimodal distribution of spherical particles with 80% large particles and small particle radius of 0.2 (large diameter is always 1.0) .....	114
Figure 7.11 Representation of bimodal distribution of spherical particles with 80% large particles and small particle radius of 0.3 (large diameter is always 1.0) .....	114
Figure 7.12 Representation of bimodal distribution of spherical particles with 80% large particles and small particle radius of 0.4 (large diameter is always 1.0) .....	115
Figure 7.13 Representation of full distribution of spherical particles approximating a narrow particle size GCC (93 w/w% < 2.0 microns) .....	115
Figure 7.14 Representation of full distribution of spherical particles approximating a broad particle size GCC (60 w/w% < 2.0 microns) .....	115
Figure 7.15 3D situation for uniform spheres packed in a 10x10x100 cell .....	116
Figure 7.16 Bending deformation in 3D mode, showing the connections between particles for a typical case for monodisperse spheres .....	118
Figure 7.17 Elastic modulus of coating layer for in-line tension at PVC = 63% and with the 77L/23S binder system .....	120
Figure 7.18 Maximum stress of coating layer for in-line tension at PVC = 63% and with the 77L/23S binder system .....	121
Figure 7.19 Strain-at-failure of coating layer for in-line tension at PVC of 63% and with the 77L/23S binder system .....	122

Figure 7.20 Elastic modulus comparison between Zhu and the model at two PVCs (in-line tension) .....	123
Figure 7.21 Maximum stress comparison between Zhu and model at two PVCs (in-line tension) .....	124
Figure 7.22 Strain-at-failure comparison between Zhu and model at two PVCs (in-line tension) .....	125
Figure 7.23 Predicted and measured flexural modulus for the coating layer near PVC of 63% for binder components of various levels of starch and latex (three-point bending) .....	126
Figure 7.24 Predicted and measured flexural maximum stress for the coating layer near PVC of 63% for binder components of various levels of starch and latex (three-point bending) .....	127
Figure 7.25 Predicted and measured strain at failure for coating layers near PVC of 63% for various levels of latex and starch in the binder composition (three-point bending) .....	128
Figure 7.26 Flexural modulus predictions and experimental results of Najafi at two PVCs (three-point bending) .....	129
Figure 7.27 Maximum stress predictions for two different PVC values and the predictions (three-point bending) .....	130
Figure 7.28 The strain at failure predictions and data for two PVC values (three-point bending) .....	131
Figure 7.29 Modulus vs. packing density (in-line tension and three-point bending) .....	132
Figure 7.30 Maximum stress vs. packing density (in-line tension and three-point bending) .....	133
Figure 7.31 Strain-at-failure vs. packing density (in-line tension and three-point bending) .....	134

Figure A.1 Flexural modulus comparison between data of Najafi and the model for various AFF values (three-point bending) .....146

Figure A.2 Maximum stress comparison between data of Najafi and the model for various AFF values (three-point bending) .....146

Figure A.3 Strain-at-failure comparison between data of Najafi and the model for various AFF values (three-point bending) .....147

## LIST OF EQUATIONS

Equation 2.1 Particle force balance .....	10
Equation 2.2 Stress/strain relationship defining modulus .....	11
Equation 2.3 Strain definition .....	11
Equation 2.4 Stress/strain relationship defining viscosity.....	11
Equation 2.5 Hooke's Law .....	12
Equation 2.6 Spring constant .....	12
Equation 2.7 Height of binder bridge .....	14
Equation 2.8 Volume of binder bridge .....	14
Equation 2.9 Binder bridge radius .....	15
Equation 2.10 Cross sectional area of binder bridge .....	15
Equation 2.11 Nonlinear stress/strain relationship for tension .....	15
Equation 2.12 Nonlinear tension contact force .....	16
Equation 3.1 Nonlinear tension contact force .....	33
Equation 3.2 Compression repulsive force .....	34
Equation 3.3 Flexural stress .....	35
Equation 3.4 Flexural strain .....	35
Equation 4.1 Nonlinear tension contact force .....	44
Equation 4.2 Compression repulsive force .....	45
Equation 4.3 Flexural stress .....	47
Equation 4.4 Flexural strain .....	47
Equation 5.1 Nonlinear tension contact force .....	67

Equation 5.2 Compression repulsive force .....	68
Equation 5.3 Flexural stress .....	70
Equation 5.4 Flexural strain .....	70
Equation 6.1 Nonlinear tension contact force .....	84
Equation 6.2 Binder bridge radius .....	85
Equation 6.3 Time integrations .....	90
Equation 6.4 Flexural stress .....	90
Equation 6.5 Flexural strain .....	90
Equation 7.1 Nonlinear tension contact force .....	108
Equation 7.2 Binder bridge radius .....	108
Equation 7.3 Time integrations .....	117
Equation 7.4 Flexural stress .....	117
Equation 7.5 Flexural strain .....	117

# **CHAPTER ONE**

## **INTRODUCTION**

Theoretical models can provide a fundamental understanding of phenomena that can lead to improved processes and products reducing the need for experimental work. If the model's development is based on sound physics or chemistry and on reasonable assumptions, then it should be able to simulate real world physical events with a respectable level of accuracy. The goal of this thesis work is to develop a model to predict the deformation behavior of coating layers and, as a consequence, expand the fundamental understanding of these events.

### **1.1 Motivation**

Coating failure during post application steps is a serious quality problem for the paper maker and for the printer. Whether the issue is cracking-at-the-fold (CAF) or picking during printing, the final result is a poor quality print job that can potentially result in both lost business and reduced revenues. The development of a computer model which can provide fundamental understanding of why the various failure events occur could provide the industry with another set of tools to avoid or to minimize such problems in the future. In addition, the proper balance between final print quality and cost of the coated paper could be even more achievable and could lead to an even better performance/cost ratio.

### **1.2 Objectives**

The goal of this thesis is to develop a computer model based on the discrete element method (DEM) that will simulate in-line tension, out-of-plane tension, and bending deformation events. This research will be performed for single coating layers as well as for double layer systems and

will focus on spherical particles. The use of the DEM to model bending and the simulation of two layers would be new developments. The model would predict the onset of failure based on coating mechanical properties and based on using inputs from pure binder films. Using such inputs also was a novel approach as was modeling binders comprised of both latex and starch.

### **1.3 Literature Review**

A detailed literature review is not given here because each chapter reviews various aspects of past work. A key point is that DEM and the finite element method (FEM) have been used in the past to describe paper coatings in a limited way. The FEM has been used to model tension, compression, and bending events but not at the particle scale possible with the DEM. In the case of the discrete element method, it has been used to simulate tension and compression events, but not bending scenarios. The FEM treats the paper and coating as a composite material that has some elastic modulus, not as the individual moduli of the pigments and of the binder as does the DEM. The complexity of the various models ranged from particles represented by simple spheres to particles representing platy type structures.

The experimental work covered the spectrum from lab scale, to the pilot coater, and to production coater trials. The lab work would involve making free standing coating films with a simple coating of pigment and of binder. In most cases, the pigments had aspect ratios close to one and the binder was composed only of latex. Some groups included starch as part of the binder package as well.

The DEM model of this thesis was compared to the experimental work of two groups. These sources and their lab data are plotted against the model results as seen in the subsequent chapters.

## 1.4 Basic Concepts of the Model

The computer model is based on the discrete element method (DEM) and uses simple constitutive equations to solve force balances around individual particles, which are represented by spheres. Each particle is connected to its neighbors via a binder bridge, with a radius determined to be a function of the Pigment Volume Concentration (PVC). The typical means of representing the bridge is as a spring and dashpot, but the later term is not included in the model at this time.

Two force equations are the basis for the model. If two particles move apart compared to the initial separation, a tension force is applied to each particle in the opposite direction of displacement. The tension equation is a non-linear form of the stress/strain experimental data for the binder as seen in the literature. The coefficients in this equation are based on mechanical data obtained from pure binder films. When in tension mode, if the simulated strain is greater than the strain-at-failure of the pure binder film, then failure is assumed to be occurring and the force goes to zero. As for the compression forces, these are needed to keep particles from overlapping. At every time step, the net force is calculated for each particle. Using Newton's law of motion, this force is used to update velocity and position of every particle using a numerical integration.

Two cases of most interest involve tensile deformation and bending. In the tensile case, one group of particles on one end of the domain are set to move with a known velocity. Another group of particles on the other end of the domain are not allowed to move. The net effect is that the particles/binder matrix will see a tensile deformation. In bending, this scenario is similar except that one group of particles are set to move out of plane, and two other groups of particles are set to not deform out of plane.

In both cases; the modulus, maximum stress, and strain-at-failure (STF) are obtained from the simulation data. The modulus represents the slope of the stress/strain curve close to the zero strain point. The maximum stress is the high point of the curve near where the strain begins to decrease for good. This later point represents failure which, in the model, is when the binder bridge between two particles fails, or breaks, cohesively. This type of failure is one of the assumptions made to simplify the model.

### **1.5 Structure of this Dissertation**

The sequence of the chapters shows the evolution of the model's complexity and are built from papers that have been published or will be submitted soon. Chapter 2 discusses the 2D modeling of in-line tension and was presented at PaperCon 2016. In Chapter 3, the model is expanded to simulate three-point bending, which is the first time the DEM was used in this regard. This work was presented at the 2016 Advanced Coating Fundamentals Symposium and is compared to the data obtained for bending by Najafi *et al.* (2018). Chapter 4 continues the model's development as not only is three-point bending simulated again but also an out-of-plane picking and a novel moving force/velocity picking type event is simulated. This paper was presented at PaperCon 2017 and gives insight with regard to the mechanical parameters that are important in picking. In Chapter 5, three-point bending is applied to two coating layer systems, where each layer has a different binder system; these predictions were compared to crack area of double coated samples of Najafi *et al.* (2019). Chapter 6 expands the model to three-dimensions for both in-line and three-point bending. This work has been accepted for presentation at PaperCon 2019 and compares the model predictions to experiments and to the 2D case. Chapter 7 expands the model from uniform spherical particles representing the pigments to two cases where the particle sizes are either bimodal or full

distributions of spheres. The simulations in these cases are applied to in-line tension and to three-point bending deformation events. This chapter is pending publication at this point. Lastly, Chapter 8 briefly summarizes the entire thesis and the appendix reviews some of the data generated when considering adhesive failure.

As a consequence of using various publications as the basis for the chapters, some of the material is a bit repetitive. The literature reviews and the model descriptions are quite similar in a number of the chapters. The best overview of the model development and the accompanying literature review is given in chapter three while chapters six and seven give thorough descriptions of the expansion of the model to three-dimensions. Ultimately, the purpose and work of each chapter is unique as is the comparison with model predictions and the experimental data.

## CHAPTER TWO

### DISCRETE ELEMENT METHOD TO MODEL IN-LINE TENSION EVENTS FOR SINGLE LAYER TWO DIMENSION SYSTEMS OF UNIFORM SPHERES

#### 2.1 Abstract

The mechanical properties of coated papers can have a significant impact on how well they survive post coating application steps. Processes such as calendering, printing, and folding can cause the following quality problems respectively: cracking, picking, and crack-at-the fold (CAF). The Discrete Element Method (DEM) has the potential to describe the mechanics of the coating layer on a microscopic scale. Recent models have given insight into the strength properties of coatings, but a good comparison with experimental results is lacking.

In this paper, a DEM model is improved to account for the non-linear deformation behavior seen with most binders. In addition, a new method to convert the latex volume fraction to a latex bridge radius is proposed. The model results are compared to recent in-plane tension type experimental data in the literature that include starch-latex mixtures. The elastic modulus, ultimate tensile stress, and strain-to-failure compare well with the experimental results.

#### 2.2 Introduction

A variety of forces are applied to coated paper and paperboard during production, converting, and printing of these substrates that can have an adverse impact on the final product quality. After coating application and drying, the paper is compressed during calendering to improve the smoothness of the sheet and to increase the final gloss. The coated paper experiences compressive forces and tensional forces during offset printing. The folding step can lead to a paper quality issue

termed crack-at-the-fold (CAF) if the right balance of paper and coating mechanical properties is not achieved.

Understanding these mechanical properties is important to the papermaker and to the coating formulator. The proper balance of these mechanical properties must be achieved to avoid issues such as picking and such as CAF. The work presented in this paper will focus on tension deformation events. The goal is for the model eventually to simulate compression as well as bending type situations.

Several groups have conducted experiments evaluating the tensile strength of free standing coatings layers or discs [Alam (2010), Fern *et al.* (2012), Husband *et al.* (2006, 2007a, 2007b, 2008, 2009, 2010), Lazarus *et al.* (2012), Nutbeem *et al.* (2010), Okomori and Lepoutre (1998), Prall *et al.* (2000), Prall (2000), Raman *et al.* (1998), Touaiti *et al.* (2010), Touaiti (2013), Zhu *et al.* (2014)]. This work showed the importance of the two main components of formulations, the pigment system and the binder package, in determining the mechanical properties. As for the pigments, the size; shape; and particle size distribution were found to be critical variables in this regard. The important aspects of the binder were the amount and the glass transition temperature. And, when taking all of these parameters in combination, the pigment volume concentration (PVC) was seen to impact coating strength as well.

The data from three investigations in particular have been used in confirming the current model's predictive ability. Raman *et al.*'s (1998) work involved tensile testing of unsupported coating films. The elastic modulus, the tensile strength, and the strain-to-failure were tested for a wide range of

PVCs. A standard styrene butadiene latex and a spherical plastic pigment were used to make the coating films, which were cut in to a “dog bone” shape for testing. Her most interesting finding was that the elastic modulus and tensile strength both experienced sudden increases in values near the critical pigment volume concentration (CPVC) while the strain-to-failure results were just the opposite. One possible issue confounding the data was the drying temperature used to prepare the films might have been too close to the glass transition temperature of the plastic pigment, possibly causing some of these particles to fuse.

In Prall’s PhD thesis (2000), the viscoelastic behavior of three pigment systems over a range of pigment volume concentrations was studied. Free standing films were prepared via drawdowns using plastic pigment, rhombohedral precipitated calcium carbonate (R-PCC), and clay. Two styrene butadiene (SB-type) lattices of differing degrees of carboxylation were used in this study. The traditional “dog bone” shaped film strip was measured in a dynamic mechanical thermal analyzer (DMTA) using tensile mode to determine the viscoelastic response. The results showed that the tensile strength and the elastic modulus increased directly with PVC until the critical PVC (CPVC) was reached, then decreased beyond that critical point [as did Raman *et al.* (1998)]. In contrast, the elongation-at-break decreased continuously over the range of PVCs studied. Prall did not see the rapid change in properties at the CPVC as did Raman.

Zhu *et al.* (2014) studied the mechanical properties of free-standing coating films, focusing on the impact of starch in a dual binder system with latex over a wide range of binder levels, thus, covering a broad spectrum of PVCs. A series of coatings comprised of GCC (60% < 2  $\mu\text{m}$ ) and of starch and latex were prepared. The trends seen for elastic modulus, ultimate tensile strength, and

elongation-at-break as the PVC increased were the same seen by Prall (2000). When increasing levels of starch were used, the elastic modulus and ultimate tensile strength increased while the elongation-at-break decreased significantly.

All of these various investigators have modeled the mechanical properties of paper coatings in an attempt to predict failure. They have used key parameters such as elastic modulus, strain-to-failure, and maximum stress as inputs to their models. Two approaches historically have been taken when developing these models – the Finite Element Method (FEM) and the Discrete Element Method (DEM).

The finite element method treats the coating layer as a continuum and solves for the stress and for the displacement. A good example is the work of Barbier *et al.* (2005), where the crack-at-the-fold was predicted based on some global values for elastic modulus and for strain-to-failure. The FEM does not go down to the particulate level as does the DEM, but instead, the former method deals more from a macroscopic viewpoint. The finite element method treats the paper and coating as a composite material that has some elastic modulus, not as the individual moduli of the pigments and of the binder as does the DEM.

The discrete element method concerns itself with computing the motion of an individual particle within a cluster of particles and it takes in to account the interactions between the various neighboring particles. The method allows for the understanding of macroscopic events based on microscopic phenomena and was developed back in the early 1970s.

This approach is similar to molecular dynamics and involves solving Newton’s second law of motion for the forces acting on particle  $i$  by all neighboring particles  $j$ . This formula has the following general form:

$$\frac{m_i d^2 x_i}{dt^2} = F_{gravitational,i} + F_{bouyant,i} + F_{drag,i} + \sum_{j \neq i} F_{contact,ij} \quad (2.1)$$

where  $m_i$  is the mass of particle  $i$  and  $x_i = (x_i, y_i, z_i)$  are the coordinates of its center of gravity. The forces on the right side of this equation represent the gravitational, the buoyant, the drag, and the contact forces acting on particle  $i$ . Some researchers combine the buoyant, drag, pressure gradient, lubrication and lift forces in to one term called “hydrodynamic” force. The rotational motion of each particle can be obtained through an angular momentum balance using this same equation. The integration time steps are chosen to be small enough in an attempt to achieve stable calculations. In addition, the net force acting on a particle depends only on the particles in which it is in contact, meaning that the first three force terms on the right side of the equation are assumed to be small enough to ignore in the calculations. Another reason for dropping these three forces is that the coatings considered in this study are dry, meaning that no fluid exists that would allow the particles to flow past each other.

A common means of evaluating the contact between two particles or, in particular, the contact force term, is by using the spring-and-dashpot model. This approach is a good representation of the binder which connects the pigment particles in the DEM model. Viscoelastic materials (such as paper coating binders) undergoing stress are modeled quite often using these mechanical components. The springs represent the elastic (restorative) element while the dashpot represents

the viscous (dampening) element of the binder. Some of the models incorporating these two components include the Maxwell Model (spring and dashpot are in series), the Kelvin-Voigt Model (both are in parallel), and the standard linear solid model (a spring is in parallel with a linear arrangement of a spring and dashpot). Springs obey Hooke's Law by the equation to follow:

$$\sigma = E\varepsilon \quad (2.2)$$

where  $\sigma$  is the applied stress,  $\varepsilon$  is the resulting strain, and  $E$  is the Young's Modulus of the material. The strain term is defined as follows:

$$\varepsilon = (h_o - h)/h_o \quad (2.3)$$

where  $h$  is the current distance between pigment surfaces and  $h_o$  is the original gap distance. This equation shows the importance of particle packing on the strain experienced by the binder bridge connecting two particles and, therefore, on the subsequent force relationship. For the dashpot, the equation relating stress and strain is represented below.

$$\sigma = \eta \frac{d\varepsilon}{dt} \quad (2.4)$$

where  $\eta$  is the viscosity. The model of this paper is comprised of a spring and a dashpot in parallel with each other, but the dashpot component is not being used at present (as some of the deformations events being simulated are at very fast rates anyway – e.g., printing and folding).

Three groups have used the DEM to simulate tension events with paper coatings [Alam *et al.* (2012), Toivakka and Bousfield (2001), Toivakka *et al.* (2014)]. DEM models have focused only on tension and on compression type deformations even though they should be able to predict bending events as well. One group that has looked at modeling compression events with the DEM is Azadi *et al.* (2008a, 2008b).

In this paper, the model of Toivakka and Bousfield (2001) is updated to include a non-linear spring type interaction between pigments. The proposed non-linear model has advantages compared to past non-linear models. In addition, a new method to convert the pigment volume concentration (PVC) to various parameters in the model is proposed. The model predictions are compared to data that is in the literature [Raman *et al.* (1998), Prall (2000), Zhu *et al.* (2014)].

### **2.3 Development of Current DEM Model**

The interaction force between two particles is based on Hooke's Law for linear springs and has the form

$$F = k\varepsilon \tag{2.5}$$

where  $k$  is the spring constant of the binder between the two particles, and  $\varepsilon$  is the strain. The spring constant term  $k$  is related to the elastic modulus  $E$  of the binder via:

$$k = E \cdot A_b \tag{2.6}$$

where  $A_b$  is the cross-sectional area of the binder bridge between two particles (see Equation 2.10). As such, the spring constant is dependent on the amount of binder via the area term. The total binder in the matrix is equal to the sum of the volume of each binder bridge. These individual volumes are a function of the initial gap between the particles (before any external forces are applied) and of the binder bridge radius. The pictures below (Figures 2.1 and 2.2) depict this scenario, where the second schematic represents a volume element within the binder bridge.

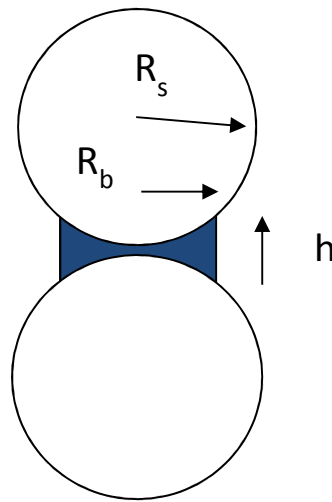


**Figure 2.1 Two particles with a connecting binder bridge**

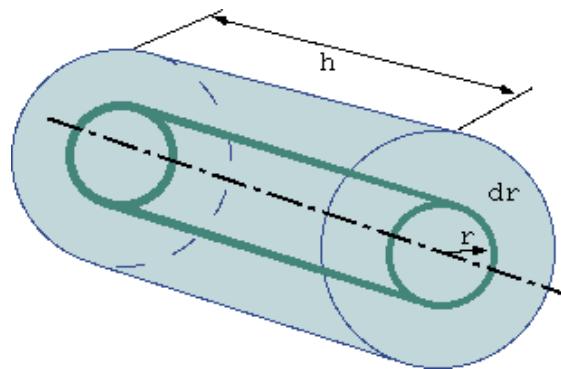


**Figure 2.2 The binder bridge volume element for integration.**

The terms in the two pictures are as follows:

- $R_s$  is the radius of the sphere representing the particle
- $R_b$  is the radius of the binder bridge
- $h$  is the height of the binder bridge as a function of the radius
- $dr$  is the width of the volume element within the binder bridge.

The height term  $h$  can be calculated from geometry between two touching spheres, with the final form given below.

$$h = 2R_s - 2(R_s^2 - r^2)^{0.5} \quad (2.7)$$

The volume of the binder bridge can be obtained by integrating the term  $2\pi rh$  (which equals the area of the circumference) from  $r = 0$  to  $r = R_b$  (the width of the volume element). The final form of this equation is the following:

$$v_b = 2\pi R_b^2 R_s - 4\pi(R_s^3 - (R_s^2 - R_b^2)^{1.5})/3 \quad (2.8)$$

While the radius  $R_s$  of the spheres is known from the average particle size, the binder radius has been found to correlate quite well with the pigment volume concentration (PVC). Below the critical PVC, the binder radius is equal to the particle radius (i.e.,  $R_b = R_s$ ) as the particles are completely surrounded by the binder. When the PVC is above the critical value, the binder bridge radius for the cylindrical volume element was found to correlate strongly ( $r^2 = 0.99$ ) with the PVC

when  $R_b$  is raised to the fourth power. Equation (2.8) was found to follow the relationship for PVC as

$$R_b = (3.1 - 3.1*PVC/100)^{0.25} \quad (2.9)$$

Additionally, it follows that the cross-sectional area of the binder bridge is

$$A_b = \pi R_b^2 \quad (2.10)$$

In summary, above the CPVC, the binder bridge radius, and thus the area of the binder bridge and the spring constant, should decrease according to equation (2.8). Below CPVC, the binder bridge radius is always taken as the particle radius. The notion of relating the amount of binder to the PVC also was suggested in Do-Ik Lee's (1998) work when he related binder shrinkage to the volume fraction of pigment. This prior work also presents a good "picture" of the situation with binder and pigments at the CPVC.

The binder of typical paper coatings has been shown to behave in a non-linear manner in simple tensile tests [(Raman *et al.* (1998), Prall (2000), and Zhu *et al.* (2014)]. Thus, if the interaction force between two particles is a nonlinear function, the mechanical response will also be nonlinear. It was found that the stress-strain behavior of the pure binder follows the expression

$$\sigma = A(1 - e^{-B\varepsilon}) \quad (2.11)$$

where A and B are constants adjusted to fit the pure binder data. Based on taking the derivative of stress with respect to strain and setting strain to zero, the initial slope of this curve is A\*B, which must equal E, the elastic modulus. The ultimate tensile stress of the pure binder is the constant A. Therefore, the advantage of using this expression is that the parameters A and B can be obtained from data for the elastic modulus and for the ultimate tensile stress of the pure binder. The contact force between two particles then is the stress calculated by equation (2.11) times the binder area, or as

$$F = A(1 - e^{-B\varepsilon})\pi R_b^2 \quad (2.12)$$

The third value that comes from the pure binder case is the strain-to-failure, the deformation that the binder can undergo before it breaks. For pure latex systems, this can be over 400%. When starch is mixed with latex, Zhu *et al.* (2014) report that the strain-to-failure decreases. In the model, if the strain is larger than the strain-to-failure of the binder, the force between particles is set to zero. This would simulate the propagation of a crack.

The constants A and B might be functions of the deformation rate of the experiments as they currently have been based on the slow rates used in the literature [Raman *et al.* (1998), Prall (2000), and Zhu *et al.* (2014)]. If different rates of strain are of interest, these values will have to be adjusted to predict tension-related deformation event under these conditions. Also, in the model, these input parameters are made dimensionless. The parameter B is already dimensionless, but the parameter A is made dimensionless with the elastic modulus of the binder as  $A^* = A/E$ .

The model starts with a structure of monodisperse spheres that are placed in a two-dimensional, randomly packed layer. Figure 2.3 shows two examples of initial structures. The program to pack these spheres is similar to other codes, but simply applies a small downward force on the particles to get them into a structure. For cases below the CPVC, the particles are widely separated. The cases in Figure 2.3 should represent cases at or above the CPVC.

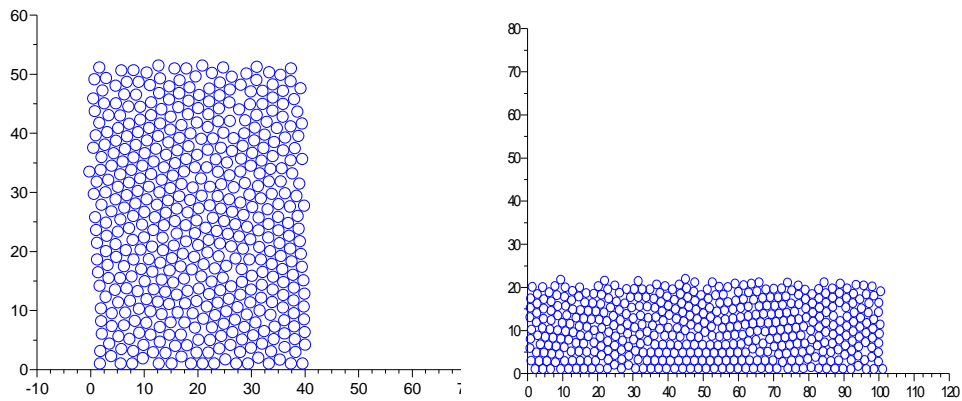


**Figure 2.3 Example initial configurations of particles.**

To simulate a tensile test, a group of particles on one edge of the domain is set to a known velocity. All particle velocities are normalized to this velocity. For example, for the left picture in Figure 2.3, particles that have positions larger than 35 units are set to a dimensionless velocity of one in the positive-x direction. Particles that have positions less than 5 units, are set to zero velocity. Particle positions and velocities between these two groups will be calculated in the model. The motion of the particles on the right will cause a local strain between these particles and the particles near them. This strain results in a force on those particles. The force leads to a velocity and a displacement of those particles. Figure 2.4 shows an example of a tensile simulation. Another way

to view the deformation is in Figure 2.5, showing the position of the particles at a number of different times.

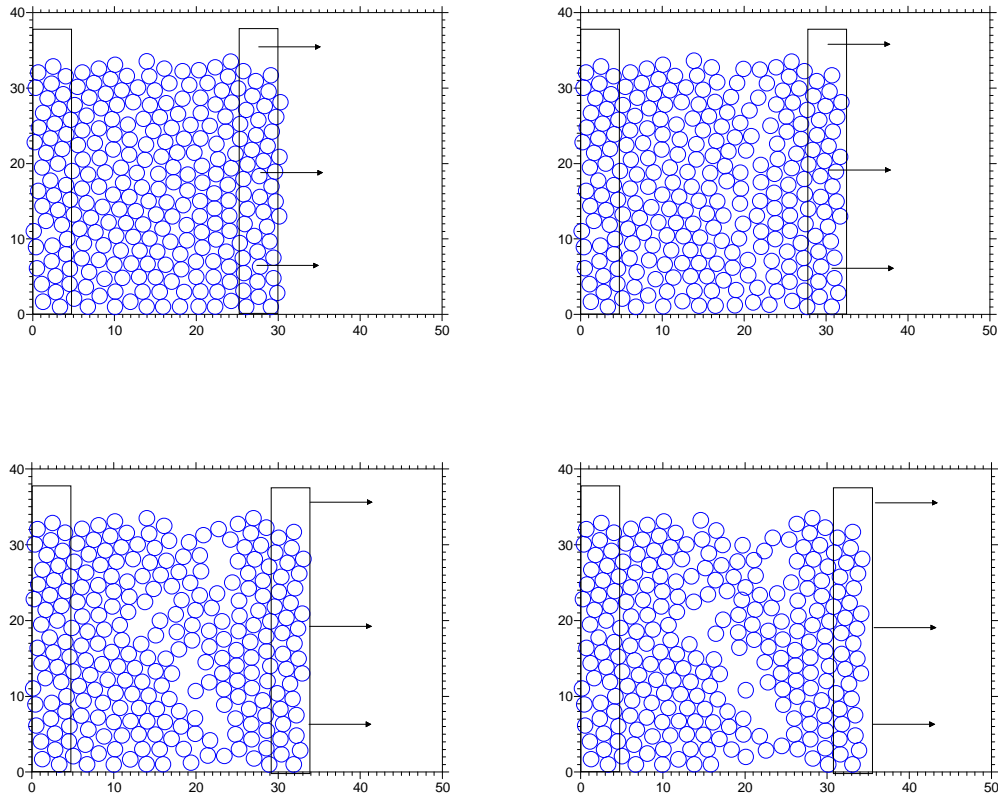


**Figure 2.4 Tensile simulation with DEM model. Crack can form at any location as spheres are pulled apart.**

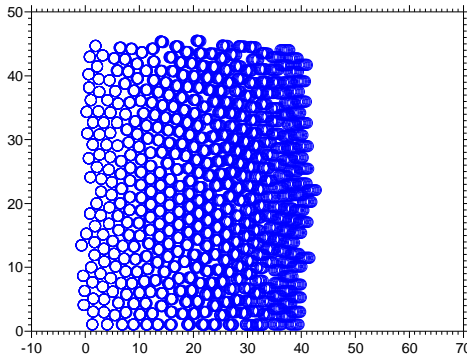


**Figure 2.5 Composite deformation of initial structure.**

The force between every particle pair that is within a distance criteria of four radii is calculated at every time step using equation (2.12). The  $x$  and  $y$  components of that force are added to each particle. The force in each direction determines the acceleration of the particle in both directions. A Euler time integration method is used to update velocity and position of each particle. The total stress is calculated by adding the force on the particles that are held to zero velocity divided by the area of the cross section. This area is the height of the simulation cell multiplied by the particle diameter. The strain is calculated by the displacement of the moving particles divided by the initial distance between these particles and the particles that are held stationary.

There are a number of assumptions associated with this model. Currently, the model does not include the dashpot terms. Therefore, the rate of deformation is not taken into account, meaning that all deformations are assumed to occur at the rate that the pure binder film modulus was measured. In addition, the adhesion of the latex to the particles is assumed to be perfect. However, in some conditions, it is expected that the binder can break from the pigment. This assumption can

be addressed by putting some stress criteria for the binder-pigment adhesion. Finally, real coating layers have a distribution of particle sizes, while at this point, uniform spheres are used as a starting point. And, for cases below the CPVC, the assumption is made that there are no air voids.

One way to scale the results to account for a particle size distribution involves the concentration of particles. Figure 3 shows particles that are tightly packed into the initial structure. Based on the area of particles, the packing is around 0.78 area fraction. If this value is assumed to correlate to the critical pigment volume concentration, which is often around 0.65 for Zhu *et al.* (2014) and for Raman *et al.* (1998), then a scaling factor can be used to link the concentration in the simulation with the experimental values. It was found later that using an area fraction of 0.7 better described the data of Zhu *et al.* (2014). For concentrations above the CPVC, the same packing is used, but the binder bridge area will change, as shown in equation (2.11).

The current model differs from the previous DEM work of Alam *et al.* (2012), of Toivakka and Bousfield (2001), and of Toivakka *et al.* (2014) in some important ways. The approach of the current paper is to use nonlinear springs to simulate the binder and to use monodisperse spheres to represent the pigment particles. Eventually, polydisperse particles will be modeled as well. Alam *et al.* (2012) used both monodisperse and polydisperse particle sizes and they developed a parameter called network connectivity which relates the number of neighboring particles, the binder length, and the binder radius. Toivakka and Bousfield (2001) used linear springs and monodisperse particles in their model. Lastly, Toivakka *et al.* (2014) used a triple tier approach to pack the particles and add the binder, to characterize this matrix, and to do the mechanical simulations in tension mode. They also looked at the influence of dispersants on coating strength.

The first and third papers included non-linear terms and also focused on the type of failure – be it cohesive (within the binder) or adhesive (at the binder-pigment interface) and found that the later type was more likely to occur at lower binder levels.

## **2.4 Comparison of Model to Experimental Data**

The experimental data to which the model is being compared is from Raman *et al.* (1998), Prall (2000), and Zhu *et al.* (2014). In each case, data from those curves using a pigment with an aspect ratio close to one (plastic pigment in the case of Raman and Prall and GCC in the case of Zhu) is used for making the comparisons.

A typical prediction is shown in Figure 2.6. Stress is made dimensionless with the elastic modulus of the pure binder. The shape of the predicted curve is quite similar to what experimental results have been reported by Raman *et al.* (1998), Prall (2000) and Zhu *et al.* (2014). The non-linear shape of the curve is a direct result of using the non-linear expression for the pure binder in the model. The predicted initial slope can be compared to the measured elastic modulus of the coating layer. The maximum stress can be compared to the ultimate tensile stress of the experimental systems. Last, the strain-to-failure prediction is when the stress drops at the end of the calculation and can be compared to the measured values.

One factor that was found to influence the predictions that was not at first expected was the initial packing of the spheres. If the spheres are allowed to approach each other in the packing routine a certain distance, say 1% of the sphere radius, the area fraction will be a certain value, around 0.8. If the approach distance (which is the minimum distance allowed between two spheres in the

packing routine) is reduced to 0.1% of the radius, the area fraction will increase a small amount. However, the predictions of the elastic modulus are sensitive to this approach distance (remember,  $E = \sigma/\epsilon$ ). The reason is that the strain between particles is the current distance divided by the initial separation distance (see equation 2.3). The same total strain in the structure will result in more local strain for the case that has a small approach distance compared to the case that has a large approach distance. The approach distance is set to 0.1% of the sphere radius for the results presented here, but this issue should be studied in more detail in future modeling. In addition, the impact of using particles of different sizes in the model on packing and on the subsequent force calculations needs further study (i.e., using particles having a broad particle size distribution as opposed to ones of the same size as is currently done).

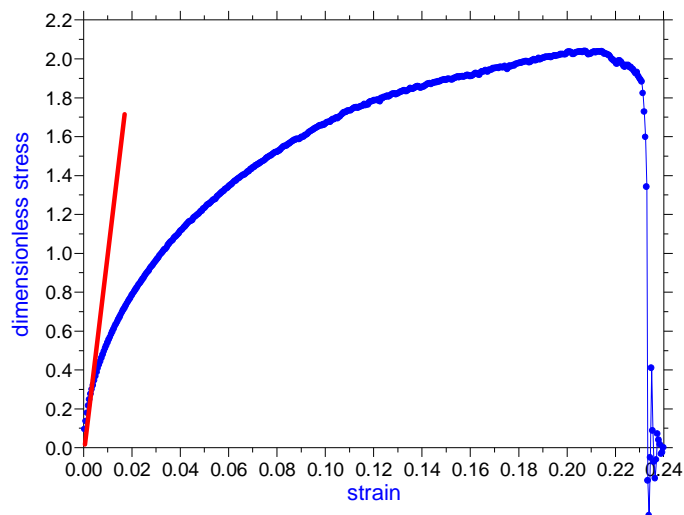


**Figure 2.6 Typical results for  $A^*=0.0288$  and  $B=34.7$  and a binder with a strain-to-failure of 100%. The rapid drop at a strain of 23% is the propagation of a crack in the system. The predicted strain-to-failure is 23% in this case.**

The current model is an improvement over past computer simulations because it can predict the non-linear response of the stress-strain data, as seen in Figure 2.6. The past work has not shown predictions like the current one even for those cases where non-linear functions have been used. While Toivakka and Bousfield (2001) used linear terms, Alam *et al.* (2012), Azadi *et al.* (2008a, 2008b), and Toivakka *et al.* (2014) all used non-linear functions. The non-linear relationships used in these prior studies were unlike the ones used in the current paper and these relationships also involved rather complex connections with the key parameters.

The comparison of the current model to the data of Zhu *et al.* (2014) is shown in Figures 2.7 – 2.9. The results being compared are for the elastic modulus, the maximum tensile stress (i.e., at failure), and the strain-to-failure. For binder systems of pure latex, the model under-predicts the values compared to the experiments. This result may be caused by the fact that the model allows particles only that are in close proximity to “connect”, while in the experimental case, particles may actually be able to connect with others over a wide distance. At low latex content of the binder film, the model over predicts the elastic modulus. One potential reason for the over prediction may link back to the initial separation distance between pigments. For the low latex or high starch binder system, the pigments may not be able to approach each other during drying as close as the pure latex systems because of the viscosity of the fluid phase; this situation would result in high initial gaps between pigments and lower elastic moduli. Experiments that also measure the void fraction of the coating layers may help understand this issue.

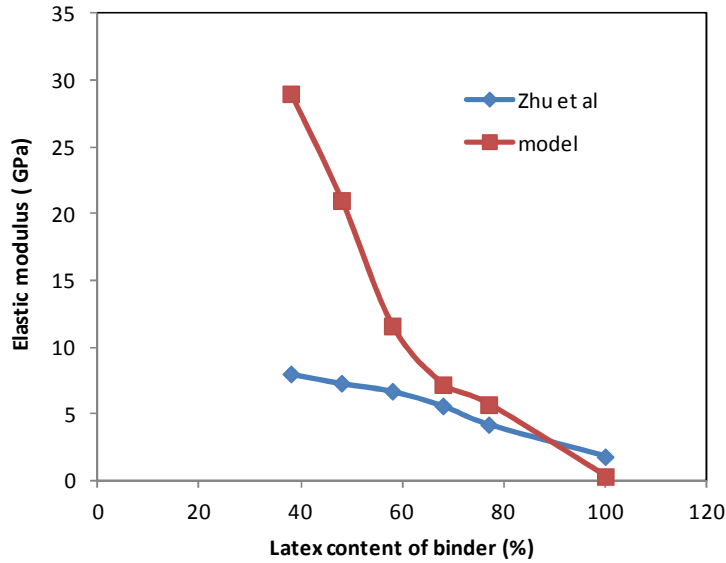


**Figure 2.7 Elastic Modulus comparison between model and Zhu data over a range of latex percentages of the total binder and with a PVC at the CPVC of 0.635. The remaining binder is starch. Simulation used 30 X 30 packing.**

The ultimate tensile stress in the experiments is reported to go to a maximum before decreasing, as shown in Figure 2.8, but the model predicts a steady decrease. In the model, as the latex content increases, the elastic modulus of the binder system decreases, which gives rise to this steady decrease of the ultimate stress. The physical reason for the maximum in the experimental results is not clear, but the low latex coatings were reported to be brittle. This brittle behavior may result in the sample breaking early due to mounting issues.

The model tends to over-estimate the strain-to-failure, as shown in Figure 2.9. The correct trends are predicted in that as the starch content of the binder package decreases, the strain-to-failure increases sharply.

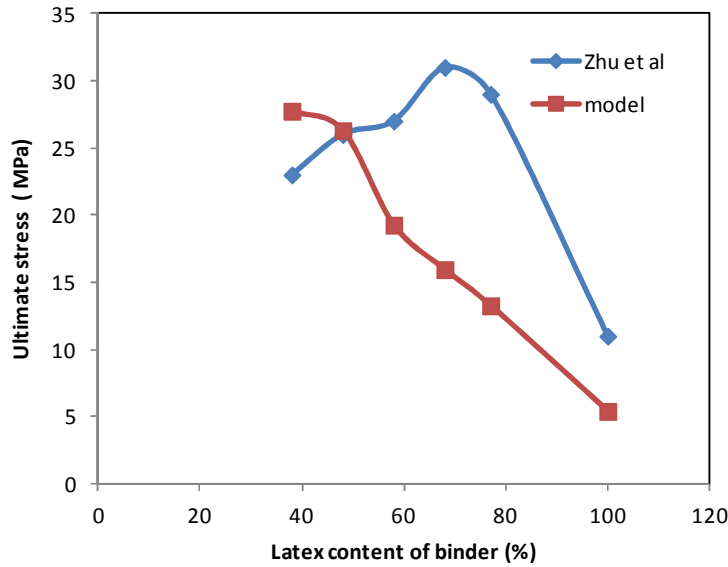


**Figure 2.8 Ultimate tensile stress comparison between model and Zhu data over a range of latex percentages of the total binder and with a PVC at the CPVC of 0.635. The remaining binder is starch. Simulation used 30 X 30 packing.**

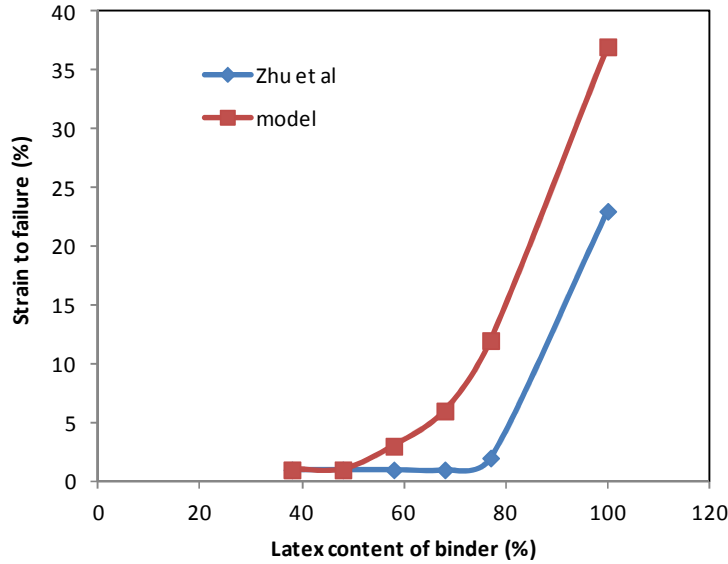


**Figure 2.9 Strain-to-failure comparison between model and Zhu data over a range of latex percentages of the total binder and with a PVC at the CPVC of 0.635. The remaining binder is starch. Simulation used 30 X 30 packing.**

To simulate a lower PVC, the initial packing is set to a low concentration of particles. Around a PVC of 0.4, Zhu *et al.* (2014) give results for the same three parameters above. Figure 2.10 shows the comparison for elastic modulus and for ultimate tensile. The strain-to-failure predictions are similar to above and compare well with the results. Again, the elastic modulus is over predicted by the model for most cases and the ultimate tensile is under predicted. This time, the experimental data do not show the ultimate tensile going through a maximum and have a steady increase like the model predicts.

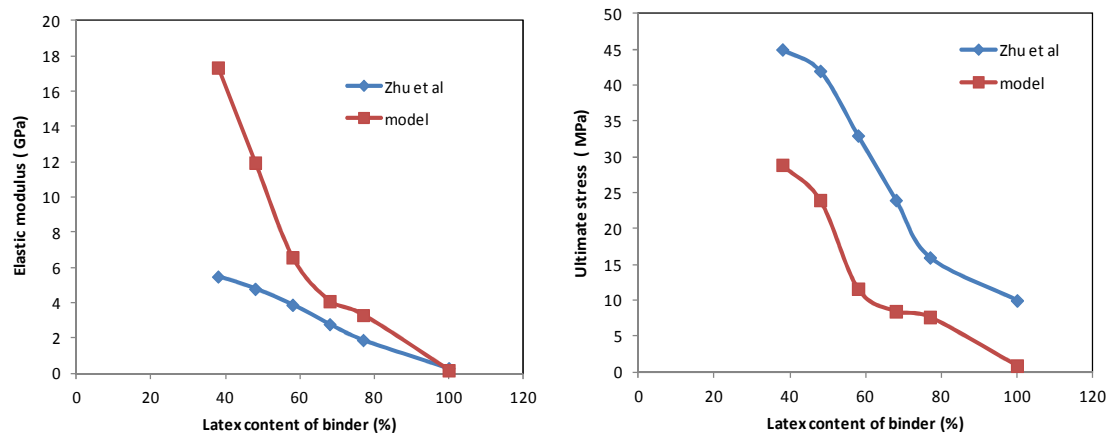


**Figure 2.10 Elastic modulus and ultimate tensile comparison between model and Zhu data over a range of latex percentages of the total binder and with a PVC near 0.4. The remaining binder is starch. Simulation used 30 X 30 packing.**

To model a case over the CPVC, the latex binder bridge is reduced as in equations (2.9) and (2.10). For a PVC around 80, the area of the bridge should be around 80% of the full area. The parameter  $A^*$  (dimensionless  $A$ ) therefore should be around 80% of the case at CPVC. It turns out that the results all scale with this 80% value. The data in Zhu also seem to show this level of decrease after CPVC. The results in Figure 2.11 show the predictions and the data.

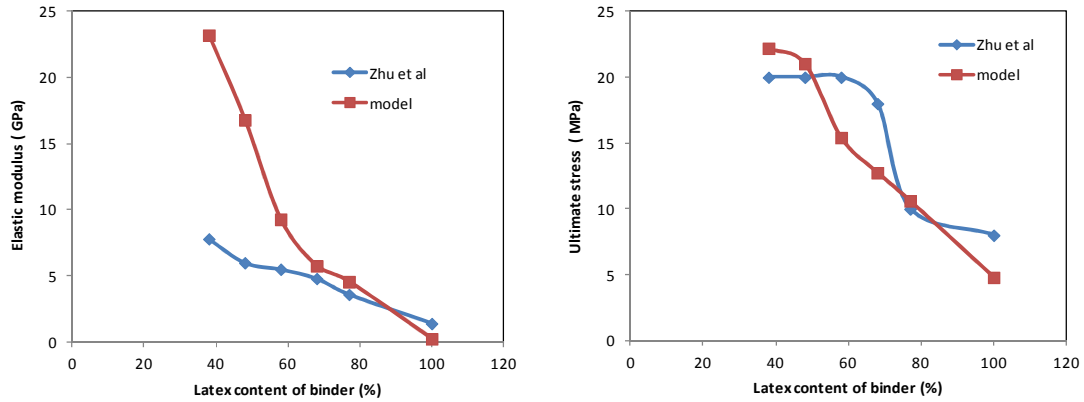


**Figure 2.11 Elastic modulus and ultimate tensile comparison between model and Zhu data over a range of latex percentages of the total binder and with a PVC near 0.8. The remaining binder is starch. Simulation used 30 X 30 packing.**

While the graphs indicate discrepancies between the predicted results and the experimental data, the results do follow similar trends and also are within the same order of magnitude. Another possible explanation for the differences could be the pigment particles used in each case. The model uses homogenous spherical particles whereas the work of Zhu *et al.* (2014) utilized a GCC (60% < 2 microns), which has a broad particle size distribution. And, as previously stated, the starch may impact the particle packing in a different manner than does the latex.

One plot comparing some data from Raman *et al.* (1998) is shown in Figure 2.12. In this case, the model and the experimental data are not in good agreement. Raman did use homogeneous spherical particles in her coating (plastic pigment), but the films were dried close to the glass transition temperature of the plastic pigment, which was styrene. The authors noted that the increase in elastic modulus was larger than expected and could have come from the fusing of the styrene pigments during drying. Note that the model is able to predict the elastic modulus at high PVC. This trend

again is similar to what was seen by Zhu *et al.* (2014). Experimentally, these coating layers are hard to produce without cracks at high values of PVC.

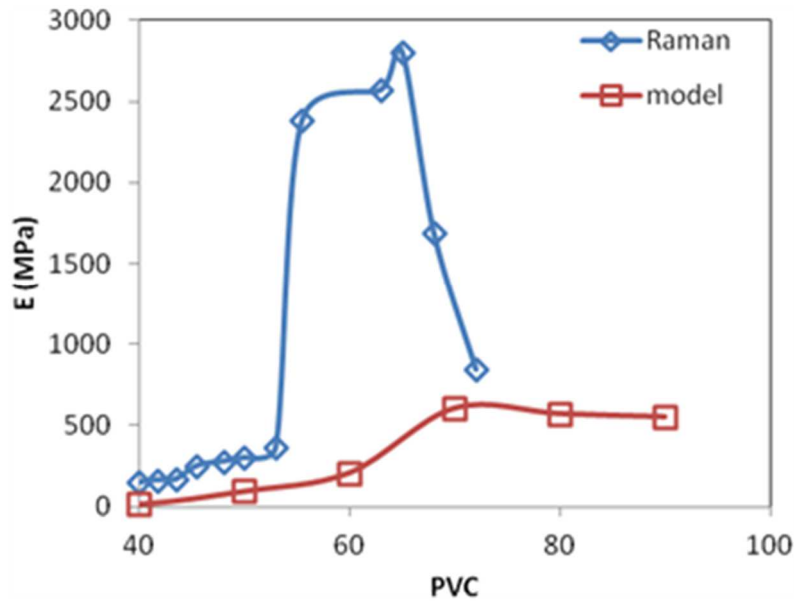


**Figure 2.12 Elastic modulus comparison between model and Raman data (for the one latex used in her study). Simulation used 20 X 40 packing.**

The predictions of the model compared to the results of Prall (2000) are shown in Figure 2.13. The elastic modulus of the pure latex was not clearly reported, but here it was assumed to be 3.8 MPa, the same as the value by Raman *et al.* (1998). The prediction of elastic modulus is much closer to the measured results than the results of Raman. Prall (2000) air dried the samples to remove the potential error from pigments fusing. The model under predicts the results at moderate values of PVC, around 0.5, and at a PVC of 0.85. At PVC of 0.5, the samples were tested at higher rates of strain, to keep the total time for the test the same. Within Prall’s thesis, it is clear that the higher strain rates will generate higher values for elastic modulus than the lower strain rates. Again,

several other reasons for the difference are possible, but this comparison shows that at least the correct order of magnitude is possible.

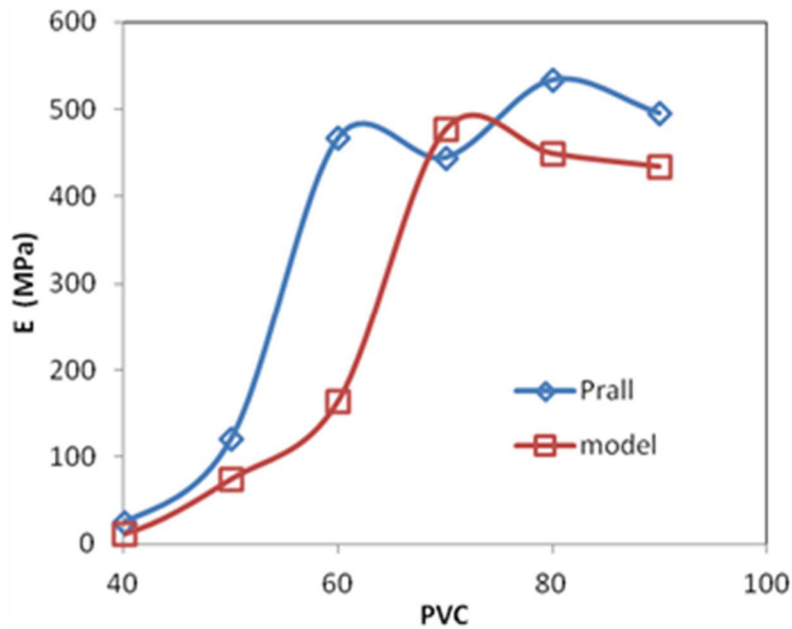


**Figure 2.13 Elastic modulus reported by Prall (2000) and the model predictions. Simulation used 20 X 40 packing.**

Toivakka and Bousfield (2001) were able to predict the oscillatory results of Prall (2000) by only using linear springs and dashpots. Their (2001) findings were likely possible because of the small deformation that occurred in these oscillatory tests. The current model is able to predict the non-linear deformations of the coating layers, but the time dependent aspects will need to be included to be able to predict short time scale deformations.

## 2.5 Conclusions

The current model has shown the ability to simulate in-plane tension events. By applying a force to one end of a matrix of particles and holding the other end stationary, the model can transmit forces throughout the system during the pulling event until a potential failure occurs. Also, relating the binder bridge radius to the PVC “connects” the structure of the coating matrix to the macroscopic mechanical properties of the coating, which is the basis for the DEM approach.

The current model shows the ability to follow the same trends and to be of the same order of magnitude as some experimental data available in the literature. Differences do exist between the model’s predictions and the results generated in the laboratory, but some potential reasons for these discrepancies are offered. Namely, packing is a critical component of the simulation as the model uses spherical particles of the same size while some of the lab work utilizes pigment particles with a broad particle size distribution. The manner in which the lab samples are prepared also is critical to the accuracy of the final results. In addition, the impact that different binders such as starch have on the packing of the pigment particles also is unclear at this point.

## CHAPTER THREE

### DISCRETE ELEMENT METHOD TO MODEL THREE-POINT BENDING EVENTS FOR SINGLE LAYER TWO DIMENSION SYSTEMS OF UNIFORM SPHERES

#### 3.1 Abstract

The folding of coated products is important in a number of applications, such as binding operations and box plants. Discrete element methods (DEM) have been used to simulate tensile and compression events in the past, but not bending situations. A method is proposed to model the three point bending of a coating layer. Properties of the binder and the binder concentration are input parameters. The model predicts the crack formation of the layer, the flexural modulus, and the maximum flexural strain.

#### 3.2 Introduction

The mechanical properties of coating layers influence the ability of the final coated sheet to avoid quality problems such as cracking, pick resistance, and cracking-at-the-fold (CAF). These issues can be the result of post coating application steps such as calendering (cracking), printing (picking), and folding (CAF). The deformation events which occur during these various steps include compression, tension, and bending respectively. The emphasis of this paper will be bending and will focus on a Discrete Element Method (DEM) model for simulating the bending of a coating layer.

While a number of experiments have looked at the tensile properties of coating layers [Prall *et al.* (2000), Raman *et al.* (1998), and Zhu *et al.* (2014)], little has been reported for the bending of free standing coating layers. Most experimental work has focused on bending and measuring the extent

of cracking of coated paper samples. One novel approach to model the bending of coated papers was by Lyons and Peshave (2014). They proposed calculating coating stiffness by using a three-point bending technique in conjunction with modeling coated paper as a multilayer construct as opposed to an I-beam. While most papers focused on cracking in the machine direction (MD), the work of Oh *et al.* (2016) also evaluated the impact of folding in the cross direction (CD) on the degree of cracking. In addition, Rättö *et al.* (2011) showed that coatings that contain kaolin crack differently than coatings that contain calcium carbonate.

The DEM has been used to describe the interactions between individual particles in a variety of systems. In the case of paper coatings, DEM has been used to model situations where the coating is under tension [Alam *et al.* (2012), Toivakka and Bousfield (2001), Toivakka *et al.* (2014), and Varney and Bousfield (2016)] and also when the coating is under compression [Azadi *et al.* (2008a, 2008b) and Ma *et al.* (2008)]. The other common computer modeling technique is the Finite Element Method (FEM), which has been used for modeling tension, compression, and bending events [Alam *et al.* (2009), Barbier (2005), and Salminen *et al.* (2008)]. Finite element methods normally treat the coating or paper as a continuum and therefore do not give insight into events on a particulate level. FEM methods can be used to build up particle level models of coating layers such as described by Barbier *et al.* (2012), but the computational time can become serious as the number of particles increases. The DEM has not been used to model bending type scenarios for paper coatings, which is a gap in the literature that this current paper hopes to fill.

In our paper, a DEM type model is suggested to describe the bending event of a standalone coating layer. Particle-particle interactions are described similar to our most recent paper [Varney and

Bousfield, (2016)]. The bending is simulated by moving a group of particles in a certain direction within the calculation domain. Cracking is predicted when the local strain-to-failure criteria is met. Results are compared to a companion paper of this conference [Hashemi-Najafi *et al.* (2016)].

### 3.3 Model Description

The model builds on the simple idea of Toivakka and Bousfield (2001) where pigments are attached to each other through binder contacts, where the binder is represented by a spring to describe its mechanical response to deformation. Varney and Bousfield (2016) describe a novel approach using a non-linear spring and estimating the binder area contact from the pigment volume concentration (PVC). The non-linear spring gives rise to a response that resembles the slow tensile tests of coatings and the pure binder films and is given by

$$F = A(1 - e^{-B\varepsilon})\pi R_b^2 \quad (3.1)$$

where  $F$  is the tensile force between particles,  $A$  and  $B$  are parameters that depend on the binder that can be obtained from the pure binder films,  $\varepsilon$  is the local strain between particles, and  $R_b$  is the radius of the binder bridge between particles and is a function of the PVC. When the local strain between particles is larger than the strain-to-failure of the binder, the binder is assumed to fail cohesively and the force is set to zero. The parameter  $A$  is also normalized, denoted as  $A^*$ , with the elastic modulus of the binder. The data of Zhu *et al.* (2014) for the pure binder systems has been used for verifying this non-linear expression for the tension forces. For compression, a repulsive force is calculated as

$$F = C\varepsilon \quad (3.2)$$

where  $C$  is a constant and  $\varepsilon$  is the strain as mentioned above. This constant has to be large enough to prevent overlapping, which requires the force to increase as well. A large force would come from the compression of high points on the particles and is important to keep particles from overlapping. The difference between tension and compression is that in compression, the force has to go to a large value as the gap is small to keep particles from overlapping each other while, in tension, the force follows the behavior seen in tensile tests and goes to zero when the critical strain is reached.

The bending simulation is done by holding two groups of particles in place, not allowing motion, while another group of particles is set to move upward as shown in Figure 3.1. This simulates a three point bending test. Other types of deformation are quite possible with the model such as moving a group of particles at one end upward and not allowing some particles on the other end to move, such as in a cantilever. Particles in the up zone are moved upward with a dimensionless velocity of one. Quantities are made dimensionless with the bending velocity, particle radius, and the elastic modulus of the binder. The grip particles can be either not allowed to move at all or not allowed to move in the vertical direction. This later condition lets the particles in the grip zones slide and simulates a three point bending test where the sample is supported loosely with a support structure.

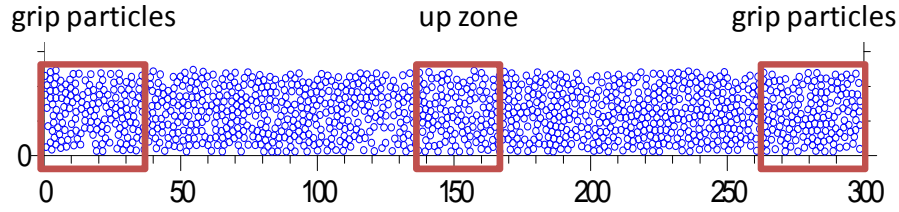


**Figure 3.1 Typical bending simulation showing grip particles and particles that will move upward.**

The force on each particle is calculated as it moves relative to its neighboring particles. If particles move away from each other, equation (3.1) is used to calculate the tension force between these particles. If particles are pushed together, then a repulsive force is applied to keep the particles from overlapping as in equation (3.2). The net vertical force on the left and right grip particles are summed. This upward force should equal the net downward force on the particles that are moving upward to balance the forces. The flexural stress and strain are defined respectively as

$$\sigma_f = \frac{3PL}{2bd^2} \quad (3.3)$$

$$\varepsilon_f = \frac{6Dd}{L^2} \quad (3.4)$$

where  $P$  is the sum of the forces on the grip particles or the load force,  $L$  is the distance between grips,  $D$  is the displacement of the upward moving particles at the center of the sample,  $b$  is the width of the sample and  $d$  is the thickness of the sample. The strain reported here is made dimensionless with the elastic modulus of the binder. The goal is to predict the bending behavior of these systems and to predict the crack propagation.

A model of this nature involves a number of assumptions. The results presented here are limited to equal sized spheres that are confined in a mono-layer. The spheres are assumed to be rigid particles and all of the deformation is either compression or tension of the latex bridges between particles. The model in this current form neglects the rotation and shear between particles; they can be included if these types of deformation are found to be important.

### **3.4 Results and Discussion**

Figure 3.2 shows the bending of a layer of particles for a binder comprised of 52% latex and 48% starch [Zhu *et al.* (2014)]. The dimensionless parameters are noted in the figure caption, where the scenario also is stated as being one in which the grip particles are not allowed to move in the vertical direction (i.e., they can “slide”). Figure 3.3 shows the force and bending strain results. As particles in the center move upward, particles pull on each other along the top surface. This pulling action transmits forces to the grip particles. Cracks are seen both near the region where particles are forced to move upward, and near the grips. When the local strain between particles is larger than the binder strain to failure, the force is set to zero and a small crack is predicted. The force can drop rapidly in this case. If a crack propagates through the whole sample, the sum of the forces goes to zero.

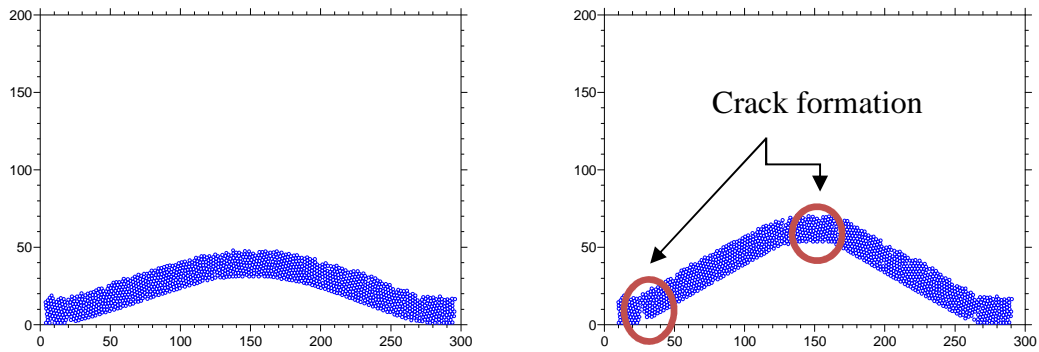


**Figure 3.2** Bending results of a coating layer with  $A^*=0.03$ ,  $B=34.7$ , and strain-to-failure of 24%. Left figure is behavior at short time and right figure is when cracks form. Grip particles are allowed to slide but not move upward.

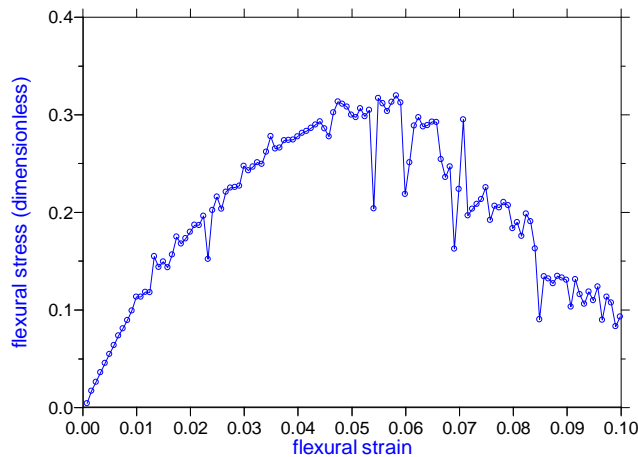


**Figure 3.3** Force on left and right grip particles as a function of bending strain for the conditions in Figure 3.2. Cracks start to form at 6% strain. Grip particles are allowed to slide.

Similar results are obtained when the grip particles are not allowed to move at all. Figures 3.4 and 3.5 show the results for the same parameters as in Figure 3.2. In this case, a single crack forms near the left grip. The strain where cracks first start is earlier. This result makes sense in that the sample is forced to deform more sharply than in the case where the grip particles can slip.

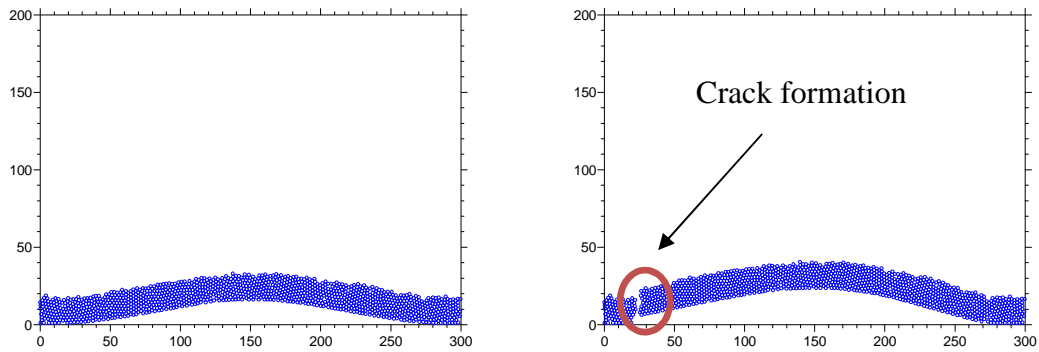


**Figure 3.4** Similar to Figure 3.2 but grip particles are not allowed to move in either the x or y directions.

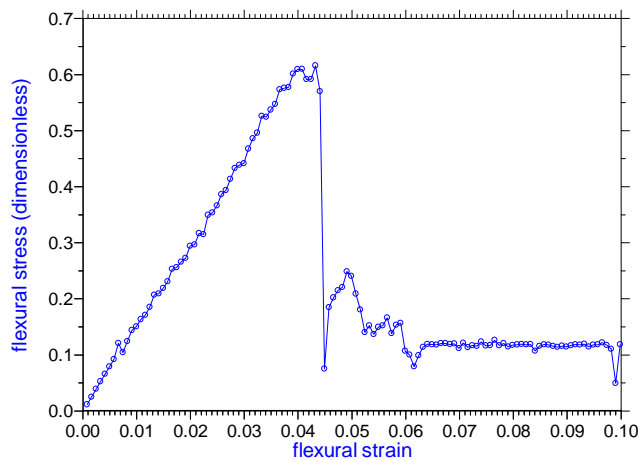


**Figure 3.5** Similar to Figure 3.3 but for grip particles not allowed to move in either the x or y directions. Crack forms around 4% strain where the stress suddenly drops.

The critical pigment volume concentration (CPVC) is assumed to be when the packing of the particles is near the maximum value. Based on the way particles are packed in the packing routine, this scenario occurs near an area fraction of 0.78. Many researchers have reported the CPVC to be near 0.63. Therefore, the ratio of 63/78 is used to convert between area fraction and volume fraction. The initial slope of the stress-strain prediction is used to predict the elastic modulus of

the system. The maximum stress and the strain-to-failure in bending is predicted by the model. By running cases with different packing densities or binder radii, a spectrum of PVC values is simulated. For example, in Figure 3.6, low and high PVC cases are depicted. If the binder has a small strain-to-failure, then a crack can initiate at a low strain. This scenario is for properties of latex-starch system as reported by Zhu *et al.* (2014). If the strain-to-failure of the binder is large, then a greater amount of bending is predicted before a crack is formed.

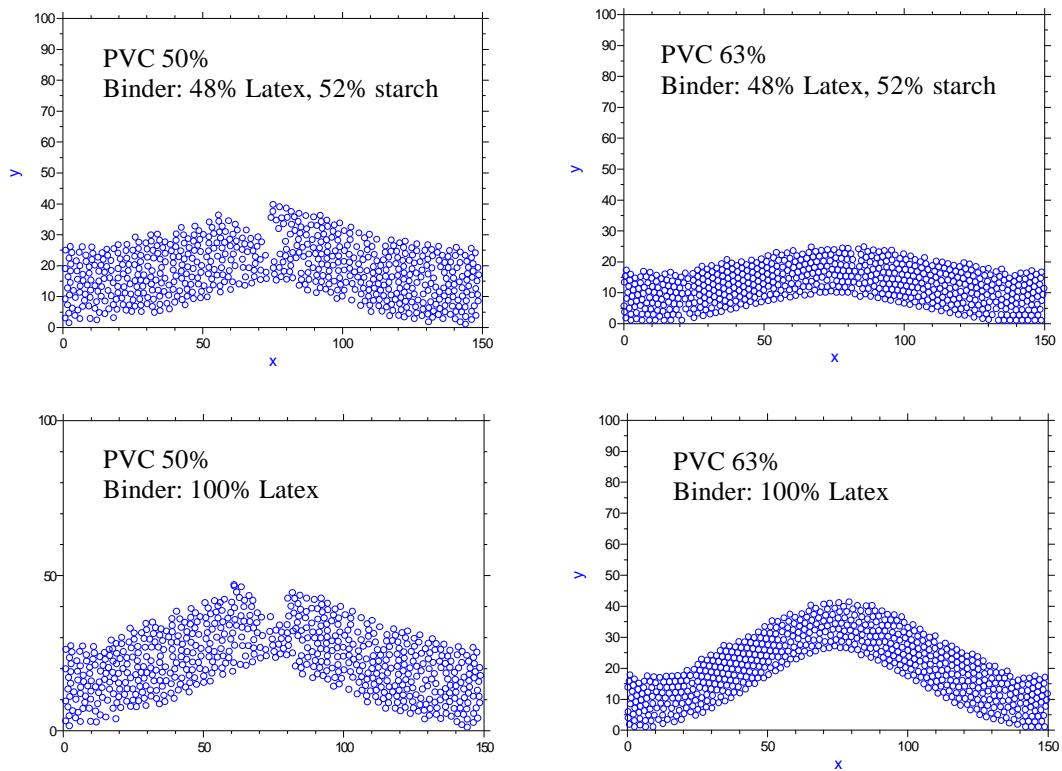


**Figure 3.6 Final result for a low PVC case (left) and high PVC case (right), top are high starch content and bottom are pure latex, using parameters from Zhu *et al.* (2014).**

For a case with a packing that should represent the CPVC, latex properties  $A=1.6$ ,  $B=2$ , and a binder strain-to-failure of 200%; the model predicts the results in Figure 3.7. These latex properties

should match the companion paper Hashemi-Najafi *et al.* (2016). The strain-to-failure predicted is about 5.7%. This result is similar to the values of 3% and 9%, depending on the direction of bending, reported in Hashemi-Najafi *et al.* (2016). The flexural modulus is predicted to be 0.6 GPa, compared to the value of 1.7 and 3.0 GPa, depending on the direction the sample was bent. The stress-at-failure for this case is 19 MPa compared to the averaged measured value of 18 MPa.

The model predicts the stress-at-failure and the strain-to-failure within what could be expected considering the assumptions of the model and the variability of the experiments. The elastic modulus, which comes from the initial slope of the stress-strain curve, is under predicted by a factor of three. The reason for this under prediction is not clear, but several explanations are possible. One issue may be related to the initial packing. Particles are packed into the structure so that the gaps between them cannot be less than 1% of a particle radius. In the experiments, some particles are most likely touching each other. If the initial gap between particles is even smaller, the stress-strain relationship would be even steeper. Another possible reason for the discrepancy between the model and the experimental results may be related to the two dimensional aspect of the model. Lastly, the experiments are using pigments with broad particle size distributions while the model uses only mono-disperse spherical particles. Rättö *et al.* (2012) report the influence of particle size distribution on crack formation.

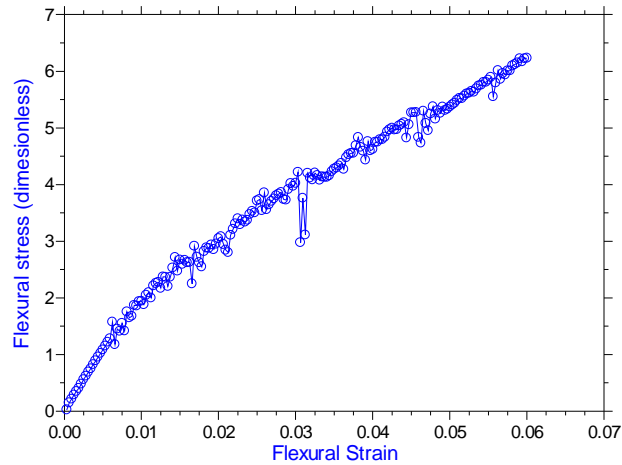


**Figure 3.7 Flexural stress verse strain for binder properties of  $A=1.6$ ,  $B=2$ , and strain-to-failure of 200%. A crack forms at 5.5% strain.**

The model technique has promise to help explore details of the deformation of coating layers on a particle level scale. The goal is for the model to be improved further so it can better predict the number of cracks and the size of cracks that will develop in a folding operation.

### 3.5 Conclusions

A method to model the bending event of a coating layer using a discrete element method is proposed. The flexural stress-strain relationship is predicted based on the PVC and the properties of the binder. The model is able to predict cracks in the structure and the flexural strain-at-failure. The model predicts the stress-at-failure and the strain-at-failure measured in the companion paper, but under predicts the flexural modulus.

## CHAPTER FOUR

### DISCRETE ELEMENT METHOD TO MODEL OUT-OF-PLANE TENSION AND THREE-POINT BENDING EVENTS FOR SINGLE LAYER TWO DIMENSION SYSTEMS OF UNIFORM SPHERES

#### 4.1 Abstract

The mechanical properties of coating layers are critical for post application processes such as calendering, printing, and folding. Discrete element methods (DEM) have been used to simulate basic deformations such as tensile and compression but have not been used as a tool to predict cracking-at-the-fold (CAF) or picking. DEM has the potential to increase our understanding of these failure mechanisms at the particle level.

A method is proposed to model the three point bending of a coating layer and also the out-of-plane picking event during printing (using a z-direction scenario and an approach involving a moving force/velocity). Properties of the binder and the binder concentration are input parameters for the simulation. The model predicts the crack formation of the layer, the flexural modulus, and the maximum flexural strain during bending. The model also predicts the forces required for picking to occur. Results are compared to experiments reported in the companion paper [Hashemi-Najafi *et al.* (2017)].

#### 4.2 Introduction

Coated paper and board undergo a variety of process steps following coating application which, depending on the coating mechanical strength, can have a negative impact on final quality. Such post application steps include calendering, printing, and folding. The potential quality problems that can result from these processes are cracking, picking, and cracking-at-the-fold (CAF)

respectively. These issues result from compression (calendering), z-direction tension (printing), and bending (folding). The proper balance of the mechanical properties of the coated substrate must be achieved to avoid such problems.

The discrete element method (DEM) and the finite element method (FEM) have been used extensively for modeling free-standing coating layers. In the case of DEM, it has been used for modeling coating layers under tension [Alam *et al.* (2012), Toivakka and Bousfield (2001), Toivakka *et al.* (2014), and Varney and Bousfield (2016a)], under compression [Azadi *et al.* (2008a, 2008b) and Ma *et al.* (2008)], and, just recently, during bending [Varney and Bousfield (2016b)]. The FEM has been used to model all three types of events [Alam *et al.* (2009), Barbier (2005), and Salminen *et al.* (2008)]. Lyons and Peshave (2014) used a unique approach to model the bending of coated paper. They proposed calculating coating stiffness by using a three-point bending technique in conjunction with modeling the coated paper as a multilayer construct as opposed to an I-beam. While this work has great potential to understand the macroscopic behavior of these systems, it does not facilitate our understanding on a pigment level.

Because the finite element method normally treats the coated paper as a composite material, it does not make the “connection” between events on the micro-scale and the responses on a macro-scale (as can the DEM). FEM can be used to develop particle-level models [Barbier *et al.* (2012)], but the computational complexity and the computing time increase significantly as the number of particles goes up.

This current paper will build on the recent work of Varney and Bousfield (2016a and 2016b). The non-linear tension model will be applied to out-of-plane (z-direction) tension, which is a modification to the in-plane tensile modeling of the first paper referenced. This effort will simulate picking. Two picking simulations will be studied – the traditional out-of-plane z-direction approach and a novel moving force/velocity situation. In addition, the same tension and compression equations outlined in the second paper will be applied to a three point bending simulation for latex and latex/starch binder systems. For both the picking and bending scenarios, the model will be compared to the experimental data of the companion paper (Hashemi-Najafi *et al.* (2017)].

### 4.3 Model Development

As outlined in the two earlier papers[Varney and Bousfield (2016a and 2016b)], a set of equations were developed to provide a better fit with the non-linear stress-strain results seen during tension experiments [Prall *et al.* (2000), Raman *et al.* (1998), and Zhu *et al.* (2014)]. The force equation evolved into having the following form:

$$F = A(1 - e^{-B\varepsilon})\pi R_b^2 \quad (4.1)$$

where  $F$  is the tensile force between particles,  $A$  and  $B$  are parameters that depend on the pure binder,  $\varepsilon$  is the local strain between particles, and  $R_b$  is the radius of the binder bridge between particles. The bridge radius and the spacing of the particles depends on the pigment volume concentration (PVC), which is defined as the ratio of total volume of pigments to the volume of pigments plus the volume of binder. When the local strain between particles is larger than the

strain-to-failure of the pure binder, the binder is assumed to fail cohesively and the force is set to zero. As confirmed with the data of Zhu *et al.* (2014), the model provides a non-linear response as depicted in Figure 4.1.

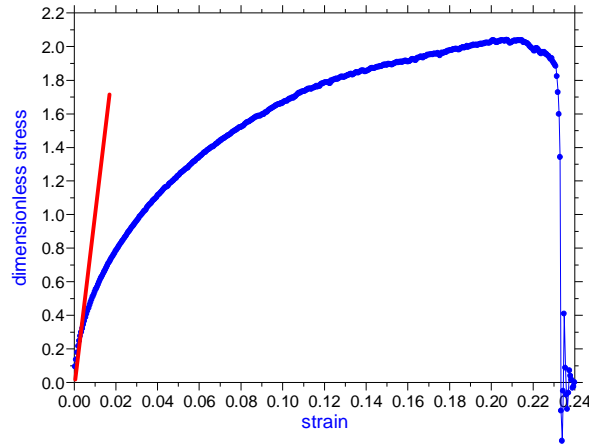


**Figure 4.1 Typical nonlinear response from tension simulation [Varney & Bousfield (2016a)]**

For compression, a repulsive force is calculated as

$$F = C\varepsilon \quad (4.2)$$

where  $C$  is a constant and  $\varepsilon$  is the strain as mentioned above. This constant has to be large enough to prevent overlapping, which requires the force to increase as well. A large force would come from the compression of high points on the particles and is important to keep particles from overlapping. The difference between tension and compression is that in compression, the force has to go to a large value as the gap is small to keep particles from overlapping each other while, in

tension, the force follows the behavior seen in tensile tests and goes to zero when the critical strain is reached.

The bending simulation is done by holding two groups of particles in place, not allowing motion, while another group of particles is set to move upward as shown in Figure 4.2. This arrangement simulates a three point bending test. Other types of deformation are quite possible with the model such as moving a group of particles at one end upward and not allowing some particles on the other end to move, such as in a cantilever. Particles in the “push up” zone are moved upward with a dimensionless velocity of one. The grip particles can be either not allowed to move at all or not allowed to move in the vertical direction. This latter condition lets the particles in the grip zones slide and simulates a three point bending test where the sample is supported loosely with a support structure.

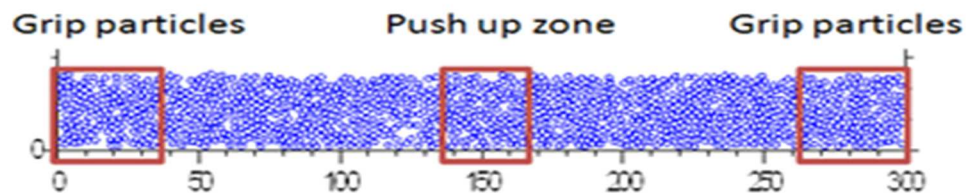


**Figure 4.2 Boundary conditions for a bending simulation. Particles in push up zone are set to move upward.**

The flexural force on each particle is calculated as it moves relative to its neighboring particles. If particles move away from each other, equation (4.1) is used to calculate the tension force between these particles. If particles are pushed together, then a repulsive force is applied to keep the particles from overlapping as in equation (4.2). The net vertical force on the left and right grip

particles are summed. This upward force should equal the net downward force on the particles that are moving upward to balance the forces. The flexural stress and strain are defined respectively as

$$\sigma_f = \frac{3PL}{2bd^2} \quad (4.3)$$

$$\varepsilon_f = \frac{6Dd}{L^2} \quad (4.4)$$

where  $P$  is the sum of the forces on the grip particles (or the load force),  $L$  is the distance between grips,  $D$  is the displacement of the upward moving particles at the center of the sample,  $b$  is the width of the sample and  $d$  is the thickness of the sample. The strain,  $\sigma_f$ , reported here is made dimensionless with the elastic modulus of the binder, and the same applies for the stress,  $\varepsilon_f$ . The goal is to predict the bending behavior of these systems and to predict the crack propagation.

Similar to the bending simulation, the picking model sets the velocity of the top couple of layers of particles to an upward direction in the “pull up” zone (Figure 4.3). Two conditions are compared for other particles: 1) the particles along the bottom of the region are assigned zero velocity or 2) the particles on the sides are not allowed to move. The first condition does not let the paper flex or bend during printing, a condition which printing on both sides of the sample may impose. The second condition would represent single sided printing, where the paper may bend slightly at the nip exit as the ink tack forces pull on the paper. This condition may be similar to standard tests, like the IGT pick test, that prints an ink layer on one side of the paper. The net force on the bottom particles predicts the force event that the coating will see as it fails.

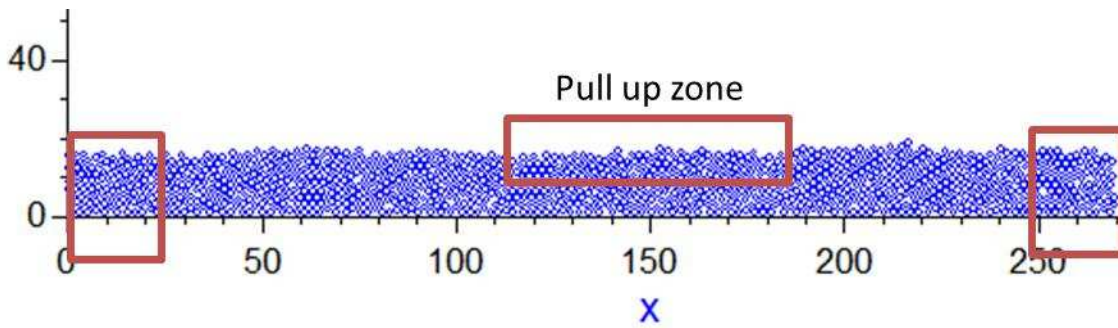


**Figure 4.3 Picking simulation by applying an out-of-plane velocity in the pull up zone. Either bottom layer of particles is held stationary or the side particles are not allowed to move.**

The length scales for the simulations for bending and for picking are scaled with pigment radius. If the particles have a radius of one micron, then the length in Figure 4.3 would represent a 270 by 20 micron region; the height of this region would be typical of a paper coating layer thickness. The length scale is much smaller than typical bending tests or production scale, but representative paper and board deformations of these sorts can be modeled by increasing the number of particles in the matrix. Regardless of the length scale, the results should be similar as the parameters inputted in to the model would be the same.

Another way to simulate picking takes a long layer of particles with a force or velocity dynamically applied to various regions of this sample. Figure 4.4 illustrates this condition. The force is applied to a region of the particles. The position of this applied force or velocity then moves from left to right at some known velocity. This would represent the paper moving from right to left. This scenario should be close to the condition where the tack force is applied to a small region of the paper for a short amount of time as the web exits the printing nip.

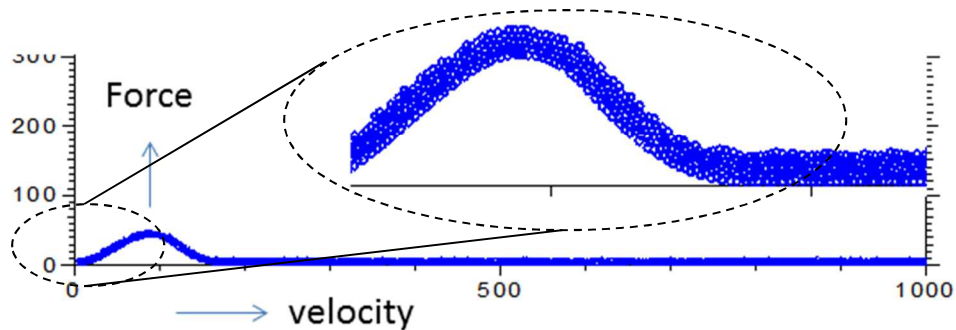


**Figure 4.4 Conditions to simulate the exit of a printing nip. A force is applied to a region of particles and moves along the web. Upper right part of the figure is an enlargement of the region that is experiencing an upward force or velocity. The x-y scales are position.**

A model of this nature involves a number of assumptions. The results presented here are limited to equal sized spheres that are confined in a mono-layer (true three-dimensional simulations eventually will be performed). The spheres are assumed to be rigid particles and all of the deformation is either compression or tension of the latex bridges between particles. The model in this current form neglects the rotation and shear between particles; they can be included if these types of deformation are found to be important. Lastly, the model does not take the Poisson's ratio (the absolute ratio of the transverse strain to the longitudinal strain) into account as the pigment particles and the binder are assumed not to compress. As such, the ratio is presumed to be about 0.5 in all cases.

Figure 4.5 shows the results of a bending simulation for a system near the critical pigment volume concentration for a binder package of 40% latex and 60% starch. As expected, the coating layer fractures earlier than the latex only binder properties at around 1% strain. The flexural stress

increases to a maximum and drops sharply when a crack develops. The shape of these predictions is similar to the experimental results.

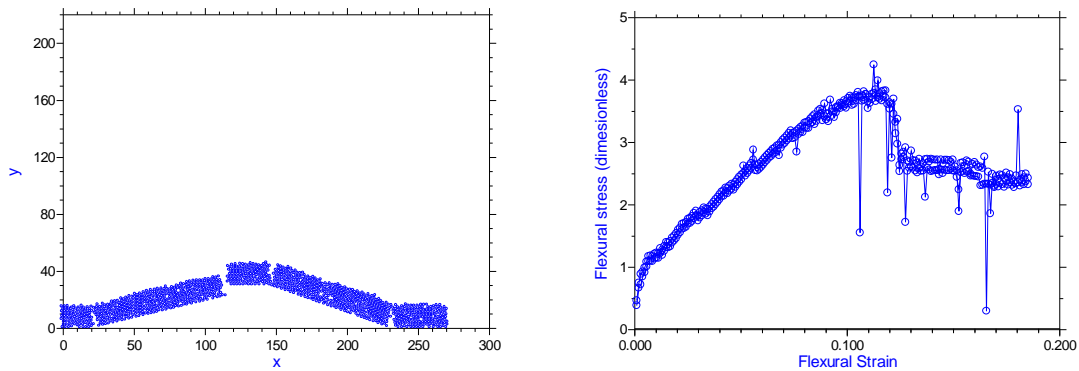


**Figure 4.5 Typical bending results for 62 PVC (20pph binder) for binder properties that resemble 40% latex and 60% starch. Left is the particle positions near the end of the simulation and right is the stress-strain prediction.**

Typical results for the picking simulations are shown in Figure 4.6 where the bottom particles are held stationary. A group of particles are forced to “pick” from the coating layer. In the real situation, the top surface of a coating layer would be subject to a normal-acting tack force instead of a velocity. If the force is less than the maximum shown in Figure 4.6, the particles will deform some amount but then remain as part of the coating layer.

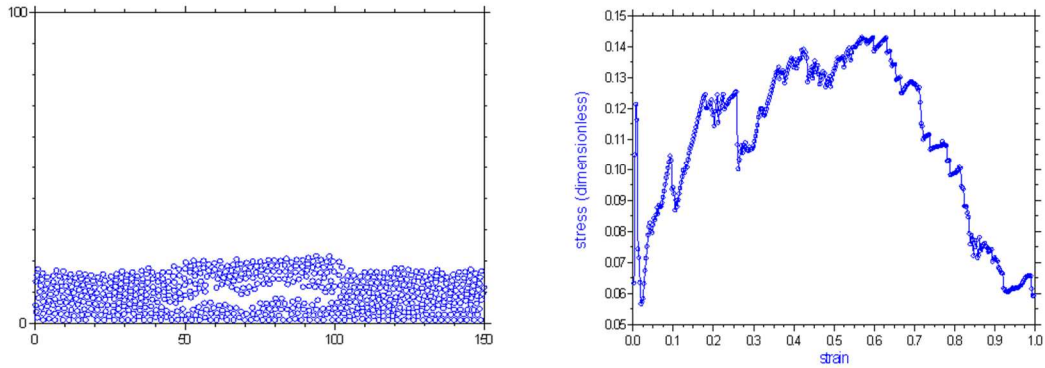


**Figure 4.6 Typical results of the picking simulation for pure latex binder properties and PVC of 62 (20 pph binder). Left is the particle positions near the end of the calculation and right is the stress-strain prediction.**

When the picking simulation is done by allowing the bottom particles to move but by holding the ends stationary, the results in Figure 4.7 are obtained. Again, this situation should represent the case where the web is allowed to deflect a small amount during printing, as would happen with one sided printing. Note that quite a different behavior is obtained in that the coating layer cracks through the entire depth instead of a small region being picked from the coating layer.

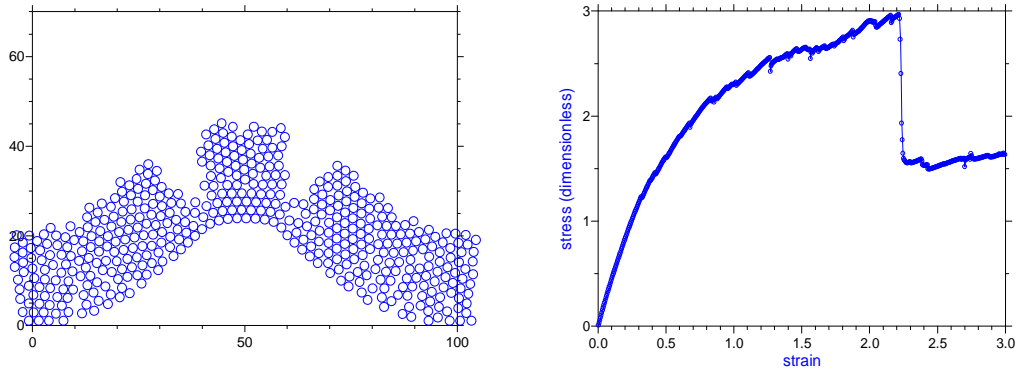


**Figure 4.7 Typical picking results when the ends of the coating layer are fixed for similar binder properties as in Figure 4.6. Left is the particle positions near the end of the calculation and right is the stress-strain prediction.**

Typical results of the moving force boundary conditions are shown in Figure 4.4. For the conditions used, the coating layer deforms and does not crack. In general, the model predicts that as the elastic modulus of the binder becomes large, the force needed to crack the layer increases. This behavior does not agree with the common experience and the companion paper in that as starch is added, the coating layer elastic modulus increases, but the picking velocity decreases.

Another key result for the moving velocity condition is shown in Figure 4.8. In this case, a region of the coating layer is forced to deflect a certain distance because an upward velocity boundary condition is set on a region of the coating layer. The location of this condition moves from left to right in the figure below. Regardless of the elastic modulus of the coating, the layer must deflect. Figure 8 shows that coating layers that contain starch are more prone to crack. Therefore, even though coating layers become stronger with the addition of starch, they also become more brittle. The cracking that is shown in Figures 4.8a and 4.8c illustrate the crack formation that occurs.

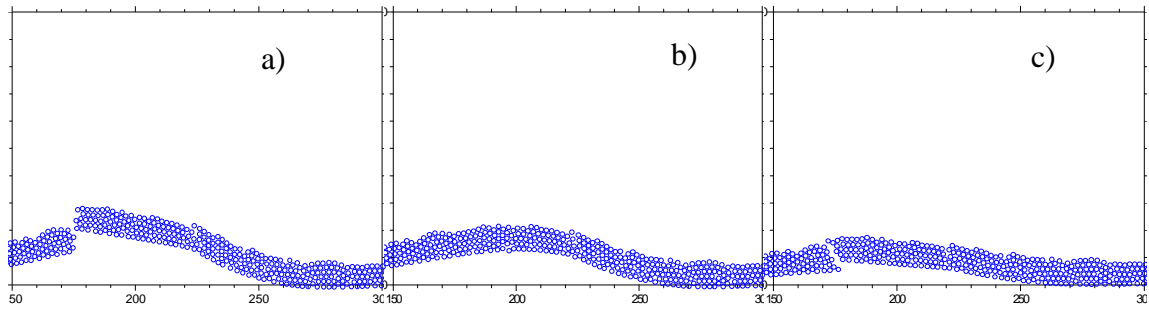


**Figure 4.8 Results for two binder systems at various net displacements. Binder consisting of 80% latex and 20% starch at 20 pph binder with net displacements of a) 12.5 units and b) 10 units. Binder composition of 60% latex and 40% starch and a net displacement of c) 10 units.**

#### 4.4 Comparison to Experimental Data

The results of the model simulations are compared to the experimental work of Hashemi-Najafi *et al.* (2016 and 2017). Their efforts involved both three-point bending and picking experiments. The pigment used in their coatings was a ground calcium carbonate (60 w/w% < 2 $\mu$ m) and various ratios of a latex/starch binder system (latex/starch ratios were 100/0, 80/20, and 60/40). The GCC used in his study would approximate the aspect ratio of the spheres used in the model but would not have the same particle size distribution (the sphere of the model would be mono-disperse whereas the GCC particles would be poly-disperse). The properties of binder-only films were characterized by tensile tests. The parameters that fit the non-linear model are given in Table 4.1. The elastic moduli here are a bit different than the companion paper because the elastic moduli reported in that paper were obtained from the initial slope and not by fitting the entire data set. As expected, as the starch level increases, the elastic modulus increases but the strain to failure decreases. Some tensile properties of the latex only and coating layers with latex as the binder are reported by Hashemi-Najafi *et al.* (2016).

**Table 4.1 Properties of the pure binder films from tensile tests. Strain-to-failure (STF) is given as a percent. 80L-20S is 80% latex and 20% starch on a weight basis from companion paper.**

Parameters	Pure Binder			
	Pure Latex	80 L - 20 S	60 L - 40 S	40 L - 60 S
<b>A</b>	1.5	4.9	4.8	11.0
<b>B</b>	2	15	35	60
<b>E (Mpa)</b>	3	73.5	168	660
<b>STF (%)</b>	200	80	22	5
<b>A*</b>	0.5	0.067	0.029	0.017

#### **4.4.1 Bending simulations**

The comparison of the model predictions with the bending experiments are summarized in Figures 4.9, 4.10 and 4.11. For the 100% latex cases, the model predicts the flexural elastic modulus fairly well and also is close in predicting the maximum stress. The strain at failure is over predicted by the model – this over prediction of the model can easily come from its failure to predict minor defects in the experimental samples that lead to early cracking. The model over predicts the elastic modulus, the maximum stress and the strain at failure for all of the starch containing binder systems. This result is similar to the predictions for tensile properties given by Varney and Bousfield (2016). Numerous possible reasons exist for this over prediction – such as the starch acting to reduce the adhesion of the binder to the pigments, the starch altering the packing properties or the initial separation of the particles (induced flocculation), or the starch causing a number of fine scale defects (shrinkage during drying). The maximum stress predictions are similar to the elastic modulus.

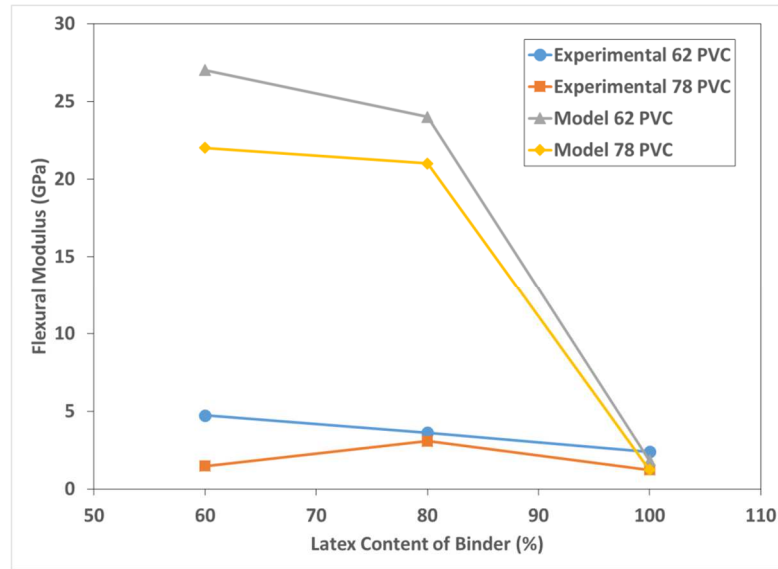


**Figure 4.9 Flexural modulus as a function of the latex content of the binder system for two pigment volume concentrations. The 62 PVC corresponds to 20 parts of binder and 78 PVC corresponds to 10 parts of binder.**

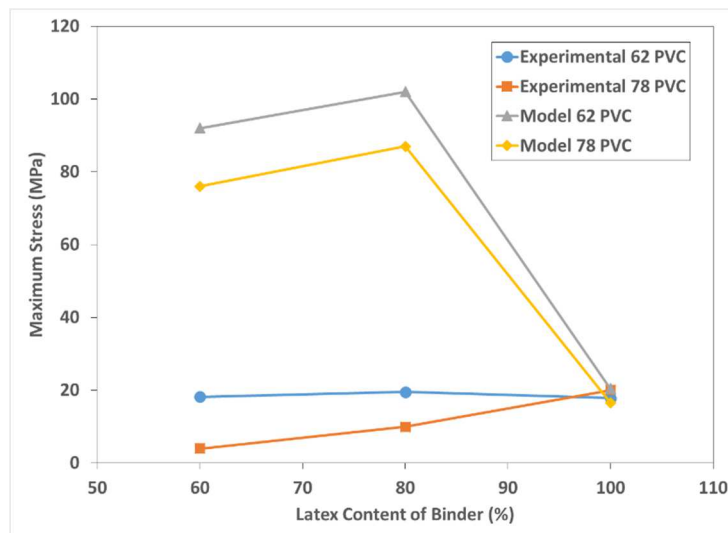


**Figure 4.10 Maximum stress as a function of the latex content of the binder system at two pigment volume concentrations. The 62 PVC corresponds to 20 parts of binder and 78 PVC corresponds to 10 parts of binder.**

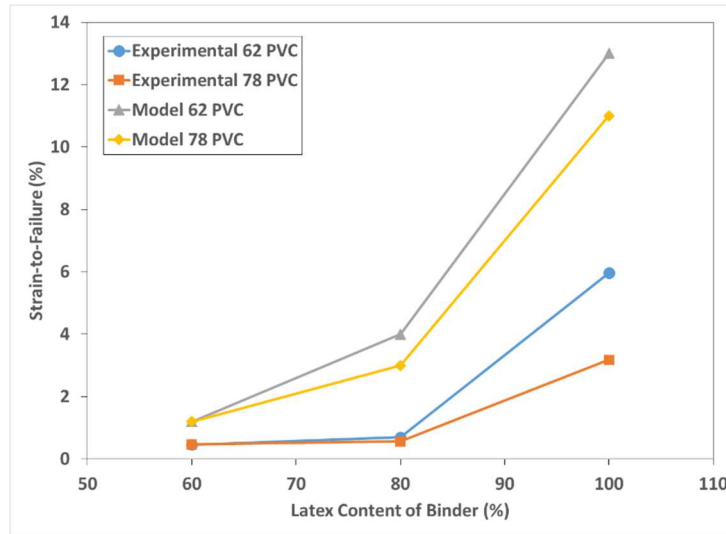


**Figure 4.11 Strain-at-failure as a function of the latex content of the binder for two pigment volume concentrations. The 62 PVC corresponds to 20 parts of binder and 78 PVC corresponds to 10 parts of binder.**

The over-prediction of the elastic modulus and the stress at failure can be expected from looking just at the experimental results. As the pure binder films are changed from pure latex to 60% starch, the elastic modulus of the binder increases by a factor of 50, but the elastic modulus of the coating only increases by a factor of 1.5. Similar results are found in the data of Zhu *et al.* (2014) where the elastic moduli, in tension, of the pure binder films increase by a large amount, yet the moduli of the coating layers, even below CPVC, increase by a modest amount.

As discussed by Zhu *et al.* (2014), starch seems to be acting more like a pigment than a binder. If the starch is viewed as a pigment in the case of a PVC of 62% and a 60% latex/40% starch binder system, the PVC would actually be 77%. When this case is run with the pure latex binder properties, the model predicts an elastic modulus of 2.6 GPa, and a maximum stress of 19 MPa. These values are much closer to the experimental values than if the properties of the starch-latex film in Table 4.1 are used. However, the strain at failure is over predicted by a significant amount.

This over prediction may be due to the assumed ability of the latex to respond to strain as if it were a pure latex film. If the strain to failure for the latex-starch film is used, good predictions of the strain to failure are obtained.

The temperature of the Hashemi Najafi *et al.* (2017) experiments should not have impacted the results for any of the binder systems. The free-standing coating films were dried above the glass transition temperature ( $T_g$ ) of the latex, so this material was able to form a film as expected. Since starch does not have a  $T_g$ , the coating film drying temperature would not influence the behavior of the starch to function as a binder in these experiments, assuming it was cooked adequately (which it was in these studies).

Figures 4.12 – 4.14 show the predictions of the three-point bending results when starch is considered as a pigment – the PVC values are modified by counting the starch volume as a pigment as shown in Table 4.2. The predicted values for elastic modulus and for maximum stress did improve when making these changes while the strain-to-failure values were over predicted.

**Table 4.2 Pigment Volume Concentrations (PVC) – original experimental values vs. PVC values when starch is considered as a pigment. 80L-20S is 80% latex and 20% starch on a weight basis.**

Binder Package	Original PVC	PVC with Starch as Pigment
Pure Latex	78	n/a
80L-20S	78	83
60L-40S	78	87
Pure Latex	62	n/a
80L-20S	62	69
60L-40S	62	77

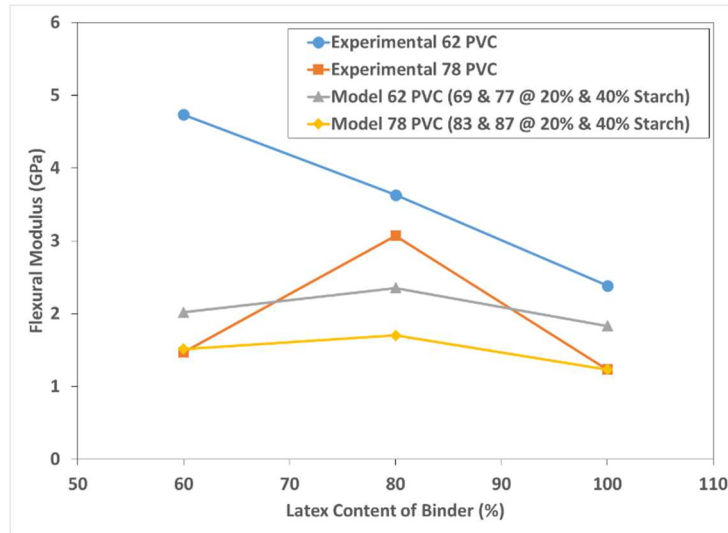


**Figure 4.12 Flexural modulus as a function of the latex content of the binder system for two pigment volume concentrations and with starch as a pigment (62 PVC corresponds to 20 parts of binder and 78 PVC corresponds to 10 parts of binder).**

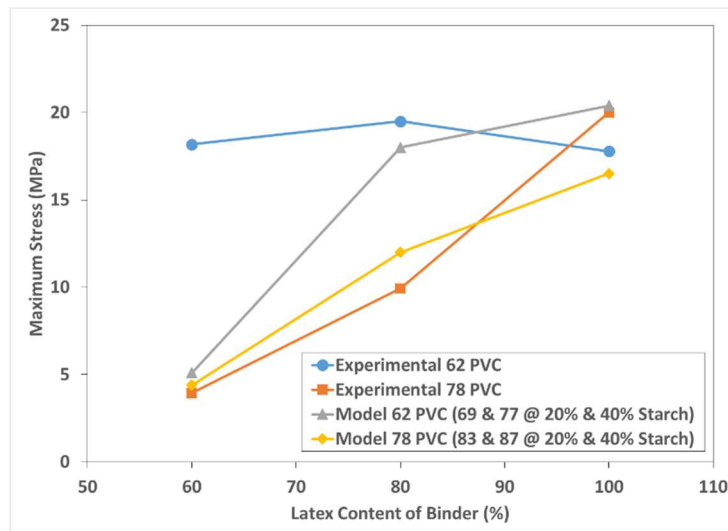


**Figure 4.13 Maximum stress as a function of latex content of the binder system for two pigment volume concentrations and with starch as a pigment (62 PVC corresponds to 20 parts of binder and 78 PVC corresponds to 10 parts of binder).**

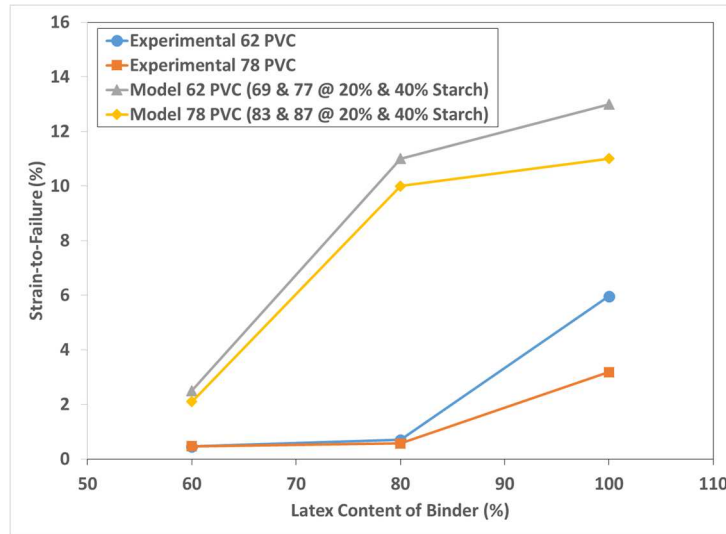


**Figure 4.14 Strain-at-failure as a function of latex content of the binder system for two pigment volume concentrations and with starch as a pigment (62 PVC corresponds to 20 parts of binder and 78 PVC corresponds to 10 parts of binder).**

Another issue which caused the over-predictions at high starch levels may be the adhesive strength of the binder to the pigments. Starch may reduce this adhesive property. Therefore, as the binder elastic modulus increases with starch addition, the adhesive properties of the binder to the pigment may decrease. This adhesive behavior could be studied by measuring the adhesion of binder to calcium carbonate crystals. The adhesive parameter has been incorporated into the current model, but the correct value of this parameter needs to be determined from adhesive type tests.

The best predictions are obtained by assuming that the starch acts as a pigment, by using the binder properties of pure latex, and by using the strain to failure properties of the starch-latex binder film. This method of using the pure binder properties under predicts the elastic modulus of the starch containing coating by around 20%, under predicts the maximum stress by 15%, and over predicts the strain at failure by 80%.

#### 4.4.2 Picking Simulations

Results of the picking simulations when the bottom layer of pigments are held stationary are shown in Figures 4.15 and 4.16. These simulations were done using the four binder packages from the experimental work of the companion paper and three “pull up” zone widths in the model. Changing the widths would represent different ink half tone dot sizes in an offset press, for example. The model particle size is such that the range of up zone widths chosen in this simulation would represent a typical half tone dot size of about 20  $\mu\text{m}$  – 50  $\mu\text{m}$ . This set of data is for a pigment volume concentration at the critical value (CPVC).

The maximum stresses plotted in Figure 4.15 were taken from the peak on the stress/strain curves, like those in Figures 4.6 and 4.7 (right side) and were converted from dimensionless stress to dimensional stress. Figure 4.15 shows how the maximum stress at failure would increase directly with the width of the pull up zone. This plot also shows that the latex-only binder system had the lowest stress values while the trends for the starch-containing systems generally increased in stress indirectly with starch levels. Figure 4.16 is similar to Figure 4.15 except that the dimensionless stress is plotted instead. In this case, the latex-only binder system had the highest values while the addition of starch caused the maximum dimensionless stress to decrease. The predicted stress before the coating cracks is well above the ink tack stress values measured by Harrison and Bousfield (2015). This result indicates that these coating layers would be strong enough to withstand normal offset printing forces.

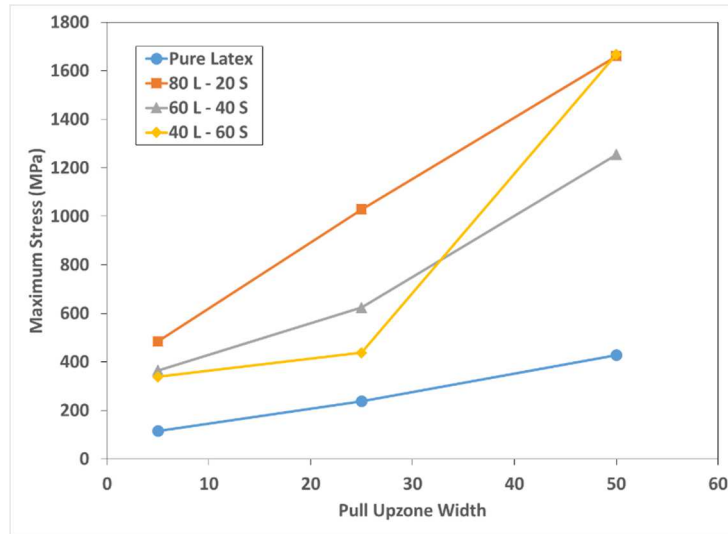


**Figure 4.15 Maximum dimensional picking stress against pull up zone width for four binder systems. 80L-20S is 80% latex and 20% starch on a weight basis.**

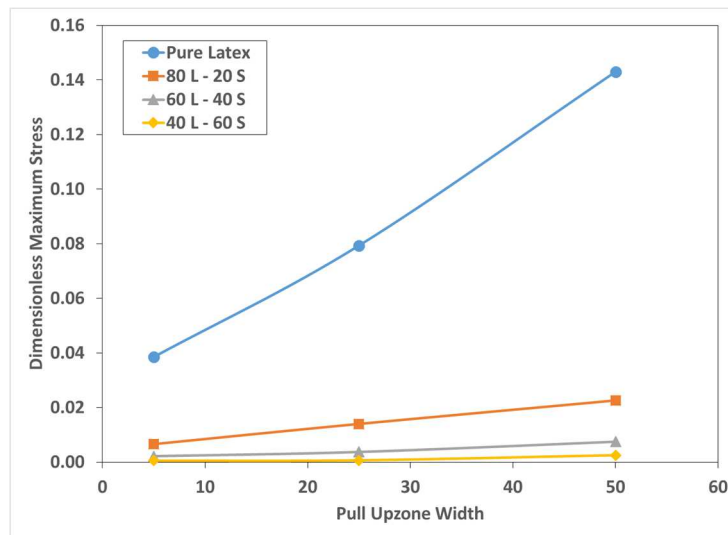


**Figure 4.16 Maximum dimensionless picking stress against pull up zone width for four binder systems. 80L-20S is 80% latex and 20% starch on a weight basis.**

The picking results of Hashemi Najafi *et al.* (2017) show that the IGT velocity at picking increases with the binder level and decreases with the addition of starch. The model also predicts that increasing binder level increases the force required to cause picking. However, the increase in

starch content, corresponding to the amount used in the experiments, should also increase the force required to generate picking. This result is opposite to what was found in the experiments, where increasing starch decreases the pick velocity.

The ability of the coating layer to deform, even a small amount, to a bending motion explains this outcome. As seen with the moving force condition and the picking simulation that allows bending of the coating layer, the addition of starch in the binder system decreases the strain at failure even if the coating layer is stronger.

#### **4.5 Conclusions**

A discrete element model is proposed to describe the bending and picking events for a coating layer. This model has the potential to predict cracking events when the sample is bent or picking phenomena during printing. The model incorporates the mechanical properties obtained from binder only films.

For the bending results, the model predicts well the behavior of coatings that contain only latex as the binder in terms of the elastic modulus, of the maximum stress, and of the strain at failure. For coatings that contain starch, the model over predicts the elastic modulus and maximum stress. If starch is treated as a pigment, and the properties of latex are used for the binder, the predictions are improved.

In the picking simulations, the model predicts the correct trend in terms of binder level. The model also predicts that starch containing coatings should be stronger than coatings that contain only

latex, but the experiments show that the latex only coatings are more resistant to picking. If a deflection or bending of the coating layer is imposed in the model, the cracking of the coating layer is found to increase with starch content. This result agrees with the experiments.

## CHAPTER FIVE

### DISCRETE ELEMENT METHOD TO MODEL THREE-POINT BENDING EVENTS FOR TWO LAYER TWO DIMENSION SYSTEMS OF UNIFORM SPHERES

#### 5.1 Abstract

Cracking at the fold is a serious issue for many grades of coated paper and coated board. Some recent work has suggested methods to minimize this problem by using two or more coating layers of different properties [Salminen *et al.* (2008a and 2008b)]. A discrete element method (DEM) has been used to model deformation events for single layer coating systems such as in-plain and out-of-plain tension, three-point bending, and a novel moving force picking simulation, but nothing has been reported related to multiple coating layers.

In this paper, a DEM model has been expanded to predict the three-point bending response of a two-layer system. The main factors being evaluated include the use of different binder systems in each layer and the ratio of the bottom and top layer weights. As in the past, the properties of the binder and the binder concentration are input parameters. The model can predict crack formation that is a function of these two sets of factors. In addition, the model can predict the flexural modulus, the maximum flexural stress, and the strain-at-failure. The predictions are qualitatively compared to experimental results reported in the literature.

#### 5.2 Introduction

While coated board grades are typically double or triple coated, the number of coating layers applied for standard coated paper grades depends on the location of production. North American coated papers typically are single coated while similar papers in Europe can have multiple layers

of coating applied. The mechanical properties of all coating layers are critical to the paper and board passing through the various post coating application steps without experiencing any quality problems. These process steps include calendaring (compression), printing (z-direction tension), and folding (bending). The potential quality problems that can result from these processes are cracking, picking, and cracking-at-the-fold (CAF), respectively.

The two main computer modeling techniques used for modeling free-standing coating layers has been the discrete element method (DEM) and the finite element method (FEM). The DEM approach has been used for modeling coating layers under tension [Alam *et al.* (2012), Toivakka and Bousfield (2001), Toivakka *et al.* (2014), and Varney and Bousfield (2016a)], under compression [Azadi *et al.* (2008a, 2008b) and Ma *et al.* (2008)], and during bending [Varney and Bousfield (2016b and 2017)]. The FEM has been used to model all three types of events [Alam *et al.* (2009), Barbier (2005), and Salminen *et al.* (2008a)].

The work of Salminen *et al.* (2008a and 2008b), of Alam *et al.* (2009), and of Yang *et al.* (2014) was different because they looked at the impact of multiple coating layers on coating mechanical properties. All three groups were trying to optimize the balance between stiffness and CAF for multiple coated papers. While the work of the first two groups involved modeling and pilot lab trials (comparing double and triple coating), the third team scaled up this work to the commercial level. The chief findings were that the optimal balance between stiffness and CAF was the case of a triple coated paper. This “ideal” paper was determined to consist of a thin, stiff bottom coating layer; a thick, lower-stiffness middle coating layer; and a thin, stiff top coating layer.

Oh *et al.* (2014) conducted a series of lab experiments evaluating the folding response of double coated heavy weight papers and the relationship of tensile to CAF. They looked at the impact of styrene butadiene (SB) latex glass transition temperature ( $T_g$ ) in the topcoat, of starch levels in the precoat, and of GCC particle size. While not commenting on the effect of the pigments, they pointed out the negative impact of starch and of higher latex  $T_g$  on cracking tendency. An important finding was that, as both starch levels and latex  $T_g$  increased, the number of cracks decreased but their length and area increased.

Because the finite element method normally treats the coated paper as a composite material, it does not make the “connection” between events on the micro-scale and the responses on a macro-scale (as can the DEM). FEM can be used to develop particle-level models [Barbier *et al.* (2012)], but the computational complexity and the computing time increase significantly as the number of particles goes up.

This current paper will build on the recent work of Varney and Bousfield (2016b and 2017). The three-point bending model of these papers will be expanded from one to two coating layers. The impact of latex to starch ratio and of top layer to bottom layer thickness ratio (i.e., coat weight ratio) will be assessed. The model results will be compared to the past work where multiple coating layers were applied to a variety of paper substrates [Salminen *et al.* (2008a and 2008b), Alam *et al.* (2009), Oh *et al.* (2014), Yang *et al.* (2014), and Hashemi-Najafi *et al.* (2018)].

### 5.3 Model Development

Previous work (Varney and Bousfield 2016a, 2016b, and 2017) discussed an equation that provides a good fit with the non-linear stress-strain results seen in prior tension experiments [Prall *et al.* (2000), Raman *et al.* (1998), and Zhu *et al.* (2014)]. The force equation had the following form:

$$F = A(1 - e^{-B\varepsilon})\pi R_b^2 \quad (5.1)$$

where  $F$  is the tensile force between particles,  $A$  and  $B$  are parameters that depend on the pure binder,  $\varepsilon$  is the local strain between particles, and  $R_b$  is the radius of the binder bridge between particles. The bridge radius and the spacing of the particles depends on the pigment volume concentration (PVC), which is defined as the ratio of total volume of pigments to the volume of pigments plus the volume of binder. When the local strain between particles is larger than the strain-to-failure of the pure binder, the binder is assumed to fail cohesively and the force is set to zero. Using data from Zhu *et al.* (2014), the model provides a non-linear response as depicted in Figure 5.1.

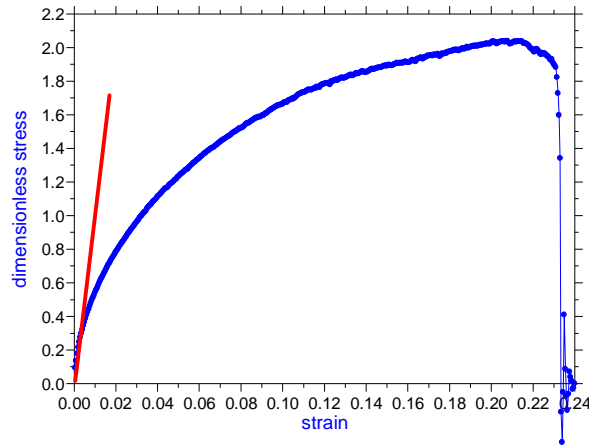


**Figure 5.1 Typical non-linear response from tension simulation [from Varney and Bousfield (2016a)].**

For compression, the repulsive force equation was established as

$$F = C\varepsilon \quad (5.2)$$

where  $C$  is a constant and  $\varepsilon$  is the strain as mentioned above. This constant has to be large enough to prevent overlapping, which requires the force to increase as well. A large force would come from the compression of high points on the particles and is important to keep particles from overlapping. The difference between tension and compression is that in compression, the force has to go to a large value as the gap is small to keep particles from overlapping each other while, in tension, the force follows the behavior seen in tensile tests and goes to zero when the critical strain is reached.

The bending simulation is done by holding two groups of particles in place, not allowing motion, while another group of particles is set to move upward as shown in Figure 5.2. This arrangement simulates a three-point bending test. Other types of deformation are quite possible with the model such as moving a group of particles at one end upward and not allowing some particles on the other end to move, such as in a cantilever. Particles in the “push up” zone are moved upward with a dimensionless velocity of one. The grip particles can be either not allowed to move at all or not allowed to move in the vertical direction. This latter condition lets the particles in the grip zones slide and simulates a three-point bending test where the sample is supported loosely with a support structure. For the simulations conducted for this paper, the grip particles were allowed to slide.

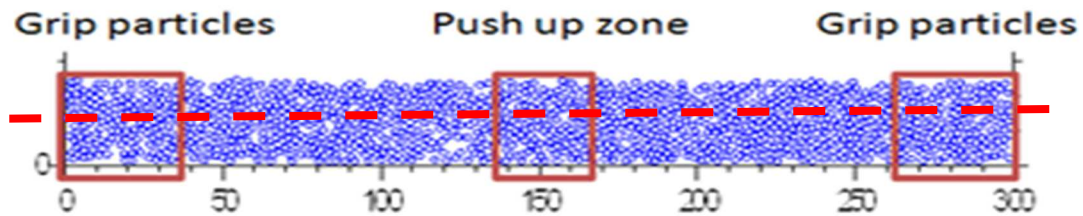


**Figure 5.2 Boundary conditions for a bending simulation. Particles in push up zone are set to move upward. The distance from the zero-y position to the red broken line is the height of the bottom layer.**

The flexural force on each particle is calculated as it moves relative to its neighboring particles. If particles move away from each other, equation (5.1) is used to calculate the tension force between these particles. If particles are pushed together, then a repulsive force is applied to keep the particles from overlapping as in equation (5.2). The net vertical force on the left and right grip particles are summed. This upward force should equal the net downward force on the particles that are moving upward to balance the forces. The flexural stress and strain are defined respectively as

$$\sigma_f = \frac{3PL}{2bd^2} \quad (5.3)$$

$$\varepsilon_f = \frac{6Dd}{L^2} \quad (5.4)$$

where  $P$  is the sum of the forces on the grip particles (or the load force),  $L$  is the distance between grips,  $D$  is the displacement of the upward moving particles at the center of the sample,  $b$  is the width of the sample and  $d$  is the thickness of the sample. The strain,  $\sigma_f$ , is made dimensionless with the elastic modulus of the binder. The goal is to predict the bending behavior of these systems and to predict the crack propagation.

The key difference between this paper and the previous ones presented by Varney and Bousfield (2016b and 2017) on 3-point bending is the modeling of two layers in the present case. This “splitting” of the layers is performed by setting the particles below a certain height to have the properties of one binder system and the particles above this height (up to the top of the particle matrix) to have the properties of a different binder system. As such, data from two binder systems as well as the intermediate height (the bottom layer height) are inputs to the two-layer model. For this paper, an 18 x 300 particle matrix was used, with the bottom layer height being 4.5, 9.0, and 13.5 (thus, establishing bottom layer to top layer ratios of 25:75, 50:50, and 75:25 respectively). The binder systems used in these simulations were based on the data of Hashemi-Najafi *et al.* (2017) and were 60% latex/40% starch, 80% latex/20% starch, and 100% latex/0% starch. These binder systems would represent typical latex to starch ratios used in the paper industry.

The length scales for the bending simulations are scaled with pigment radius. If the particles have a radius of one micron, then the length in Figure 5.2 would represent a 300 by 18-micron region; the height of this region would be typical of a paper coating layer thickness. The length scale is much smaller than typical bending tests or production scale, but representative paper and board deformations of these sorts can be modeled by increasing the number of particles in the matrix. Regardless of the length scale, the results should be similar as the parameters inputted in to the model would be the same.

A model of this nature involves a number of assumptions. The results presented here are limited to equal sized spheres that are confined in a mono-layer (true three-dimensional simulations currently are in progress). The spheres are assumed to be rigid particles and all of the deformation is either compression or tension of the latex bridges between the particles. The model in this current form neglects the rotation between particles, which can be included if it is deemed to be important. In addition, the failure between the particles is assumed to be cohesive in nature, so any failure that takes place is within the binder bridge and not at the interface between the binder and the particles (recent work has incorporated adhesive failure in to the model, but it was not included in this paper). Lastly, the model does not take the Poisson' ratio (the absolute ratio of the transverse strain to the longitudinal strain) in to account as the pigment particles and the binder are assumed not to compress. As such, the ratio is presumed to be about 0.5 in all cases.

Figure 5.3 below shows the results of a bending simulation in which the bottom layer was comprised of 80% latex and 20% starch (80L/20S) and the top layer consisted of 60% latex and 40% starch (60L/40S). The ratio of the bottom layer to the top layer heights (i.e., the coat weight

ratio) was 75% bottom layer and 25% top layer. The PVC for the simulations was kept to a constant value of about 62. The pure binder data used as inputs for the model came from the work of Hashemi-Najafi *et al.* (2017), where the PVC was 62 (20 pph binder). The particle position plot on the left shows the formation of cracks taking place in the top layer, which has a higher amount of starch in it, but the cracks do not propagate through the second layer.

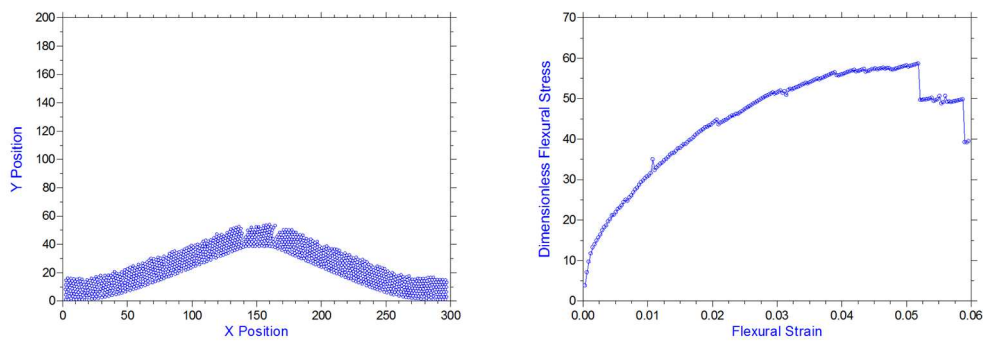


**Figure 5.3 Typical results for 62 PVC (20 pph binder) with binder properties that resemble 60% latex and 40% starch in the top layer and 80% latex and 20% starch in the bottom layer. The ratio of bottom layer height to top layer height was 75:25. Left is the particle positions near the end of the simulation and right is the stress-strain prediction.**

#### 5.4 Simulation Results

A total of 21 simulations were conducted in generating data for this paper – 18 representing various combinations of bottom layer/top layer thicknesses and binder systems and three representing single coating with the three individual binder systems (60L/40S, 80L/20S, and 100L/0S). The model inputs for the pure binder data of Hashemi-Najafi *et al.* (2017) is show in Table 5.1 below.

**Table 5.1 Properties of the pure binder films from tensile tests. Strain-to-failure is given as a percent. 80L-20S is 80% latex and 20% starch on a weight basis from companion paper.**

<b>Parameters</b>	<b>Pure Latex</b>	<b>80L-20S</b>	<b>60L-40S</b>
<b>A</b>	1.5	4.9	4.8
<b>B</b>	2.0	15.0	35.0
<b>E (MPa)</b>	3.0	73.5	168.0
<b>STF (%)</b>	200.0	80.0	22.0

The results for flexural modulus, maximum stress, and strain-at-failure are shown in Figures 5.4 – 5.6 below. Each property is plotted against the height of the bottom layer (with the total height being 18 in dimensionless form). Thus, a bottom layer height of 4.5 means the top layer height is 13.5 and the ratio of the bottom to the top layer heights is 25:75. A height of 18 indicates that the coating is comprised of one layer.

For the flexural modulus, the simulations show the values to be highest with increased thickness of the starch-rich layer. This layer dominates the response and drives the flexural modulus to a value approaching the single layer condition with the same starch-rich binder system. The same trends were observed with the maximum stress. As for the strain-at-failure (STF), similar trends are observed, but in reverse. The values tend to decrease at higher thicknesses of the starch-rich layer as is expected. In addition, the highest STF values were for increasing thickness of an all latex binder bottom layer (100L/0S), with either of the other two binder systems in the top layer. When the 100L/0S binder is in the top layer, the STF values remain constant with bottom layer height regardless of the bottom layer binder system (80L/20S or 60L/40S). These constant values are very similar to the single layer condition using the same binder package as the bottom layer.

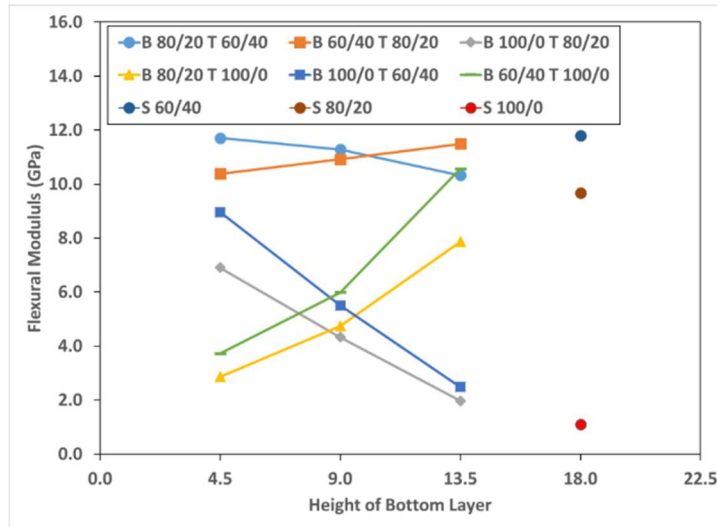


**Figure 5.4 Simulated flexural modulus as a function of the bottom layer height and various bottom layer/top layer binder systems. B 80/20 T 60/40 stands for bottom layer with an 80% latex/20% starch binder system and a top layer with a 60% latex/40% starch binder system. S 60/40 stands for single layer with a 60% latex/40% starch binder system.**

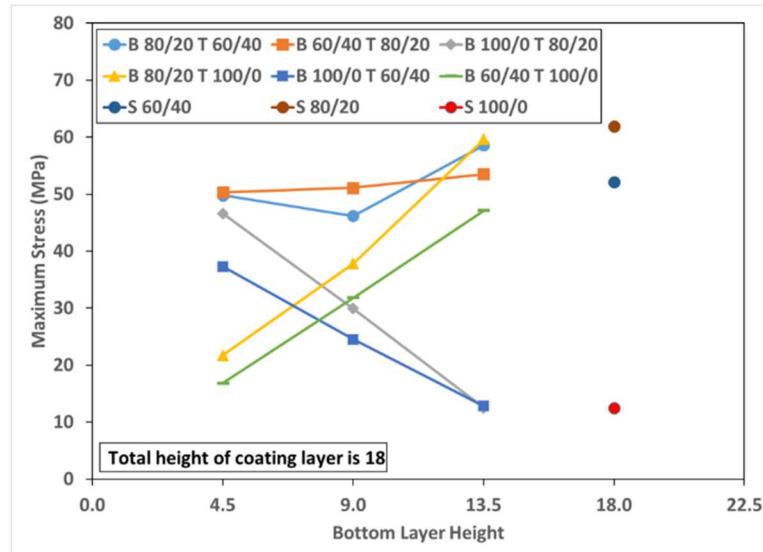


**Figure 5.5 Simulated maximum stress as a function of the bottom layer height and various bottom layer/top layer binder systems. B 80/20 T 60/40 stands for bottom layer with an 80% latex/20% starch binder system and a top layer with a 60% latex/40% starch binder system. S 60/40 stands for single layer with a 60% latex/40% starch binder system.**

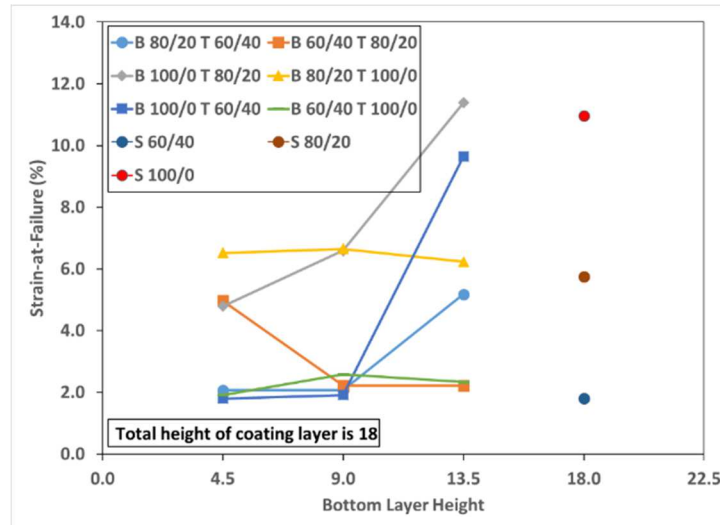


**Figure 5.6 Simulated strain-at-failure as a function of the bottom layer height and various bottom layer/top layer binder systems. B 80/20 T 60/40 stands for bottom layer with an 80% latex/20% starch binder system and a top layer with a 60% latex/40% starch binder system. S 60/40 stands for single layer with a 60% latex/40% starch binder system.**

The position plots show cracking in all 21 cases if the simulation is allowed to run long enough to result in failure. Cracking would always occur in the starch-rich layer regardless of whether it was in the top or bottom layer. The appearance of cracks in the bottom layer always occurred near the grips. While cracks did appear in some cases for the all-latex binder system, this situation was in the minority and might have been more a result of the length of the simulation. These durations were varied to achieve failure (and, therefore, to obtain the stress/strain and modulus values) and might not correlate perfectly with a bending test, which is run for the same amount of time in all experiments.

Some specific situations are depicted in position plots show in Figures 5.7 – 5.10 below. The first three cases are for thick bottom layers with thin top layers (a 75:25 ratio of bottom layer to top layer heights). Figures 5.7 and 5.8 represent opposite scenarios, with the first layer being a thick

latex only bottom layer with a thin starch rich top layer while the second case is a thick starch rich bottom layer with a thin latex only top layer. In Figure 5.7, the cracks appear only in the thin starch containing top layer. The thick latex rich bottom layer does not appear to crack, as might be expected. Figure 5.8 shows cracking in the bottom thick starch rich layer, but it also shows cracks in the top latex only thin layer. The appearance of cracks in this top layer is a bit confusing, but it could be due to slippage out of the grips as seen by the bottom cracks on the left and right sides. In addition, the work of Salminen *et al.* (2008a and 2008b) showed the case of Figure 5.7 to be less prone to cracking. Figure 5.9 shows a two-layer system with a 50:50 split of a 60% latex/40% starch bottom layer (60L/40S) and an 80% latex/20% starch top layer (80L/20S). In this case, the more cracks occur in the higher starch containing bottom layer, as might be expected. Lastly, Figure 5.10 is a single layer (of equal thickness as the two-layer systems) with a binder system comprised of 60% latex and 40% starch. Cracks can be seen in both the top and bottom of the single layer. As in the other cases, the bottom cracks appear near the grips, possibly indicating some slipping at these positions.

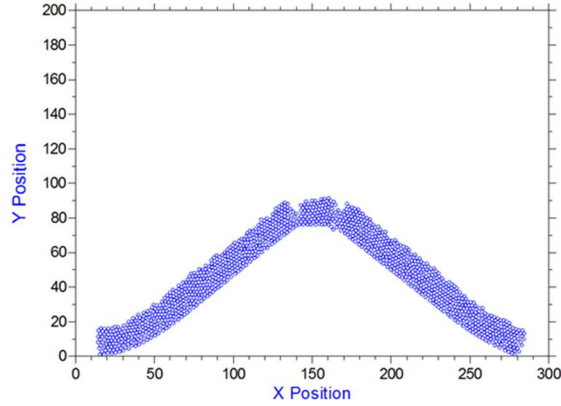


**Figure 5.7** Position plot for 62 PVC (20 pph binder) with binder properties that resemble 100% latex in the bottom layer (100L/0S) and 60% latex plus 40% starch in the top layer (60L/40S). The ratio of bottom layer to top layer heights is 75:25 (i.e., a thick latex rich bottom layer and a thin starch rich top layer).

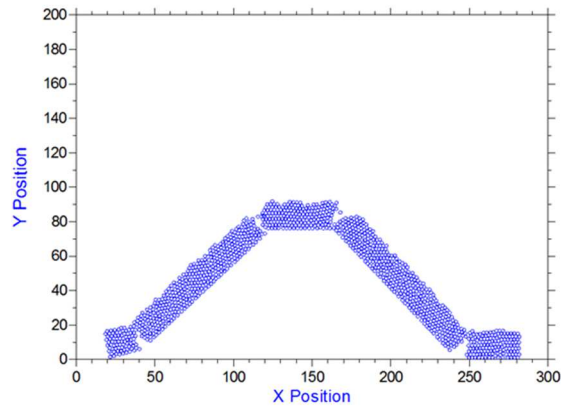


**Figure 5.8** Position plot for 62 PVC (20 pph binder) with binder properties that resemble 60% latex plus 40% starch in the bottom layer (60L/40S) and 100% latex in the top layer (100L/0S). The ratio of bottom layer to top layer heights is 75:25 (i.e., a thick starch rich bottom layer and a thin latex rich top layer).

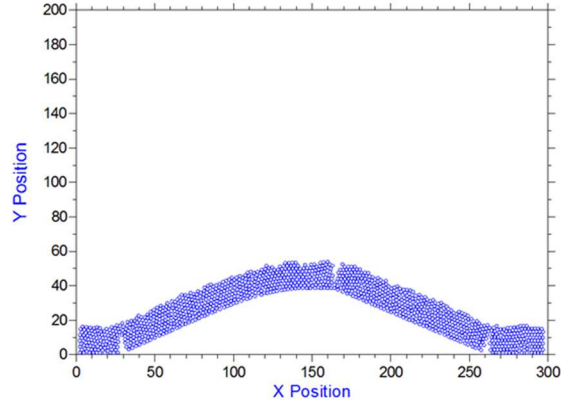


**Figure 5.9** Position plot for 62 PVC (20 pph binder) with binder properties that resemble 60% latex plus 40% starch in the bottom layer (60L/40S) and 80% latex plus 20% starch in the top layer (80L/20S). The ratio of bottom layer to top layer heights is 50:50 (i.e., layers of equal thickness which both contain starch, with the bottom layer having twice as much starch as the top layer).

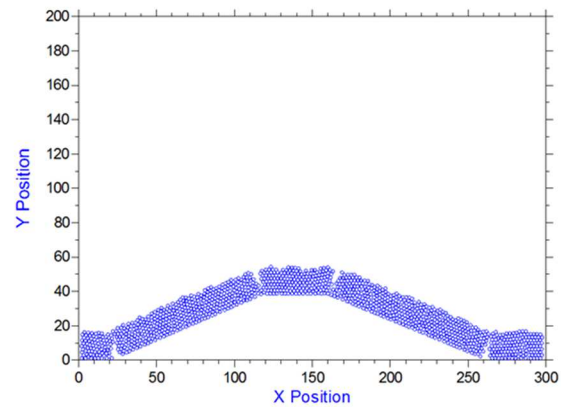


**Figure 5.10** Position plot for 62 PVC (20 pph binder) with binder properties that resemble 60% latex plus 40% starch (60L/40S) in a single layer (i.e., one starch rich layer equal in height to the two-layer scenarios).

### 5.5 Comparison to Experimental Data

The simulations of this paper show agreement with the trends observed in the literature. While the model was not concerned with finding the optimal balance between stiffness and CAF [as were

Salminen *et al.* (2008a and 2008b), Alam *et al.* (2009), and Yang *et al.* (2014)], the current simulations did show that cracking tendency would decrease with a thick, low-stiffness bottom layer and a thin, stiff top layer (i.e., conditions with an all-latex bottom layer and a top layer with some level of starch – the conditions with the highest strain-at-failure values). As noted earlier, the position plot of Figure 5.7 is an example of how the simulations agree with this past work. As stated above, these earlier investigators found their ideal paper to be a thin, stiff bottom coating layer, a thick, lower-stiffness middle coating layer, and a thin, stiff top coating layer. It may be that cracks form in the top coating layer in these systems, but they are not noticed because the middle coating layer (bottom layer in our case) does not crack or it dissipates the crack.

The tendency for the starch-rich layers in the model to be more prone to cracking was in accordance with Oh *et al.* (2014) who commented about the negative impact on cracking tendency when adding starch to the precoat (the topcoat was an all-latex binder system in their study). As stated previously, they found that the length and area of the cracks would increase directly with starch level. In addition, their data agreed with the results of Zhu *et al.* (2014) in that the strain-at-failure decreased and the maximum stress increased as more starch was added to the precoat. Since the model is concerned with two dimensions at present, definitive comments about the size and number of cracks cannot be made. However, the model does show agreement with the stress-strain data from Oh *et al.* (2014) for the simulations involving starch-containing precoats and an all-latex topcoat. The maximum stress goes up when the starch level is raised, be it from adding more to the precoat or from increasing the precoat weight. As for the strain-at-failure, this parameter drops with more starch but remains constant with increasing precoat weight. However, the position plot of Figure 8 shows the appearance of cracks in an all-latex top layer. These results are not in

agreement with Oh *et al.* (2014) even though the simulated stress-strain results follow the same trends as the prior experimental work.

Hashemi-Najafi *et al.* (2018) applied two coating layers to a couple of paper substrates. The coatings were formulated at two different PVCs and with the four binder systems used in the simulations above. Following bending, the area of the cracks was found to be a strong function of the amount of latex in the topcoat. The area was lower at higher levels of latex in the top layer binder system, indicating that cracking became less of an issue in this case. These results concur with the model in that cracking, in general, did not occur in the layers with an all-latex binder system. However, the simulated strain-at-failure results for the case of an all-latex topcoat (100L/0S) were not the highest in all cases, thus indicating that these conditions did not show the lowest propensity of cracking.

## **5.6 Conclusions**

A discrete element method model was found capable of simulating bending for a two-layer system comprised of different ratios of the two heights and of different binder systems in the two layers. The model could predict cracking during the three-point bending event. The model was based on using the mechanical properties obtained from pure binder films.

The model shows a direct relationship between starch level and height of a starch-rich layer on the flexural modulus and the maximum stress. For the case of strain-at-failure, the model shows the relationship to be the inverse case.

The trends shown by the model are in general agreement with the literature in that starch-rich coating layers of high coat weight were seen to be more prone to cracking. Additionally, the lowest tendency for cracking was seen for a thick bottom layer of an all-latex binder system with a thinner top layer of a starch-containing coating.

More work needs to be performed to improve the model's predictions relative to experimental results. Possible ideas to pursue include the impact of starch on the mode of failure (cohesive vs. adhesive) and true three-dimensional packing.

## CHAPTER SIX

### DISCRETE ELEMENT METHOD TO MODEL INLINE TENSION AND THREE-POINT BENDING EVENTS FOR SINGLE LAYER THREE DIMENSION SYSTEMS OF UNIFORM SPHERES

#### 6.1 Abstract

The mechanical properties of paper coating layers are important in converting operations such as slitting, calendaring, printing and, folding. While a number of experimental and theoretical studies have advanced our knowledge of these systems, a good particle level understanding of issues like crack at the fold are lacking.

In this paper, a discrete element method (DEM) model has been modified to account for three dimensions. Simulations were run for both in-line tension and for three-point bending of single layer systems. As with past models, inputs to the 3D version include properties of the pure binder film and the binder concentration. The model predicts crack formation as a function of these parameters and can also calculate the modulus, the maximum stress, and the strain-at-failure. The simulation results were compared to the work of Zhu *et al.* (2014) and of Hashemi-Najafi *et al.* (2018). Good predictions are obtained for both tensile and bending for a range of latex-starch ratios and at various pigment concentrations.

#### 6.2 Introduction

The mechanical properties of coatings are important in a number of applications. For coated papers, the resistance to picking during the printing operation is critical as well as is the ability for the sample to be converted or folded without cracking of the coating layer [Sim *et al.* (2012) and Barbier *et al.* (2012)]. The increased use of starch as a binder is of interest as the industry tries to

move to natural binders, but starch often increases cracking problems as reported by Rättö and Hornatowska (2010) and Oh *et al.* (2015). If the coating layer is a homogenous material, such as a specific polymer, the mechanical properties of the layer can be estimated from the bulk properties of that material. However, when the coating layer is a composite of pigments and binder, the mechanical properties are more difficult to predict.

Finite element methods (FEM) can be used to predict the deformation of coated paper by treating the coating layer as a continuum [Barbier *et al.* (2005) and Alam *et al.* (2009)]. The compressive and tensile stresses during bending can be predicted. However, the elastic modulus and the Poisson ratio are inputs of the model; these would need to be measured for each sample because they would depend on the latex type, starch loading, and the paper fiber properties. These methods also do not lead to insight as to the mechanism of crack formation.

Some continuum type models have been explored by modeling groups of particles connected by polymeric bridges (Rättö, 2004). When the number of particles increase and the distance between particles is small, numerical analysis of this nature are costly. While some insight into mechanical properties of porous composites has been obtained with a mesh-free continuum mechanics simulation (Toivakka *et al.* 2015), an understanding of the micromechanical behavior of pigmented coating layers in various industrially relevant situations is lacking.

Discrete element methods (DEM) are based on the particle length scale and have potential to reveal particle level mechanisms in the study of these systems. Toivakka and Bousfield (2001) proposed a simple model to predict the dynamic mechanical properties of a pigmented coating layer in

tension and compared the simulation results to experimental data. DEM has been used to study the compression of paper coatings during the calendaring event (Azadi *et al.* 2008). Tensile and bending predictions also have been reported previously by Varney and Bousfield (2016a, 2016b, 2017, and 2018). While most of these models are two dimensional in nature except Azadi *et al.* (2008); a good comparison between 2D and 3D models has not been reported.

In this current paper, the authors propose to use a particle level 3D model to understand the tensile and bending behavior of coating layers that contain pigments, latex, and starch. The results are compared to the experimental data of Zhu *et al.* (2014), of Chen *et al.* (2014), and of Najafi *et al.* (2018). Latex and starch mixtures were used as a binder between ground calcium carbonate pigments in these experiments and the mechanical properties of these starch-latex mixtures are inputs into the model. The predictions of two and three dimensional forms of the model are compared along with the experimental values.

### 6.3 Model Description

When two particles move relative to each other as in Figure 6.1 (similar to in-line tension), a restoring force is calculated to pull them together based on the local strain of the polymer between them. The force equation used here takes on the non-linear form

$$F = A(1 - e^{-B\varepsilon})\pi R_b^2 \quad (6.1)$$

where  $F$  is the tensile force between particles,  $A$  and  $B$  are parameters that depend on the pure binder properties,  $\varepsilon$  is the local strain between particles, and  $R_b$  is the radius of the binder bridge between particles. The bridge radius and the spacing of the particle depends on the pigment volume

fraction (PVC), which is defined as the ratio of the total volume of pigments to the volume of pigments plus the volume of binder. The relationship between the PVC and the binder bridge radius was discussed by Varney and Bousfield (2016a). In this work, the binder bridge radius was found to fit the equation below, where the PVC is above the critical value.

$$R_b = (3.1 - 3.1PVC)^{0.25} \quad (6.2)$$

Note that the bridge radius goes to zero as PVC goes to 1.0, which is a system that has no binder. Below the critical PVC, the binder bridge radius is 1.0, but the particle separation would increase. This value represents a system that is full of binder everywhere.

When the predicted local strain between particles is larger than the strain-to-failure measured for the pure binder, the binder is assumed to fail cohesively and the force is set to zero. This non-linear form for the force equation (6.1) is selected because it resembles the behavior of the tensile tests of the binder films as reported by Prall *et al.* (2000) and Raman *et al.* (1998). The model can also account for adhesive failure by putting a strain or stress criteria in the calculation.

The mechanical properties of the binder films are possible to measure from tensile tests. Zhu *et al.* (2014) and Najafi *et al.* (2018) report the mechanical properties of mixtures of starch and latex. The maximum stress at failure is the parameter A in equation (6.1). The elastic modulus divided by A is the parameter B in equation (6.1) because the initial slope of equation (6.1) is the product of A and B. Table 6.1 shows the mechanical properties of these films produced from mixtures of latex and starch. As is well known, as starch is added to these systems, the elastic modulus of the binder increases but the strain at failure decreases.

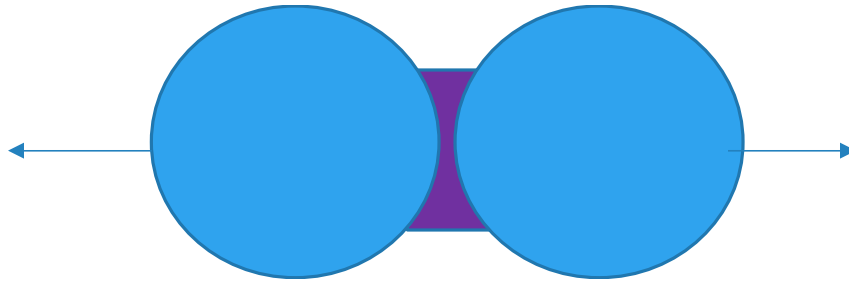


**Figure 6.1** Idealized system of two spherical pigments connected together by a binder bridge. The binders of interest here are mixtures of starch and latex.  $R_b$  is the binder bridge radius and  $h$  is the height of the binder bridge.

**Table 6.1** Mechanical properties of particle free films composed of mixtures of starch and latex.

Investigator	Weight Fraction Latex (Parts)	A (MPa)	B	E (MPa)	STF (%)
Najafi <i>et al.</i>	100	1.5	2	3	200
Najafi <i>et al.</i>	80	4.9	15	73.5	80
Najafi <i>et al.</i>	60	4.8	35	168	22
Najafi <i>et al.</i>	40	11.0	60	660	5
Zhu <i>et al.</i>	100	3.75	3.2	12	355
Zhu <i>et al.</i>	77	9.4	24	221	200
Zhu <i>et al.</i>	58	15.5	29	448	41
Zhu <i>et al.</i>	38	32.0	36	1156	13

If particles move closer to each other compared to the initial gap (compression), a repulsive force is applied to keep the particles from overlapping. This repulsive force is linear and depends on the compressive strain as  $F = C\epsilon$ , where  $C$  is some constant and the strain is the current gap between particles divided by the initial gap. The value of  $C$  must be large enough to prevent the particles from overlapping, but not to impact the final results.

One parameter included in the model is the distance between two particles to consider them neighbors and, thus, to have a connection. Some have termed this concept “nearest neighbors”. At the Critical Pigment Volume Concentration (CPVC), every particle should be close to several others. However, it is not clear at what distance particles should be considered connected. In Figure 6.2, if the gap between the particle of interest and the other particles, is less than one radius, the particles will be considered neighbors and, therefore, be connected. If they are too far away, then no connection is assumed.

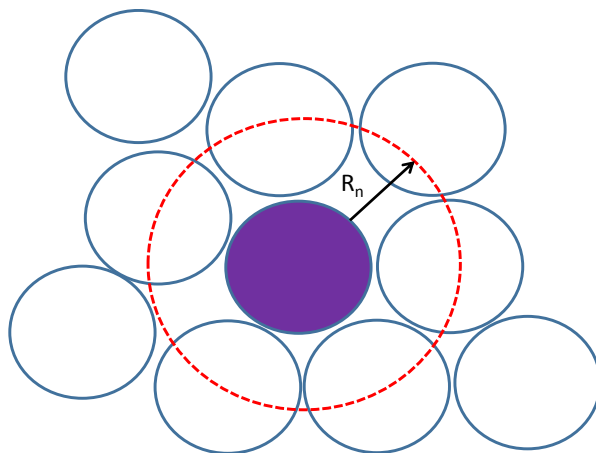


**Figure 6.2 Near neighbor criteria with  $R_n=1.0$ . Particles closer than the criteria are assumed to be connected. As  $R_n$  increases, more particles are connected together.**

For the 2D model, spheres are assumed to be confined to a monolayer, as depicted in Figure 6.3. Spheres are “pressed” into the region during the initial packing, keeping the minimum separation of spheres to be around 0.5% of the radius. In the 3D case, depicted in Figure 6.4, spheres are packed into the structure using a Brownian motion type simulation, where particle motion is accepted for minimizing the gap between particles. In either case, the particles are packed into a

structure that would represent the coatings at low binder content, where most particles will have a number of near neighbors. For low pigment volume concentrations, the initial packing should be much lower. These cases can be calculated by using the same packing, but assuming that the particles have a radius less than what is used to pack the structures near CPVC.

To simulate an in-line tensile event, particles in the grip region on the right of the figure are set to a velocity of one dimensionless unit value to the right. Particles in the left grip region are assigned to no velocity. This scenario causes the particles on the right to pull on other particles in the middle of the structure and transmit forces throughout the structure. The up zone is not used in tension. The results presented here are for slow motions relative to the inertia of the particles. Therefore, the forces are near equilibrium during the deformation event and the rate of deformation is not important.

To stabilize the simulation when a crack occurs, it was found helpful to add a small damping factor, where a particle moving at some velocity will experience a force in the opposite direction. The equation is  $F = -DV$ , where  $D$  is a damp factor and  $V$  is the velocity vector. The value of the damping factor should be small enough so as not to influence the predictions of the modulus or of the ultimate stress.

To simulate bending tests, particles in the “push up” zone are assigned an upward velocity (i.e., the particles are pushed upwards from below this zone). For the results here, the push up zone has a width of 10 units which is smaller than depicted in the figure. The sizes of the two grip zones and of push up zone have minimal influence on the results as long as the distance from the zones is large compared to the zones themselves. Similar conditions are set for the 3D model – the

bending of a 3D case is shown in Figure 6.4. Spheres on the two sides (the grip zones) of the simulation are not allowed to move in the vertical direction, but they are allowed to slide in the horizontal direction or deflect downward.

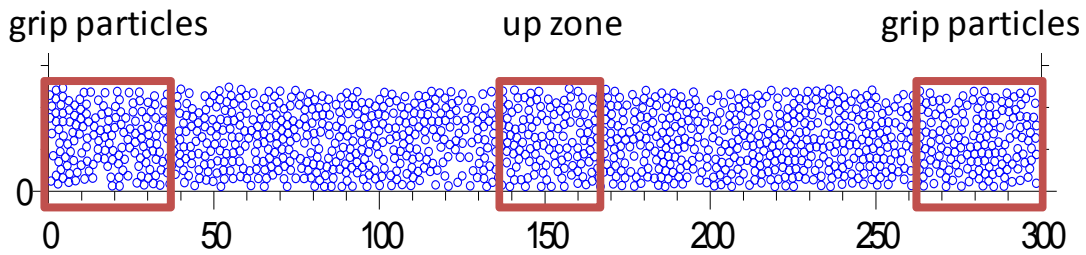


**Figure 6.3 Simulation set up for the 2D model for the three point bending case for 30x300 matrix (the particles are pushed up from the bottom in the “push up” zone).**

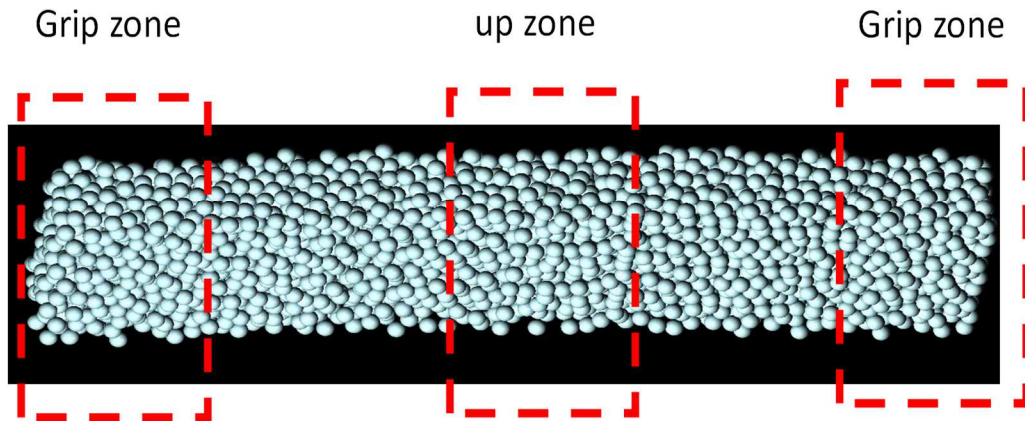


**Figure 6.4 3D situation for uniform spheres packed in a 10x10x100 cell. Particles here have undergone some upward deflection. Particles are packed to a PVC of 64%.**

In both cases, as some particles are forced to move from their equilibrium position, a vector force on neighboring particles is calculated using either equation (6.1) or the compression equation ( $F = C\varepsilon$ ). The net force on every particle is calculated based on its position and the position of all of the neighbors. This net force is used to update particle velocities and positions with a numerical

integration using a predictor-corrector method. In the results presented in this paper, the motion is slow and the inertia terms are small; time or rates do not influence the results, but these effects are straight forward to include in the future. These time integrations can be expressed as

$$\begin{aligned} a &= dV / dt = F / x_m \\ dP / dt &= V \end{aligned} \tag{6.3}$$

where  $a$  is acceleration,  $V$  is velocity,  $F$  is force,  $x_m$  is a parameter that represents the mass of the particle, and  $P$  is position. Equation (6.4) is a vector equation because it has components in each dimension.

The sum of the forces on the particles that move relate to the force a mechanical tester would record; these forces balance the sum of the forces on the particles that are not allowed to move. In tension, the stress is the sum of the forces on the grip particles divided by the cross sectional area. In 2D, the distance into the paper is assumed to be one particle diameter. The flexural stress and strain can be calculated as

$$\sigma_f = \frac{3PL}{2bd^2} \tag{6.4}$$

$$\varepsilon_f = \frac{6Dd}{L^2} \tag{6.5}$$

where  $P$  is the sum of the forces on the two grip particles (or the load force),  $L$  is the distance between grips,  $D$  is the displacement of the upward moving particles at the center of the sample,  $b$  is the width of the sample and  $d$  is the thickness of the sample. The goal is to predict the bending behavior and the crack propagation of these systems.

A typical bending result is shown in Figure 6.5. As a group of particles moves from the initial position, the forces are transmitted through the particles to generate a force throughout the sample. At some point, the local strain of the sample exceeds the strain to failure of the pure binder, a crack propagates, and the sample breaks. This general behavior and the shape of the response are quite similar to the experimental data. The model predicts the elastic modulus of the coating layer from the initial slope of the response as well as the maximum stress and the strain to failure.

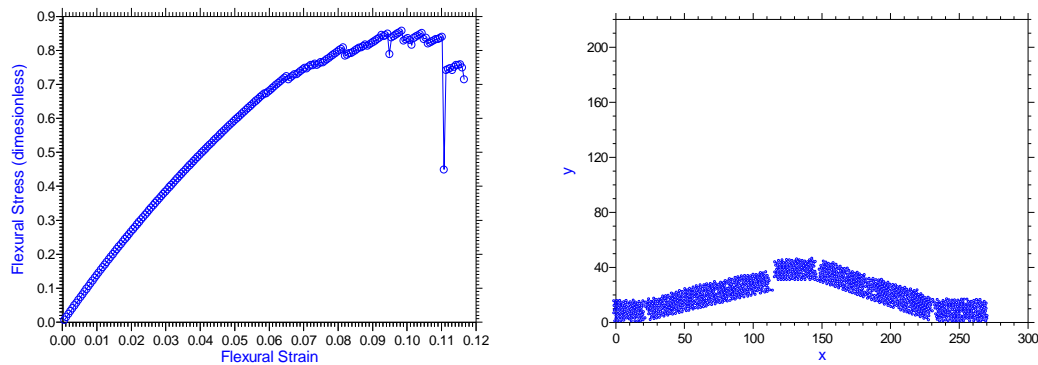


**Figure 6.5 Flexural strain and stress predicted by the simulation (left) and crack of the coating layer (right) for a 2D example.**

The deformation and local forces for a typical 3D case are shown in Figure 6.6. In the region that is forced upward, a tensile force is generated. Also, near the regions where particles are only allowed to slip in the horizontal direction (the grip zones), a tensile force is generated between particles.

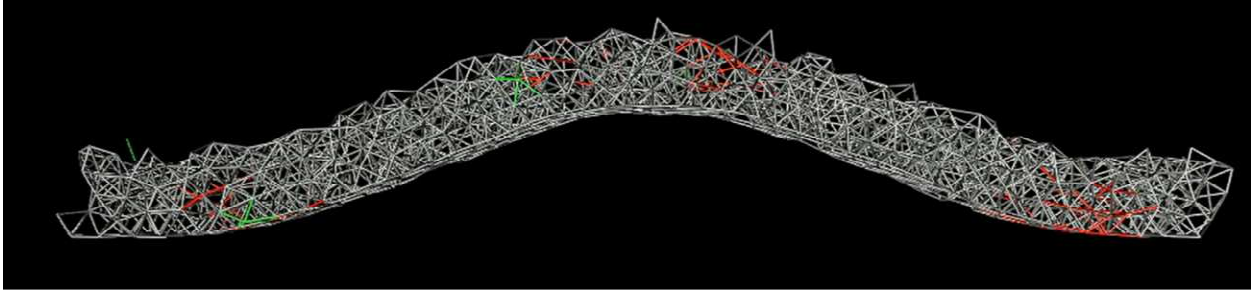


**Figure 6.6 Bending deformation in 3D mode, showing the connections between particles for a typical case.**

## 6.4 Results

The value of  $C$  is found to not strongly influence the results as long as it is large enough to prevent particles from overlapping. In tension simulations especially, the value of  $C$  has little influence. Figures 6.7 – 6.9 show how the parameter  $C$  influences the mechanical properties for different values of a damping factor for a bending simulation. These plots were produced for 3D bending with a set value of  $R_n$  of 1.0 and an  $x_m$  of  $5.0 \times 10^{-5}$  using mono-disperse spheres. The model in the current form neglects the viscous effects and shear effects, but these factors can be incorporated in a straight forward way if needed. As  $C$  increases, the flexural modulus increases, but the maximum stress and the strain to failure are little influenced. And, as  $C$  increases, particles are not able to move towards each other. In bending, this situation would cause particles on the top side of the sample to move more than cases where  $C$  is small for a set flexural strain – the net results is that increasing  $C$  increases the elastic modulus. Based on these result, a value of 500 was used for  $C$  in the simulations.

Figures 6.7 – 6.9 also show that a damping factor of 0.01 does not influence the results, but if the damping factor is larger than this value, the predictions are influenced. The damp factor was set to 0.001 for most of the predictions.

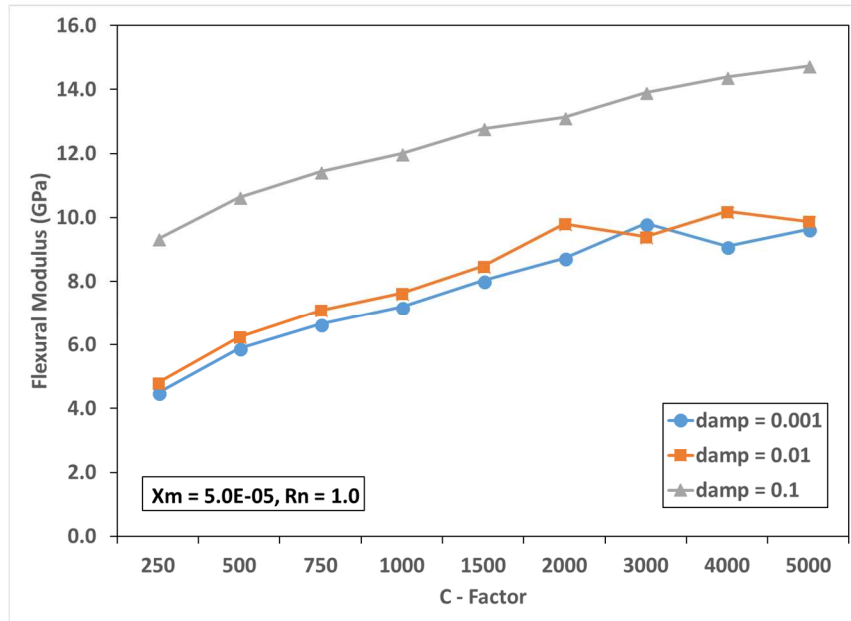


Figure 6.7 Flexural modulus vs. C-factor at various values of damping factor using monodisperse spherical particles.

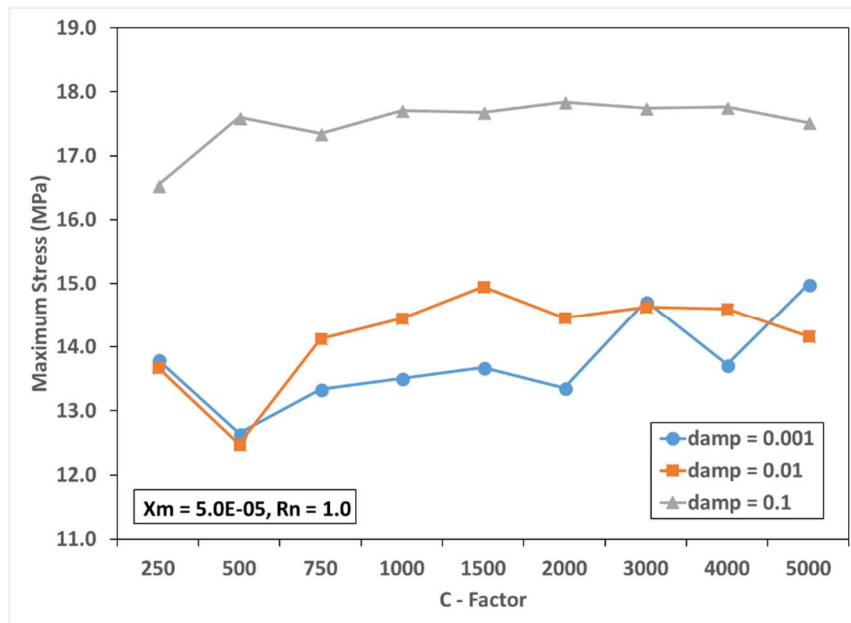
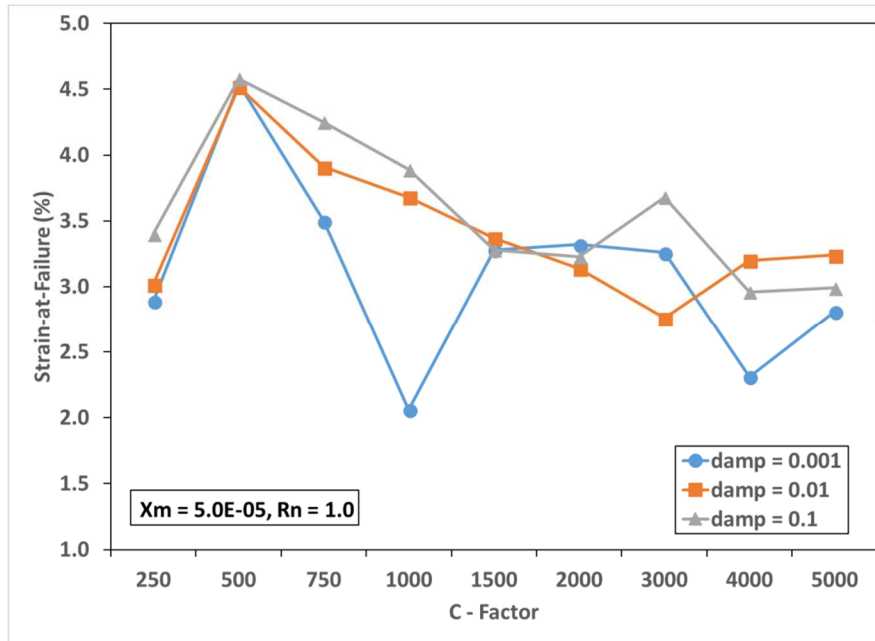
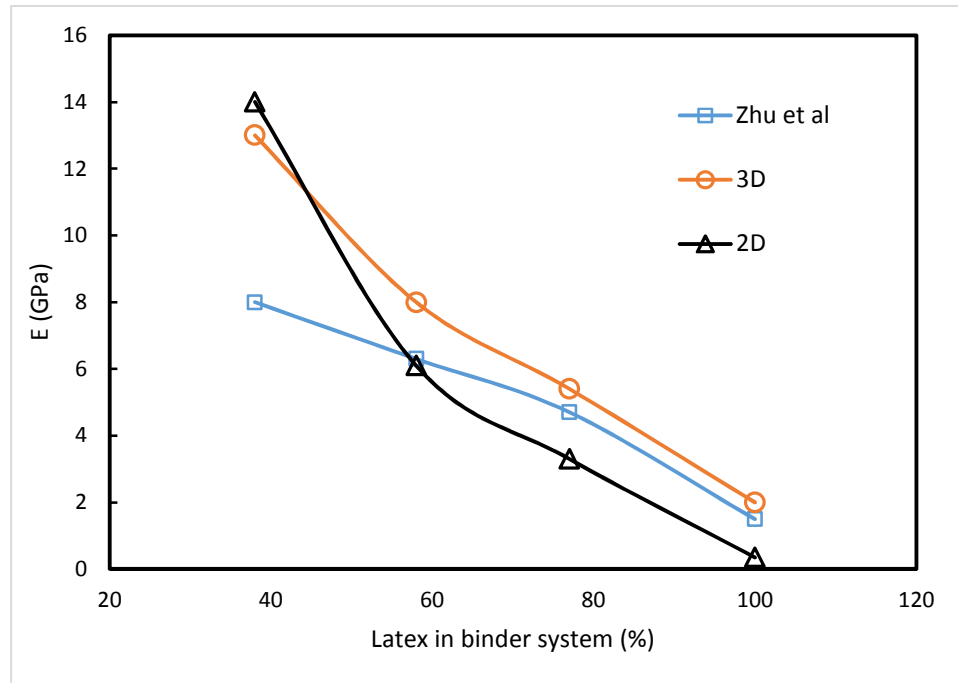


Figure 6.8 Flexural maximum stress vs. C-factor at various values of damping factor using monodisperse spherical particles.



**Figure 6.9 Flexural strain at failure vs. C-factor at various values of damping factor using monodisperse spherical particles.**

The predictions of the models are compared to the tensile experimental data of Zhu *et al.* (2014) in Figures 6.10 – 6.12 for the PVC near the critical value of about 63% by volume of pigment. The model predictions are for  $R_n = 1.0$  and  $R_b = 1.0$ . The different ratios of latex and starch results in different values of  $A$  and  $B$  in equation (1) as well as a different strain to failure of the binder itself. Both the 2D and 3D models predict the elastic modulus well considering the assumptions of the model. The predicted elastic modulus is on the order of 20 times larger than the pure binder films, given in Table 6.1. As the binder contains more latex, the elastic modulus decreases, mirroring the pure binder behavior.



**Figure 6.10 Elastic modulus of coating layers in tension for PVC = 63% for various values of the starch and latex content in the binder system. 3D closer by 12% vs. 2D.**

The maximum stress or the stress at failure is under predicted by both the 2D and 3D models as shown in Figure 6.11. The experimental data shows a maximum value at middle values of latex content. It is possible that the decrease in maximum stress at low latex content could be caused by issues related to mounting a brittle sample into the tensile test, as discussed by Zhu *et al.* (2014). The predictions of the strain at failure are shown in Figure 6.12. The 3D model picks up the experimental results quite well, but the 2D predictions are quite low. The potential for a crack to form in tension comes from a weak region in the model system. In 2D, the probability of a weak area increases because of the fewer numbers of particles and the lower connectivity to neighboring particles when compared to 3D case.

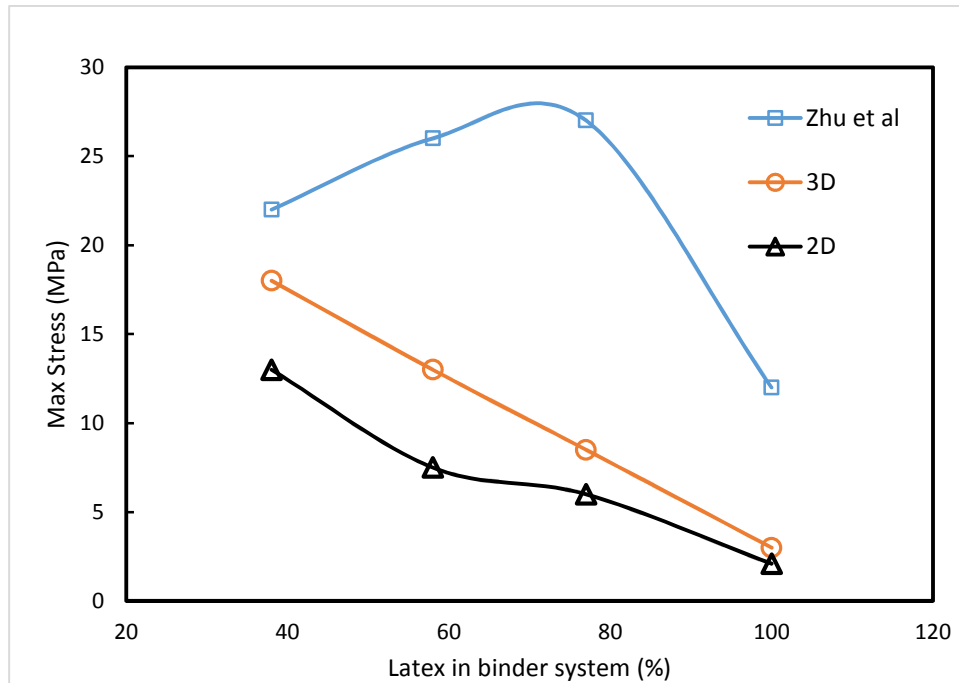


**Figure 6.11 Predictions of the stress at failure for the coating layers in tension for PVC = 63% for various levels of latex and starch in the binder system. 3D closer by 24% vs. 2D.**

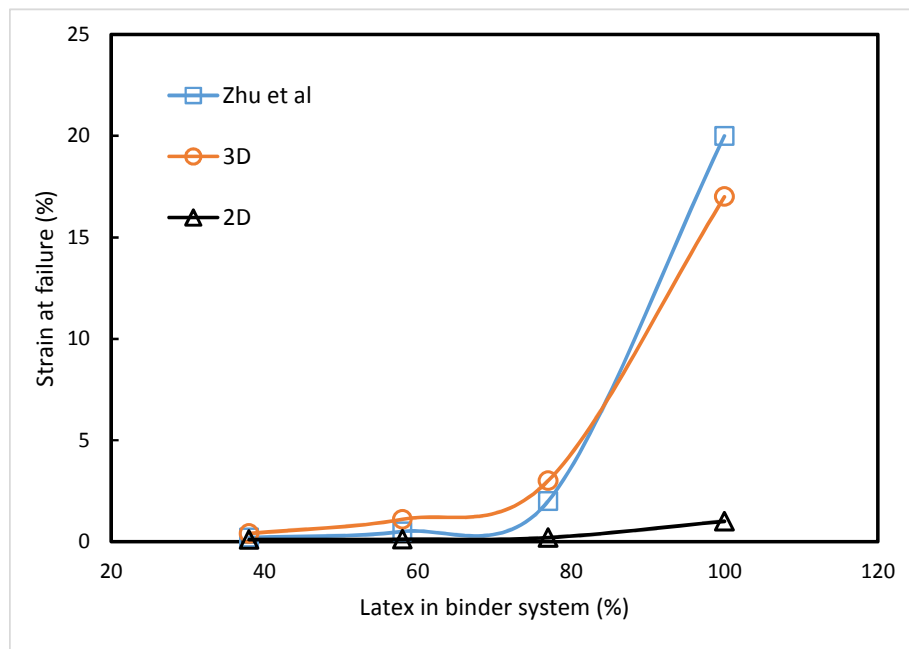


**Figure 6.12 Predictions of the stress at failure for the coating layers in tension for PVC = 63% for various levels of latex and starch in the binder system. 3D closer by 77% vs. 2D.**

The 2D and 3D predicted flexural modulus, maximum stress, and strain at failure as well as the experimental data of Hashemi-Najafi *et al.* (2018) for various latex content of the binder system are all shown in Figures 6.13 – 6.15. Both the 2D and 3D models predict the correct trends – as the latex content decreases, the coatings become more brittle. The 2D model underpredicts the elastic modulus and the maximum stress a significant amount. If the value of  $R_n$  is increased, better predictions are obtained. The 2D situation has fewer connections between particles than the 3D case. Both models over predict the strain to failure, in Figure. 6.15; this result may be due to minor imperfections in the coating layers in the experiments, causing the samples to fail earlier than they would in theory. Considering the assumptions in the model and the simple interactions between particles, these predictions are encouraging.

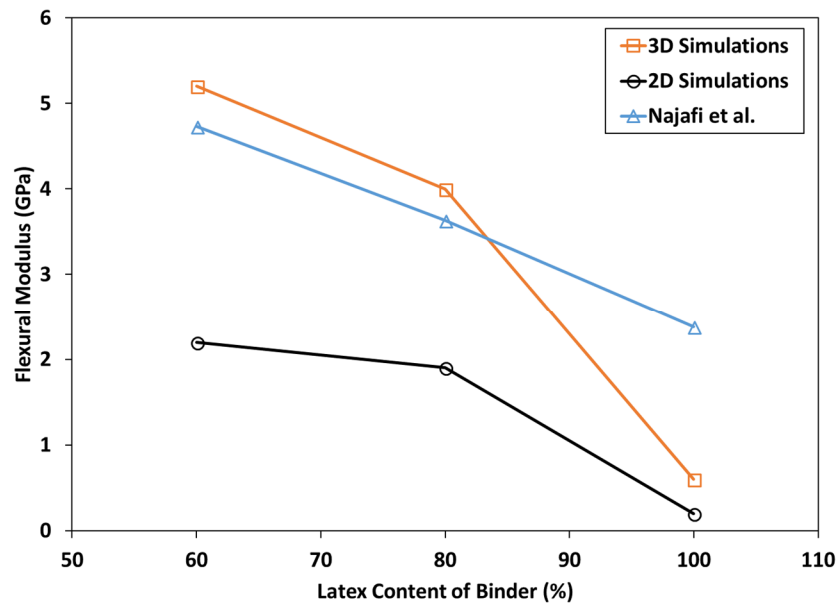


**Figure 6.13 Predicted and measured flexural modulus for the coating layer near PVC of 63% for binder components of various levels of starch and latex. 3D closer by 59% vs. 2D.**

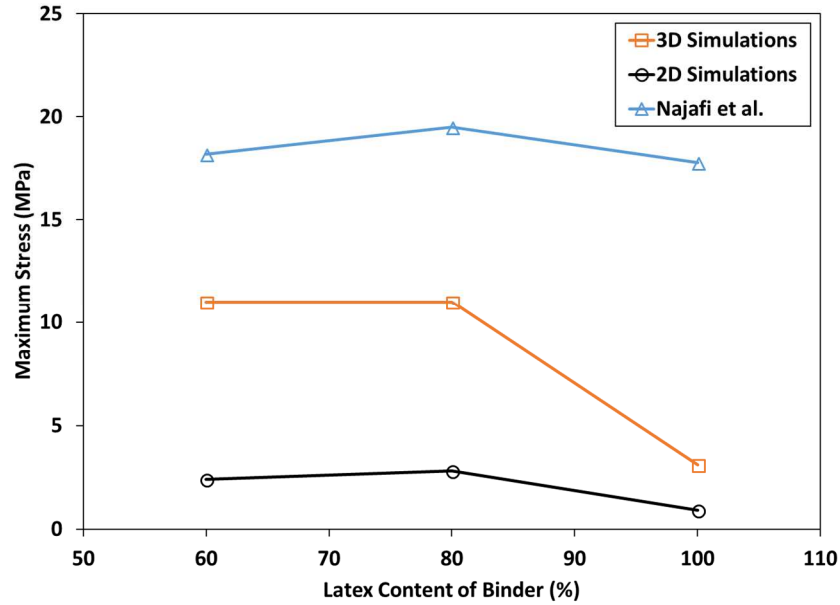


**Figure 6.14** Maximum stress at failure for coating layers near PVC of 63% for various levels of latex and starch in the binder composition. 3D closer by 38% vs. 2D.

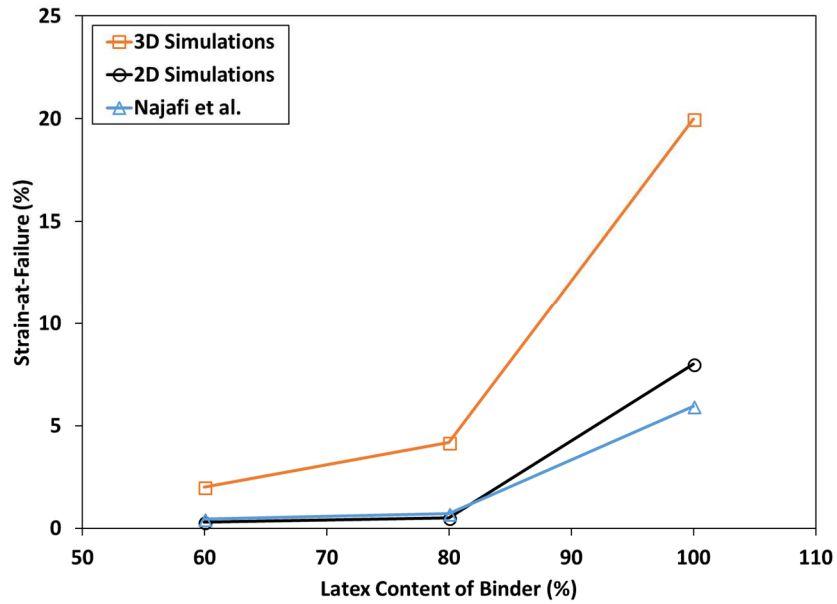


**Figure 6.15** Predicted and measured strain at failure for coating layers near PVC of 63% for various levels of latex and starch in the binder composition. 2D closer by 87% vs. 3D.

As seen in Figures 6.10 – 6.15, the move from 2D to 3D (uniform spheres) offered significant improvements in the model’s ability to approximate the experimental data. These 3D gains ranged from 12% to 77% vs. the 2D conditions for all properties with both in-line tension and three-point bending (save for the strain-at-failure with three-point bending, where the 2D STF results were much closer to the lab data).

Figures 6.16 – 6.18 show the comparison of the model for the two different PVC concentrations of Najafi *et al.* (2018). The binder bridge radius, for PVC of 78%, is 90 percent of the particle radius based on equation (2) above. This value reduces the modulus predictions and the maximum stress predictions around that factor, but the strain to failure remains quite similar. The experimental data at PVC of 78% is nearly 60% of the data at 63%: this lower value is closer to the model predictions than the 63% case. The predictions of the 40% latex level are shown, but experimental value could not be obtained due to the brittle nature of the samples.

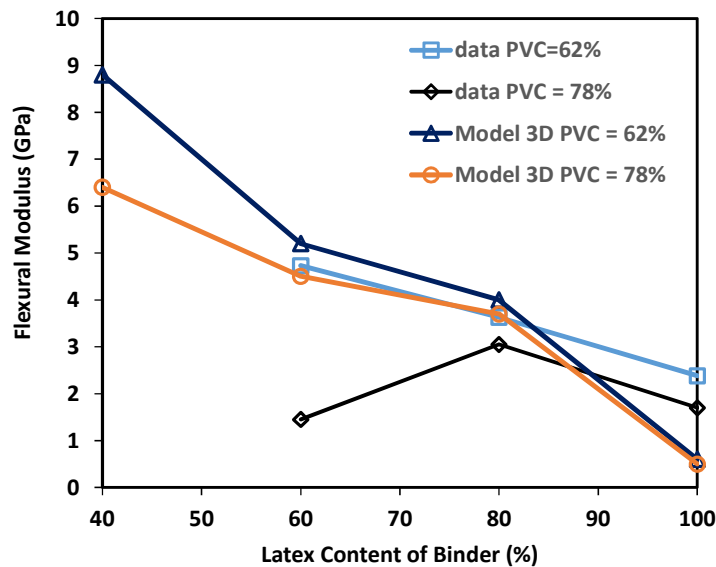


**Figure 6.16 Flexural modulus predictions and experimental results of Najafi *et al.* (2018).**

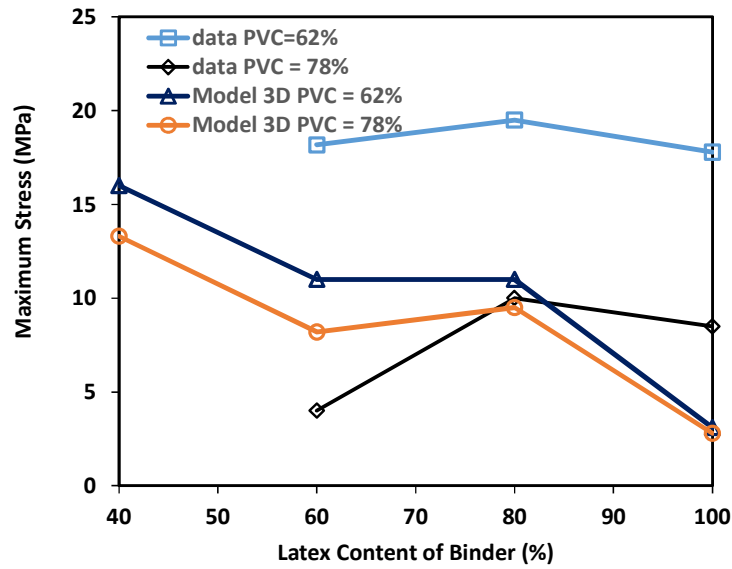


**Figure 6.17** Maximum stress predictions for two different PVC values and the predictions.

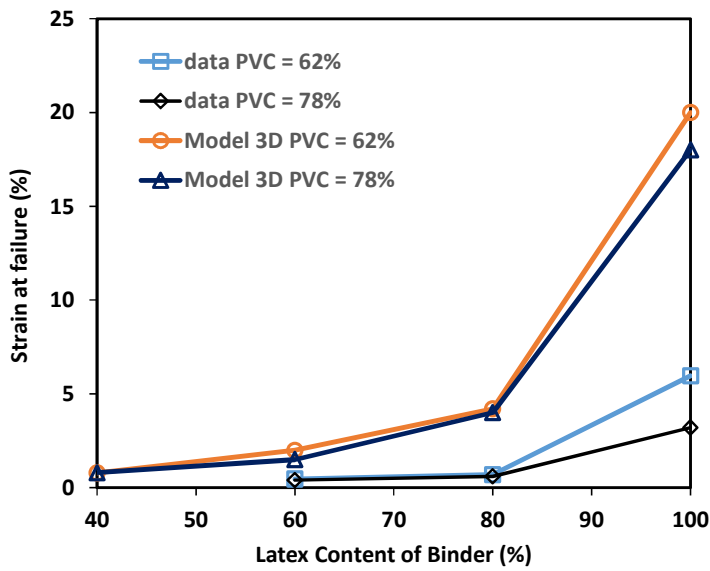


**Figure 6.18** The strain at failure predictions and data for two PVC values.

In both tension and flexural deformation, the model under predicts the maximum stress or the stress at failure with the exception of the 78% PVC flexural case. This under prediction is hard to

explain, especially for the 3D case. The maximum stress between each particle pair summed across the cross section would control this prediction. In some way, the real system seems to make more connections than predicted with  $R_n=1.0$ . In a system with a broad particle size distribution, as in the experiments, it is possible that the particles can make more connections. The inclusion of a broad particle size distribution is straight forward and is the subject of our current work.

The influence of the  $R_n$  factor is demonstrated in Figures 6.19 – 6.21. The value of  $R_n$  influenced the elastic modulus predictions a small amount. However, the maximum stress and strain to failure are strongly influenced. In fact, the maximum stress is now over predicted with  $R_n = 1.5$ . This result must come from the increased number of connections between particles that can support a higher strain value. Therefore, a better prediction of the maximum stress could be obtained with a value of  $R_n$  around 1.25, but now the strain to failure is over predicted.

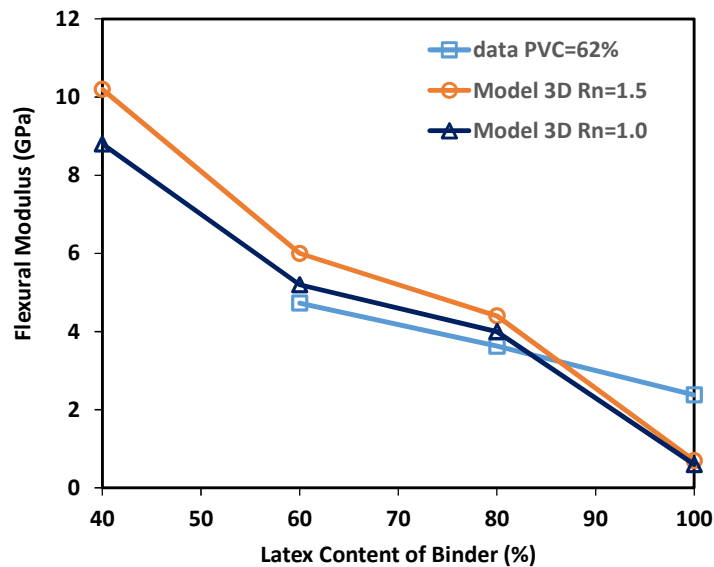


**Figure 6.19 Comparison of  $R_n$  value on model modulus predictions for the PVC 63% case.**

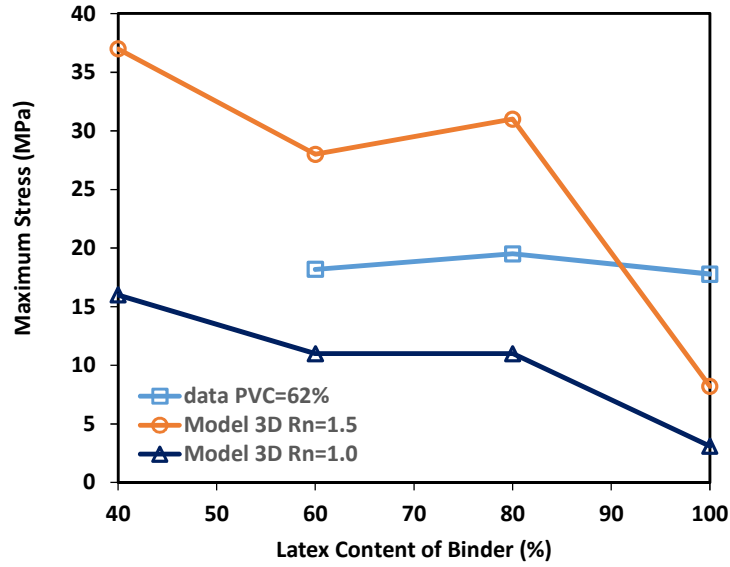


Figure 6.20 Comparison of model predictions for maximum stress for two values of  $R_n$ .

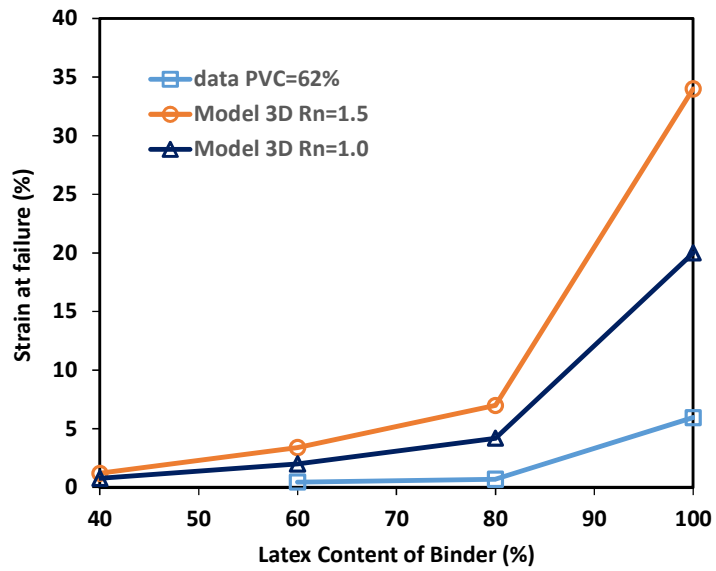


Figure 6.21 Comparison of predictions of strain at failure for two values of  $R_n$ .

A number of assumptions are used in these simulations to simplify the model. This list includes perfect adhesion between the binder and the pigment, the initial packing of the particles being

similar to that of the real case, and the starch and latex forming a uniform material (Chen *et al.* in 2014 discuss this topic in detail). In addition, these results are for uniform spherical particles while pigments in the experiments have a wide size distribution.

The model is flexible for other situations. If a normal downward load is applied to the top layer of the particles, a calendering event would be modeled. If a load is applied vertically to a layer of the particles (in a pull up zone), the tensile event during printing could be simulated. If multiple coating layers are of interest, the parameters for each layer could be specified. The inclusion of particle inertia is natural to model high speed events. Even complex processing, such as slitting, could be modeled.

## **6.5 Conclusions**

A discrete element method based model is developed to predict the mechanical properties of pigmented coating layers. The model parameters are the mechanical properties of the binder and the pigment volume concentration. The model gives reasonable predictions in both tensile and flexural tests and does predict all of the correct trends. The 3D model improves the predictions compared to the 2D model. The elastic modulus is quite well predicted in both tension and bending, but the maximum stress is under predicted except for the 78% PVC case. The strain at failure tends to be over predicted. Including a full particle size distribution may improve predictions of real systems.

## CHAPTER SEVEN

### DISCRETE ELEMENT METHOD TO MODEL INLINE TENSION AND THREE-POINT BENDING EVENTS FOR SINGLE LAYER THREE DIMENSION SYSTEMS WITH BIMODAL AND FULL PARTICLE SIZE DISTRIBUTIONS OF SPHERICAL PARTICLES

#### 7.1 Abstract

The mechanical properties of paper coating layers are important in converting operations such as calendaring, printing and, folding. While a number of experimental and theoretical studies have advanced our knowledge of these systems, a good particle level understanding of issues like crack at the fold are lacking.

In this paper, the three dimension version of the discrete element method (DEM) model of Varney *et al.* (2019) has been modified. The particles used in the model have been expanded from the standard monodisperse packing of spherical particles to bimodal distributions of spherical particles and also to pseudo-full particle size distributions of spherical particles. In making this upgrade to the model, the impact of particle size distribution on the mechanical properties of the coating layer could be studied.

Simulations were run for both in-line tension and for three-point bending of single layer systems. As with past models, inputs to the 3D version include properties of the pure binder film and the binder concentration. The model predicts crack formation as a function of these parameters and can also calculate the modulus, the maximum stress, and the strain-at-failure. The simulation results were compared to the work of Zhu *et al.* (2014) and of Hashemi-Najafi *et al.* (2018). Good predictions were obtained for both tensile and bending for a range of latex-starch ratios and at

various pigment concentrations. In addition, the model predicted the correct trends and order of magnitude relative to the experimental data.

## **7.2 Introduction**

The mechanical properties of coatings are important in a number of applications. For coated papers, the resistance to picking during the printing operation is critical as well as is the ability for the sample to be converted or folded without cracking of the coating layer [Sim *et al.* (2012) and Barbier *et al.* (2012)]. The increased use of starch as a binder is of interest as the industry tries to move to natural binders, but starch often increases cracking problems as reported by Rättö and Hornatowska (2010) and Oh *et al.* (2015). If the coating layer is a homogenous material, such as a specific polymer, the mechanical properties of the layer can be estimated from the bulk properties of that material. However, when the coating layer is a composite of pigments and binder, the mechanical properties are more difficult to predict.

Finite element methods (FEM) can be used to simulate the deformation of coated paper by treating the coating layer as a continuum [Barbier *et al.* (2005) and Alam *et al.* (2009)]. The compressive and tensile stresses during bending can be predicted. The elastic modulus and the Poisson ratio are inputs to these models and would need to be measured for each sample because they would depend on the latex type, starch loading, and the paper fiber properties. One drawback of FEM is that it does not lead to particle scale insights of the mechanism of crack formation.

Some continuum type models have been explored by modeling groups of particles connected by polymeric bridges (Rättö, 2004). When the number of particles increase and the distance between

particles is small, numerical analysis of this nature are costly. While some insight into mechanical properties of porous composites has been obtained with a mesh-free continuum mechanics simulation (Toivakka *et al.* 2015), an understanding of micromechanical behavior of pigmented coating layers in various industrially relevant situations is lacking.

Discrete element methods (DEM) are based on the particle length scale and have potential to reveal particle level mechanisms in the study of these systems. Toivakka and Bousfield (2001) proposed a simple model to predict the dynamic mechanical properties of a pigmented coating layer in tension and compared the simulation results to experimental data. DEM has been used to study the compression of paper coatings during the calendaring event (Azadi *et al.* 2008). Tensile and bending predictions also have been reported previously by Varney and Bousfield (2016a, 2016b, 2017, and 2018). Since most of these models are two dimensional in nature except Azadi *et al.* (2008), a good comparison between 2D and 3D models has not been reported.

While much of the past 3D DEM work has involved the use of monodisperse spherical particles [Ratto (2004), Varney *et al.* (2019)], some of the prior work has used other shapes and particle size distributions. Azadi *et al.* (2008a) used spherical particles similar in size and distribution to two GCCs (60 w/w% < 2 microns and 90 w/w% < 2 microns) plus a hypothetical pigment with a bimodal distribution. In a second study, Azadi *et al.* (2008b) used commercially available software to model spherical, needle-like, and platy particles. The latter two shapes were modeled as a collection of spherical particles “attached” to each other. Two particle size distributions were modeled for each particle shape – monodisperse and polydisperse. Other investigators used multiple size distributions for 2D DEM work [Alam *et al.* (2012)] and with the FEM [Alam *et al.*

(2008) and Alam and Toivakka (2012)]. The later work studied spherical as well as platy particles in their model.

In this current chapter, the authors propose to use a particle level model to understand the tensile and bending behavior of a coating layer that contains pigment, latex, and starch. Two different particle size distributions for the spherical pigments will be evaluated – bimodal and pseudo-full distributions. The results are compared with experimental data from Zhu *et al.* (2014) and from Najafi *et al.* (2018). Latex and starch mixtures were used as a binder between ground calcium carbonate pigments in these experiments and the mechanical properties of these starch-latex mixtures are inputs into the model. The predictions of three dimensional forms of the model are compared along with the experimental values for two pigment volume concentrations (PVCs).

### 7.3 Model Description

When two pigments move relative to each other as in the example of in-line tension shown in Figure 7.1, a restoring force is calculated to pull them together based on the local strain of the polymer between them.

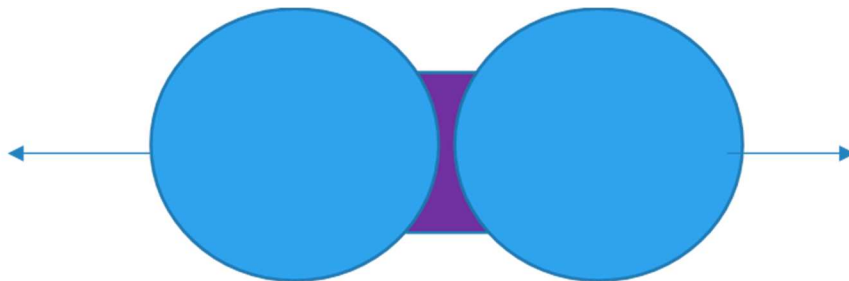


**Figure 7.1 Idealized system of two spherical pigments connected together by a binder bridge. The binders of interest here are mixtures of starch and latex.  $R_b$  is the binder bridge radius and  $h$  is the height of the binder bridge.**

The force equation used here takes on the non-linear form

$$F = A(1 - e^{-B\varepsilon})\pi R_b^2 \quad (7.1)$$

where  $F$  is the tensile force between particles,  $A$  and  $B$  are parameters that depend on the pure binder properties,  $\varepsilon$  is the local strain between particles, and  $R_b$  is the radius of the binder bridge between particles [Varney and Bousfield (2016a)]. The bridge radius and the spacing of the particles depends on the pigment volume fraction (PVC), which is defined as the ratio of total volume of pigments to the volume of pigments plus the volume of binder. The relationship between the PVC and the binder bridge radius was discussed by Varney and Bousfield (2016a). In this work, the binder bridge radius was found to fit the equation below, when the PVC is above the critical value.

$$R_b = (3.1 - 3.1PVC)^{0.25} \quad (7.2)$$

Note that the bridge radius goes to zero as PVC goes to 1.0, which is a system that has no binder. Below the critical PVC, the binder bridge radius is equal to the particle radius (which is set to a dimensionless value of 1.0). As such, the particle separation would increase as the PVC decreases. This value represents a system that is full of binder everywhere.

When the local strain between particles is larger than the strain-to-failure of the binder, the binder is assumed to fail cohesively and the force is set to zero. The non-linear form for the force equation (7.1) is selected because it resembles the behavior of the tensile tests of the binder films as reported

by Prall *et al.* (2000) and Raman *et al.* (1998). The model can also account for adhesive failure by putting a strain or stress criteria in the calculation.

The mechanical properties of the binder films are possible to measure from tensile tests. Zhu *et al.* (2014) and Najafi *et al.* (2018) report the mechanical properties of mixtures of starch and latex. The maximum stress at failure is the parameter A in equation (7.1). The elastic modulus divided by A is the parameter B in equation (7.1) because the initial slope of this equation is the product of A and B. Table 7.1 shows the mechanical properties of these films produced from mixtures of latex and starch. As is well known, as starch is added to these systems, the elastic modulus of the binder increases but the strain at failure decreases.

**Table 7.1 Mechanical properties of particle free films composed of mixtures of starch and latex.**

Investigator	Weight Fraction Latex (Parts)	A (MPa)	B	E (MPa)	STF (%)
Najafi <i>et al.</i>	100	1.5	2	3	200
Najafi <i>et al.</i>	80	4.9	15	73.5	80
Najafi <i>et al.</i>	60	4.8	35	168	22
Najafi <i>et al.</i>	40	11.0	60	660	5
Zhu <i>et al.</i>	100	3.75	3.2	12	355
Zhu <i>et al.</i>	77	9.4	24	221	200
Zhu <i>et al.</i>	58	15.5	29	448	41
Zhu <i>et al.</i>	38	32.0	36	1156	13

If particles move closer to each other compared to the initial gap (compression), a repulsive force is applied to keep the particles from overlapping. This repulsive force is linear and depends on the

compressive strain as  $F = C\epsilon$ , where  $C$  is some constant and the strain is the current gap between particles divided by the initial gap. The value of  $C$  must be large enough to prevent overlapping but not to impact the final results.

Another parameter included in the model is the distance between two particles within which they can still be considered neighbors and, thus, considered to have a connection. Some have termed this concept “nearest neighbors”. At the Critical Pigment Volume Concentration (CPVC), every particle should be close to several others. However, it is not clear at what distance particles should be considered connected. In Figure 7.2, if the gap between the particle of interest and the other particles, is less than one radius, the particles will be considered neighbors and, therefore, be connected. If they are too far away, then no connection is assumed.

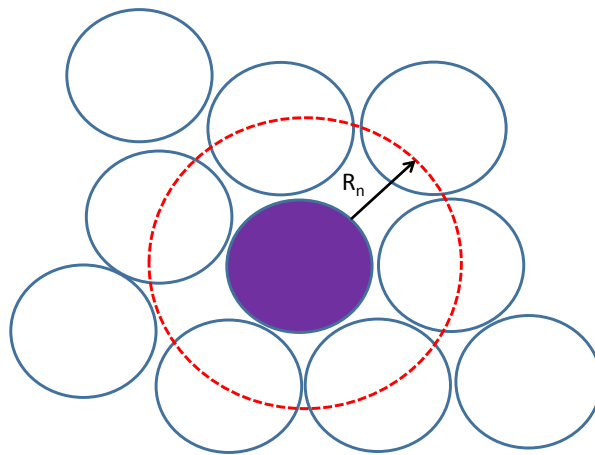


**Figure 7.2 Near neighbor criteria with  $R_n=1.0$ . Particles closer than the criteria are assumed to be connected. As  $R_n$  increases, more particles are connected together.**

## 7.4 Particle Size Distributions

The main difference between this current paper and the previous one by these authors [Varney *et al.* (2019)] was the move beyond a monodisperse packing of spherical particles to two other distributions of the same particle shape. The first one involved bimodal distributions of large and small spheres. The amounts, or levels, of each size were based on the work of Brouwers (2011). This paper showed that the void fraction of bimodal mixtures was a function of the size ratio  $u$  ( $u = d_L/d_S$ , where  $d_L$  is the diameter of the large particles and  $d_S$  is the diameter of the small particles) and of the volume fraction of the large particles  $c_L$  (see Figure 7.3). To cover a range of void fractions, three size ratios (5:1, 3.33:1, and 2.5:1) were used for each of three volume fractions of the large particles (0.80, 0.65, and 0.50).

In addition to these nine bimodal distributions, two full distributions that represented a coarse GCC (60 w/w% < 2 microns) and a narrow particle size GCC (93 w/w% < 2 microns) were also evaluated [they were the GCC types used by Zhu *et al.* (2014) and by Mohammad *et al.* (2017 and 2018 respectively)]. To generate data for the packing routine, particle size distribution data for these two commercially available GCCs from Omya, Inc. was obtained and discretized.

The packing routine of Toivakka *et al.* (2019) was used to generate the (x, y, z) coordinates for the nine bimodal cases, the two GCCs, and the monodisperse case. As with all prior simulations, these coordinate points were inputs to the model along with the mechanical properties of the pure binder films.

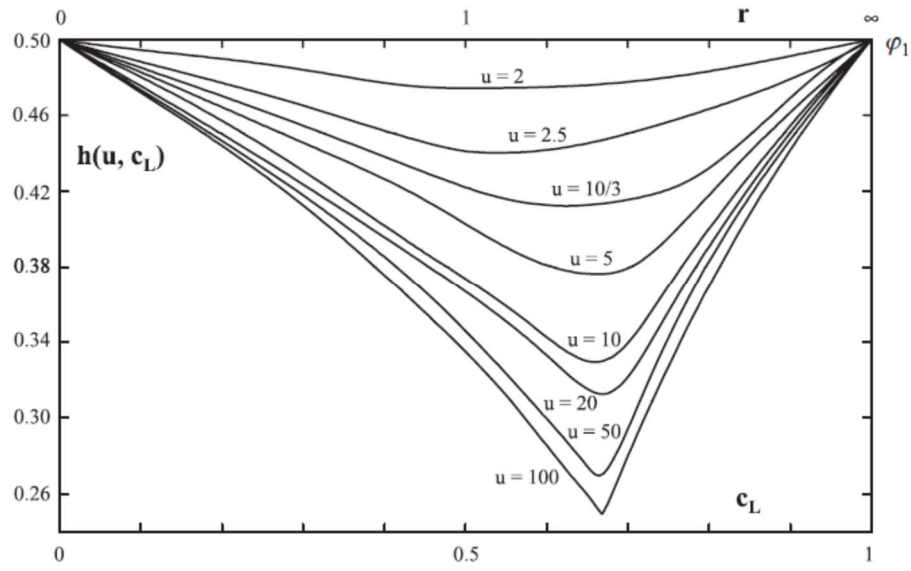


**Figure 7.3 Void fraction of bimodal mixes as a function of size ratio and of volume fraction of large constituent [from Brouwers (2011)].**

### 7.5 3D Packings

The 3D packings initially were generated with a voxel-based digital packing tool detailed in Byholm *et al.* (2009). Subsequently, the porosity of the packings was adjusted to a desired level by using a particle packing approach mimicking Brownian motion. In this case, an energy function calculated from the particle positions and particle overlaps was minimized towards the desired porosity utilizing a simulated annealing algorithm [Corana *et al.* (1987)].

Pictures of the nine bimodal distributions and of the two full distributions (representing the two GCCs) are shown in the 11 figures below. The bimodal figures clearly show the changing ratios of the small to large particles and the changing sizes of the small particles as well (the large particles always had a diameter of 1.0 in dimensionless units).

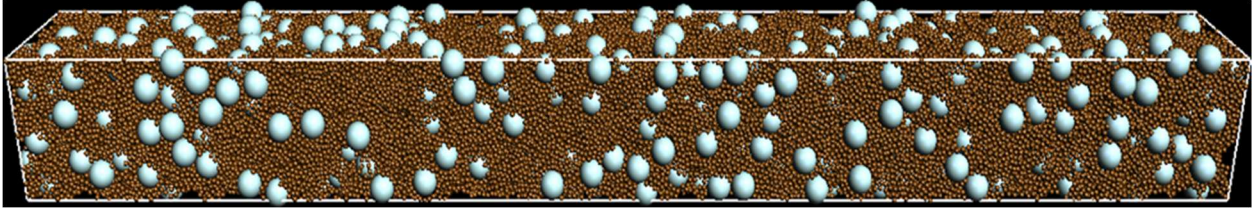


**Figure 7.4** Representation of bimodal distribution of spherical particles with 50% large particles and small particle radius of 0.2 (large diameter is always 1.0).

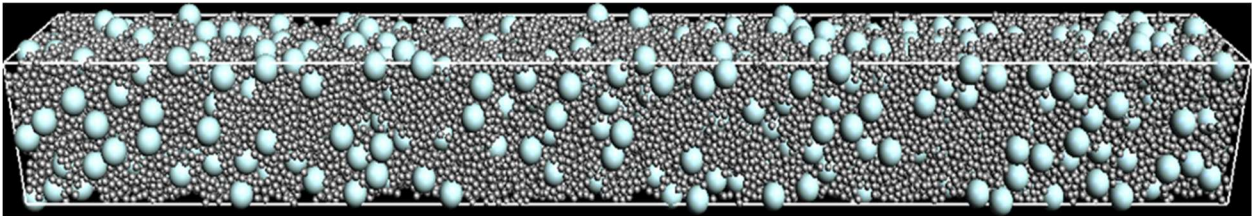


**Figure 7.5** Representation of bimodal distribution of spherical particles with 50% large particles and small particle radius of 0.3 (large diameter is always 1.0).

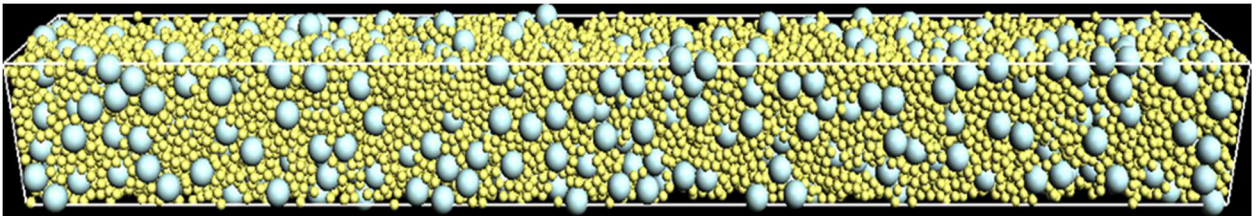


**Figure 7.6** Representation of bimodal distribution of spherical particles with 50% large particles and small particle radius of 0.4 (large diameter is always 1.0).

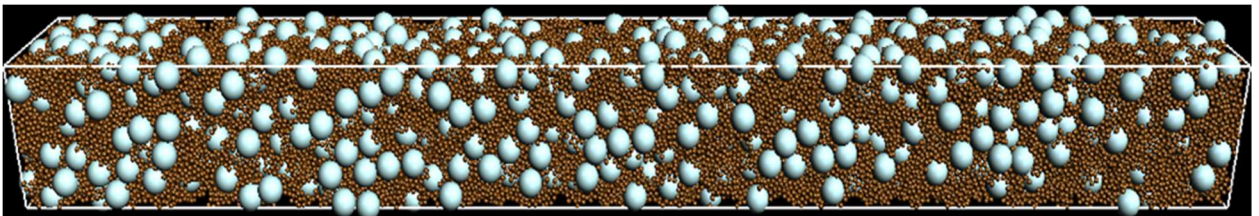


**Figure 7.7** Representation of bimodal distribution of spherical particles with 65% large particles and small particle radius of 0.2 (large diameter is always 1.0).

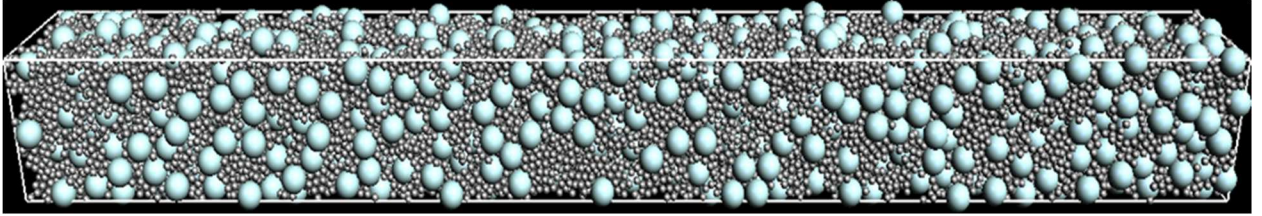


**Figure 7.8** Representation of bimodal distribution of spherical particles with 65% large particles and small particle radius of 0.3 (large diameter is always 1.0).

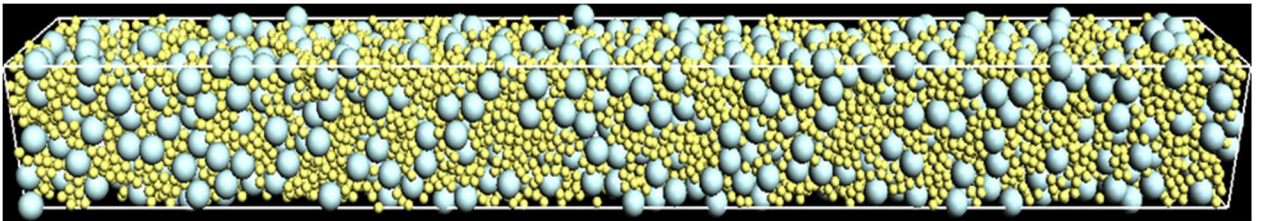


**Figure 7.9** Representation of bimodal distribution of spherical particles with 65% large particles and small particle radius of 0.4 (large diameter is always 1.0).

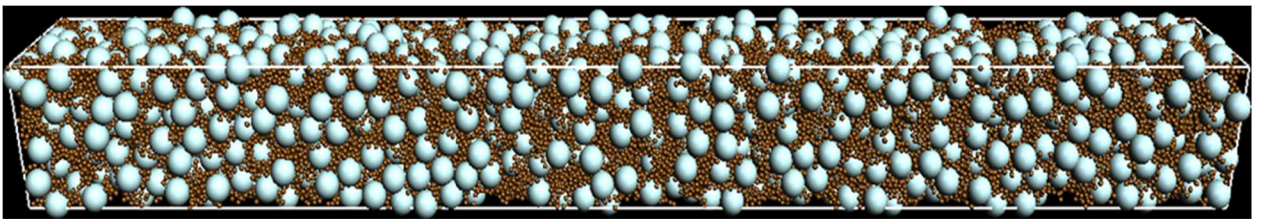


**Figure 7.10** Representation of bimodal distribution of spherical particles with 80% large particles and small particle radius of 0.2 (large diameter is always 1.0).

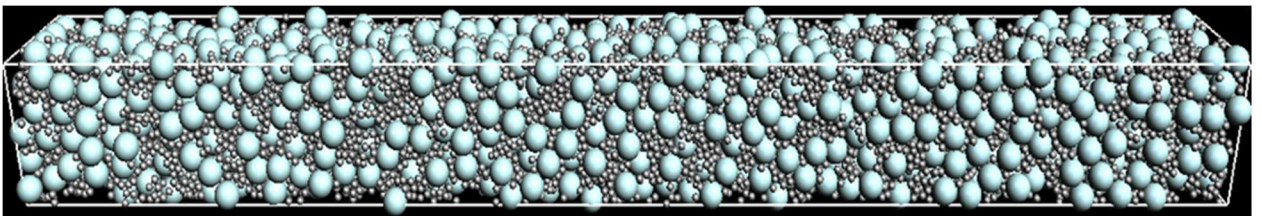


**Figure 7.11** Representation of bimodal distribution of spherical particles with 80% large particles and small particle radius of 0.3 (large diameter is always 1.0).

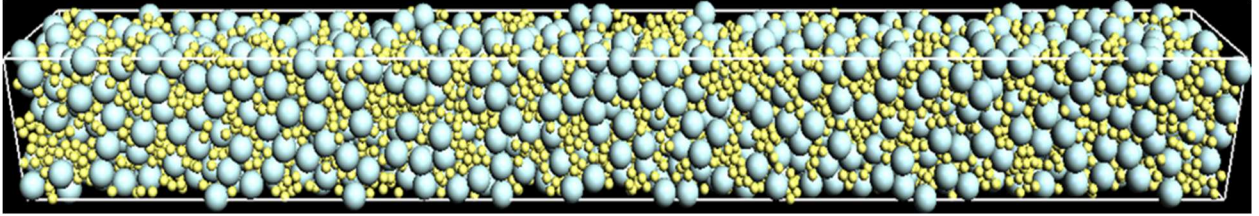


**Figure 7.12 Representation of bimodal distribution of spherical particles with 80% large particles and small particle radius of 0.4 (large diameter is always 1.0).**

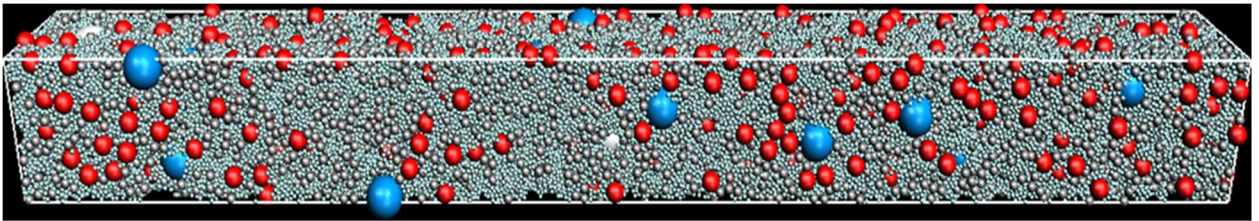


**Figure 7.13 Representation of full distribution of spherical particles approximating a narrow particle size GCC (93 w/w% < 2.0 microns).**

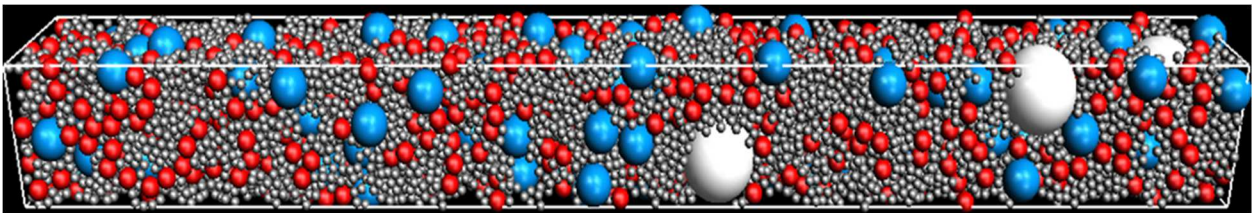


**Figure 7.14 Representation of full distribution of spherical particles approximating a broad particle size GCC (60 w/w% < 2.0 microns).**

## **7.6 Modelling of In-line Tension and of Three-Point Bending**

To simulate an in-line tensile event, particles in the grip region on the right of Figure 7.15 are set to a velocity of one dimensionless unit value to the right. Particles in the left grip region are assigned to no velocity (the pull up zone does not exist with in-line tension). This scenario causes the particles on the right to pull on other particles in the middle of the structure and transmit forces throughout the structure. The results presented here are for slow motions relative to the inertia of

the particles. Therefore, the forces are near equilibrium during the deformation event and the rate of deformation is not important.

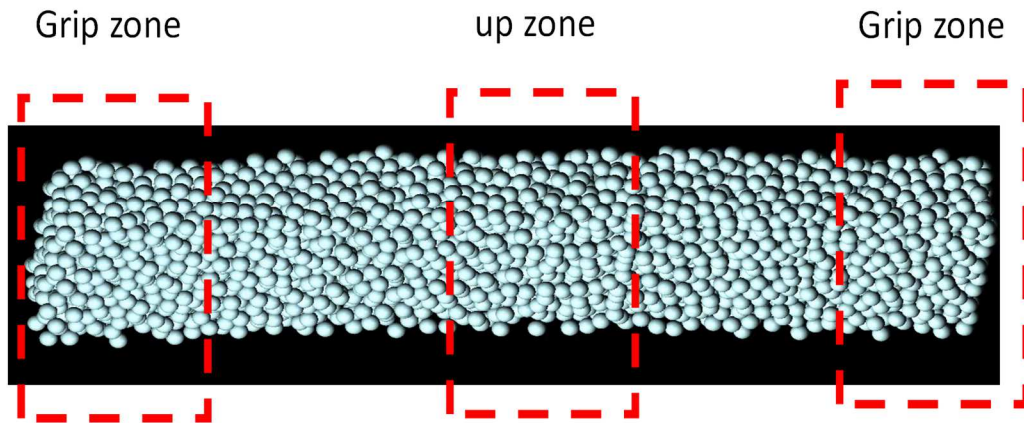


**Figure 7.15 3D situation for uniform spheres packed in a 10x10x100 cell. Particles are packed to a PVC of 64%.**

To stabilize the simulation when a crack develops, it was found helpful to add a small damping factor, where a particle moving at some velocity will experience a force in the opposite direction. The equation is  $F = -DV$ , where  $D$  is a damp factor and  $V$  is the velocity vector. The value of the damping factor should be as small as to not influence the predictions of the modulus or of the ultimate stress.

To simulate bending tests, particles in the “push up” zone are assigned an upward velocity (the particles are pushed upwards from below this zone). The sizes of the two holding (grip) zones and of the push up zone have minimal influence on the results as long as the distance from the zones is large compared to the zones themselves. Spheres on the two sides (the grip zones) of the simulation are not allowed to move in the vertical direction, but they are allowed to slide in the horizontal direction or deflect downward.

In both cases (in-line tension and three-point bending), as some particles are forced to move from their equilibrium position, a vector force on neighboring particles is calculated using either equation (1) or the compression equation ( $F = C\varepsilon$ ). The net force on every particle is calculated based on its position and the position of all of the neighbors. This net force is used to update particle velocities and positions with a numerical integration using a predictor-corrector method. In the results presented in this paper, the motion is slow and the inertia terms are small; time or rates do not influence the results, but these effects are straight forward to include in the future. These time integrations can be expressed as

$$\begin{aligned} a &= dV / dt = F / x_m \\ dP / dt &= V \end{aligned} \quad (7.3)$$

where  $a$  is acceleration,  $V$  is velocity,  $F$  is force,  $x_m$  is a parameter that represents the mass of the particle, and  $P$  is position. Equation (7.3) is a vector equation because it has components in each dimension.

The sum of the forces on the particles that move relate to the force a mechanical tester would record; these forces balance the sum of the forces on the particles that are not allowed to move. In tension, the stress is the sum of the forces on the grip particles divided by the cross sectional area. The flexural stress and strain can be calculated as

$$\sigma_f = \frac{3PL}{2bd^2} \quad (7.4)$$

$$\varepsilon_f = \frac{6Dd}{L^2} \quad (7.5)$$

where  $P$  is the sum of the forces on the grip particles (or the load force),  $L$  is the distance between grips,  $D$  is the displacement of the upward moving particles at the center of the sample,  $b$  is the width of the sample and  $d$  is the thickness of the sample. The goal is to predict the bending behavior and the crack propagation of these systems.

The deformation and local forces in the 3D case are shown in Figure 7.16 for a typical three point bending case. In the region that is forced upward, a tensile force is generated. Also, near the two grip regions where particles are only allowed to slip in the horizontal direction, a tensile force is generated between particles.

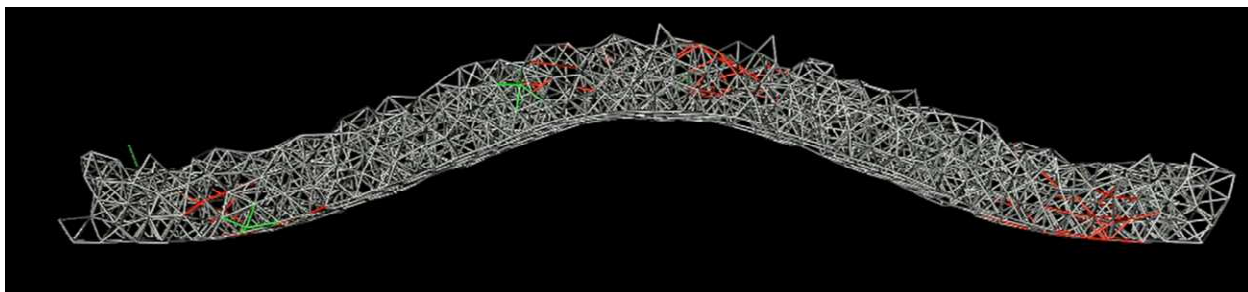


**Figure 7.16 Bending deformation in 3D mode, showing the connections between particles for a typical case for monodisperse spheres.**

### **7.7 Results – In-line Tension**

The predictions of the models are compared to the in-line tensile experimental data of Zhu *et al.* (2014) in Figures 7.17 – 7.19 for the PVC near the critical value of 63% by volume of pigment and for the 77% latex/23% starch binder package (77L/23S). The model was run using the nine different bimodal distributions, the uniform spheres, and the pseudo-Hydrocarb 60 (H60) distribution (this GCC was the pigment used in Zhu's experiments). The values for the input

parameters A and B were taken from the 77L/23S pure binder data. Other important model parameters were values of  $R_n = 1.0$  and  $R_b = 1.0$ .

The plot of elastic modulus is shown in Figure 7.17. The modulus is plotted vs. the volume fraction of larger particles with three lines representing the small particle radii (0.2, 0.3, and 0.4). In addition, datapoints for the Zhu data and for the pseudo-H60 are shown as horizontal lines across the range of X-values. Lastly, the mono-disperse case is shown as a single data point at the 100% large particle point on the X-axis. The three bimodal lines are assumed to converge on this monodisperse point.

The graph shows the pseudo-H60 datapoint to be only 6% higher than the value from Zhu's experiments of 4.7 GPa. The bimodal distribution with a small particle radius ( $R_s$ ) of 0.4 comes the closest to matching this value, but it still exceeds the Zhu data like the rest of the bimodal simulations. One trend to note is the increase in modulus as the radius of the small particle decreases, which occurs for each volume fraction of large particles (save for one case). The reason for this trend is that the number of particles and, hence, the "tightness" or density of the packing increases as the small particle radii decrease. With more particles filling the voids between the larger ones, fewer and smaller voids are resulting, which leads to more connections. As a consequence, the strength will increase with a denser packing. In addition, the general trend in modulus values as the percent volume of larger particles increases is downward, which results from the same argument that there are fewer smaller particles and the bimodal distribution is trending towards being more of a monodisperse matrix. Interestingly enough, the pseudo-H60 data

point is lower than the rest, which might imply a fairly open packing that probably is due to a large average particle size (about 1.4 microns).

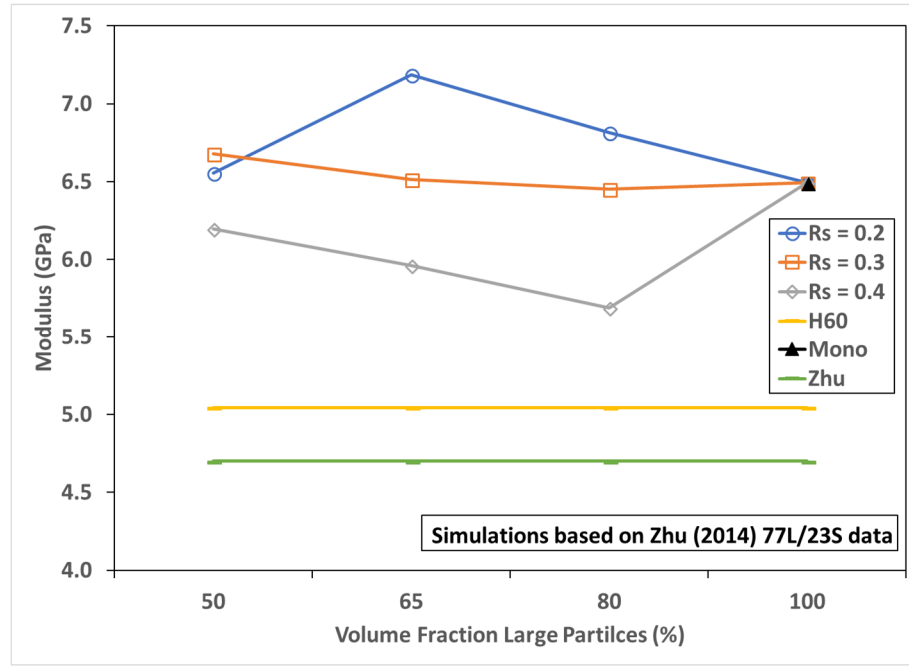


**Figure 7.17 Elastic modulus of coating layer for in-line tension at PVC = 63% and with the 77L/23S binder system. H60 closest to Zhu – off by only 6.4%.**

In contrast to the modulus, the maximum stress plot below (Figure 7.18) shows the model results to be significantly below the Zhu value of about 27.0 MPa. The monodisperse and pseudo-H60 data points are below all three bimodal lines, which also all appear to trend upwards (in contrast to the modulus bimodal lines). In addition, the data from Zhu and for the pseudo-H60 case are quite different. The reasons for the poor performance of the model to approximate the Zhu experimental data for this property are not clear at this time.

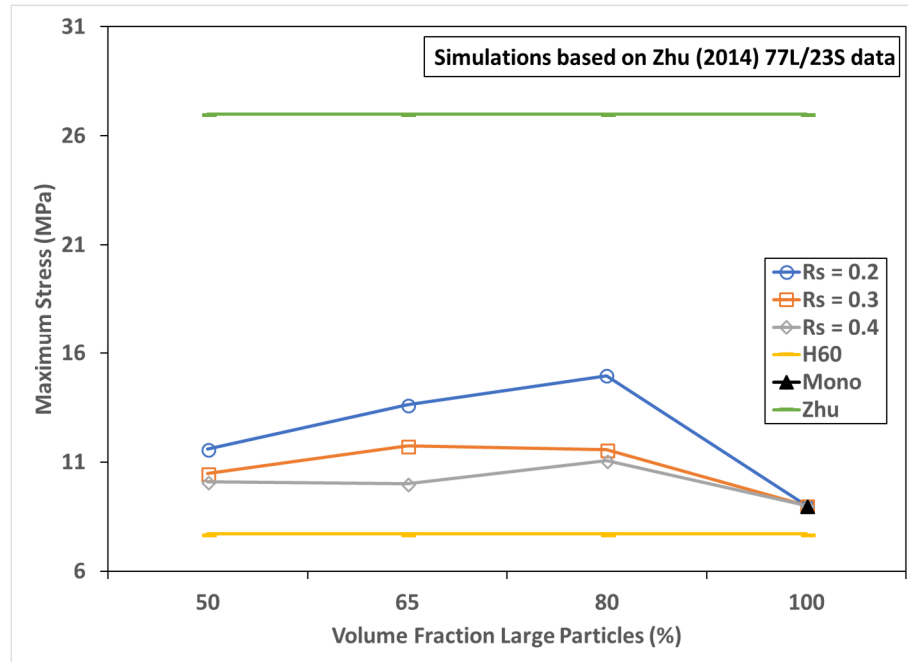


**Figure 7.18 Maximum stress of coating layer for in-line tension at PVC = 63% and with the 77L/23S binder system. H60 worse of all (by 71%) and  $R_s = 0.2$  low by 50%.**

The strain-at-failure simulation results shown in Figure 7.19 indicate the model to underpredict the Zhu data, albeit not to the extent as with the maximum stress. The same trends followed in both cases, with the pseudo-H60 being the lowest for the STF results as well.

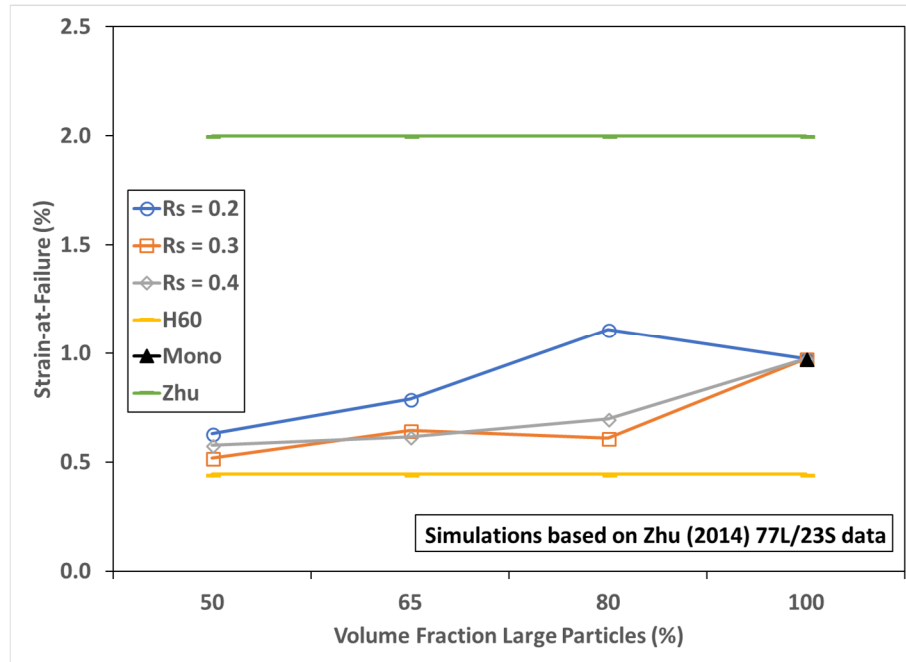


**Figure 7.19 Strain-at-failure of coating layer for in-line tension at PVC of 63% and with the 77L/23S binder system. H60 worst of all (by 80%) and  $R_s = 0.2$  low by 58%.**

Figures 7.20 – 7.22 show the comparison of Zhu’s in-line tension data with the model at two PVCs (and, four different latex/starch ratios in each case). While the experimental work was done at several pigment volume concentrations, the values of 63 (which is the critical PVC) and 78 were chosen for this exercise. The modulus plot in Figure 7.20 shows the model to approximate the experimental data quite well, especially at higher latex levels in the binder system. At the lowest level of latex (38%), the model overpredicts the modulus. In addition, the values at a PVC of 78 are lower than the corresponding values at a PVC of 62. This results makes sense as there is less binder in the matrix (relative to the amount of pigment) above the CPVC, which should lead to a drop in strength. And, as has been seen in the past, the modulus decreased as the level of latex in the binder system increased (i.e., the amount of starch was reduced).

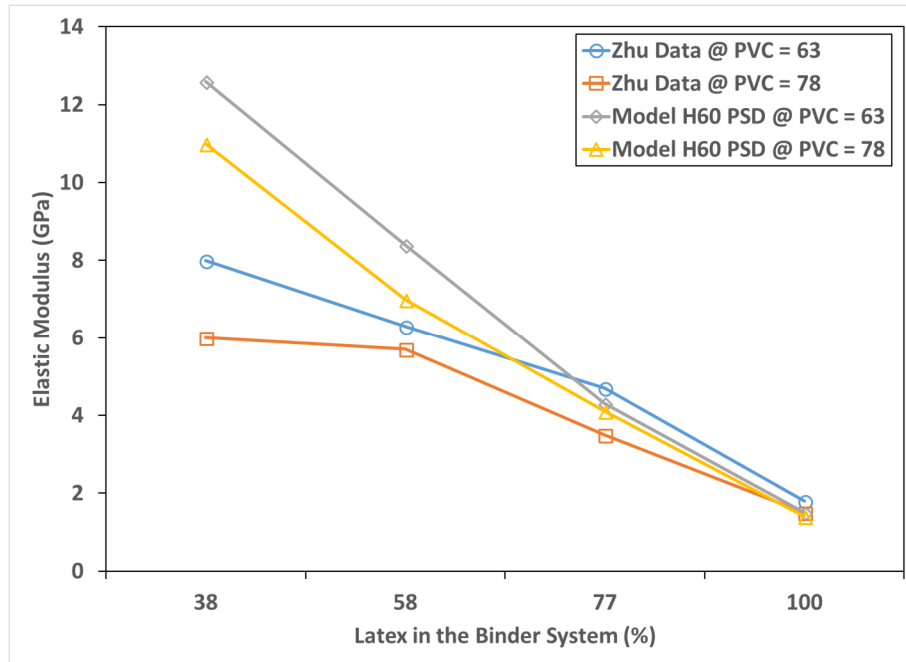


**Figure 7.20 Elastic modulus comparison between Zhu and the model at two PVCs (in-line tension).**

The maximum stress plot in Figure 7.21 shows some of the same general trends save for the model underpredicting the work of Zhu instead. The higher 78 PVC results for both the model and the experimental work were lower than the 62 PVC conditions and the overall curves decreased directly with the starch level.

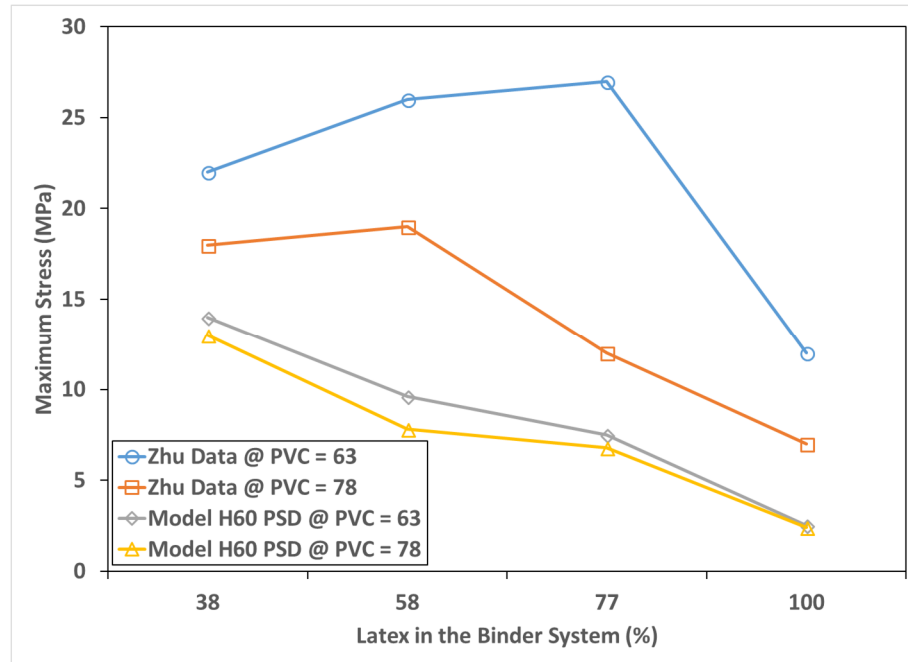


**Figure 7.21 Maximum stress comparison between Zhu and model at two PVCs (in-line tension).**

The strain-at-failure plot in Figure 7.22 shows the same trends as have been seen before. The model and the experimental data are in good agreement at low levels of latex in the binder package but start to diverge as the latex percentage increases (especially when the binder is 100% latex). The model underpredicts the Zhu data as well.

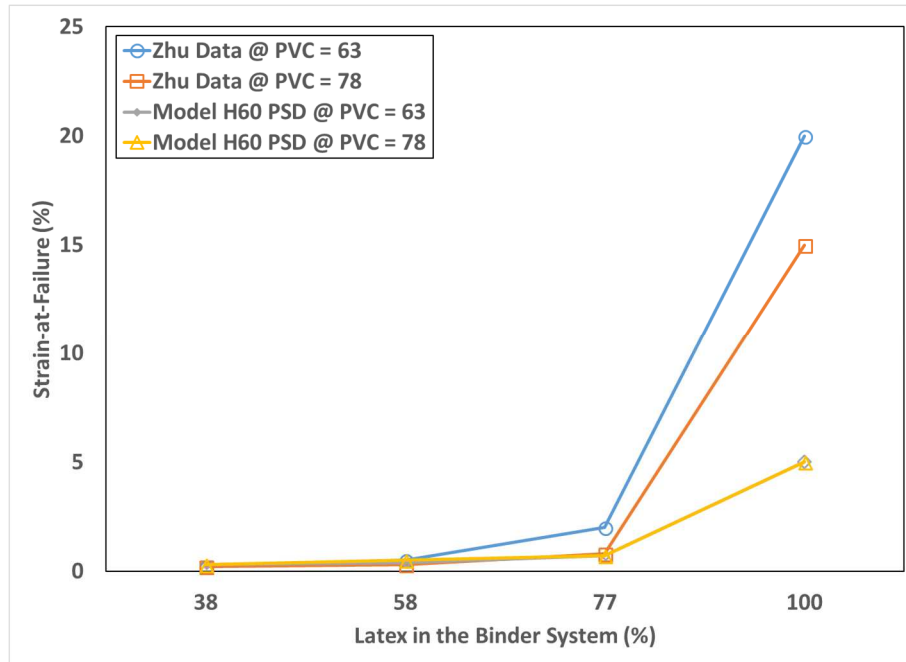


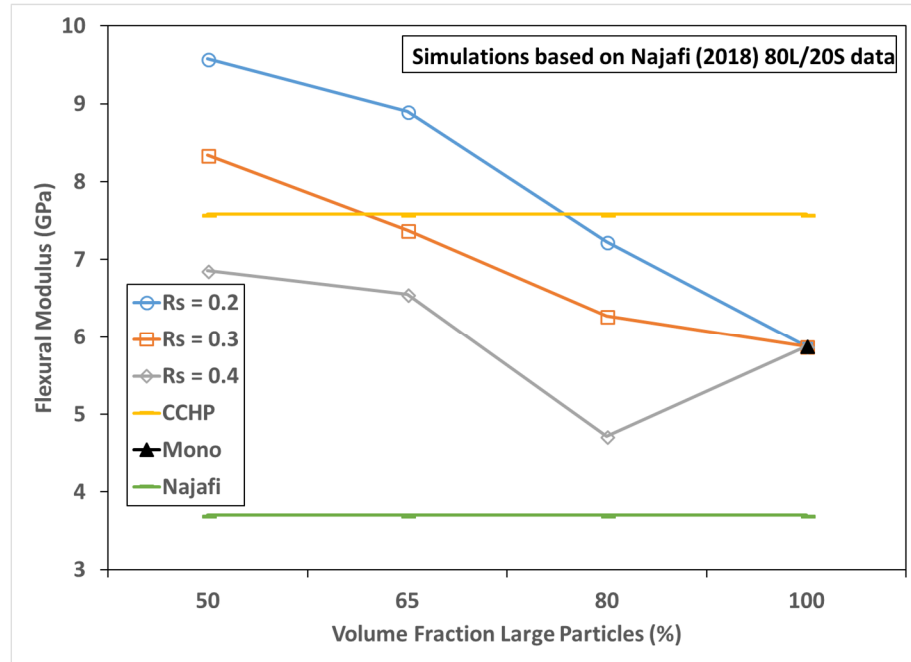
**Figure 7.22 Strain-at-failure comparison between Zhu and model at two PVCs (in-line tension).**

### 7.8 Results – Three-Point Bending

The predictions of the model are compared to the three-point experimental data of Najafi *et al.* (2018) in Figures 7.23 – 7.25 for the PVC near the critical value or around 63% by volume of pigment and for the 80% latex/20% starch binder package (80L/20S). The same particle size distributions were run in this comparison as was done with Zhu but the pseudo-H60 was replaced with a distribution which approximated Covercarb HP (which was the GCC used by Najafi *et al.*). In addition, the model input parameters A and B were taken from the 80L/20S pure binder data. And, as before the values for  $R_n$  and for  $R_b$  were 1.0 in each case. In addition, these sets of figures are set up in the same manner as Figures 7.17 – 7.19 in terms of how the data is plotted.

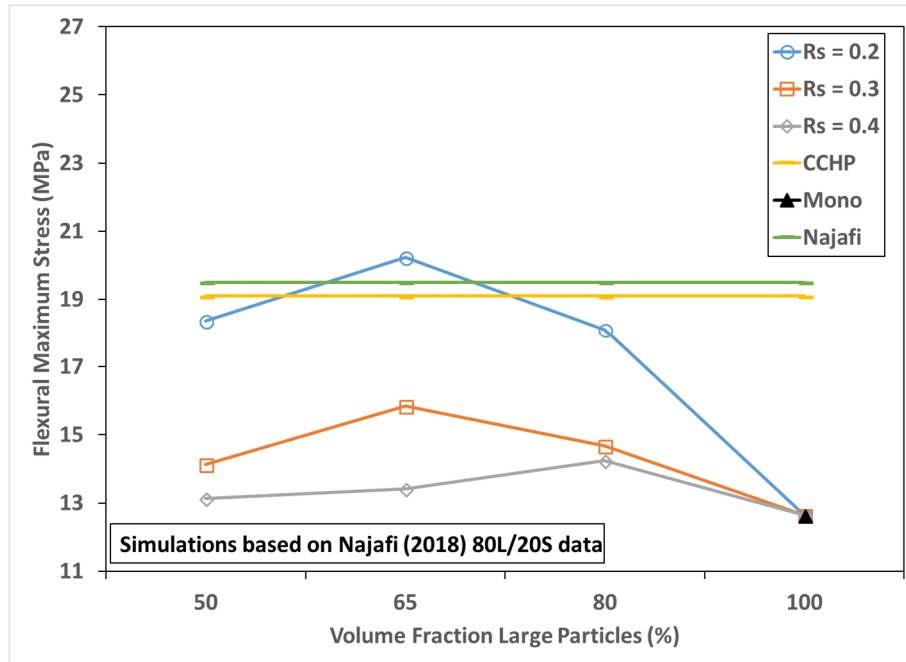
The flexural modulus shown in Figure 7.23 shows the same general trends as did the Zhu data as far as the bimodal distributions are concerned. While the simulation results all over-predict the

Najafi modulus value of 3.7 GPa, the bimodal distribution with 80% large particles by volume and a small particle radius of 0.4 comes the closest to Zhu. The pseudo-CCHP line also is significantly higher than the Zhu data by a factor of over two.



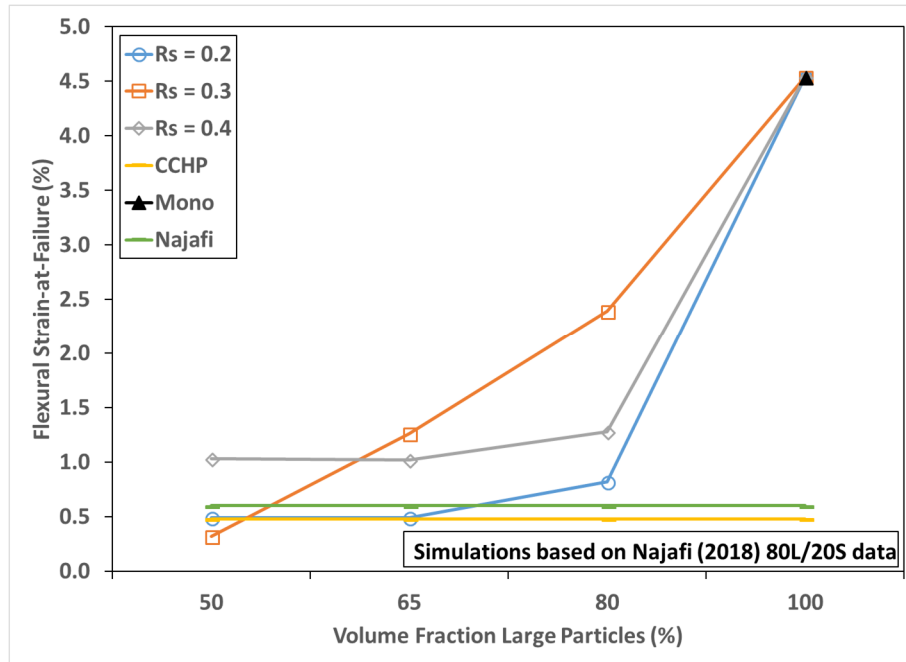
**Figure 7.23 Predicted and measured flexural modulus for the coating layer near PVC of 63% for binder components of various levels of starch and latex (three-point bending). Mono (uniform spheres) closest to Najafi (off by 41%) along with one  $R_s = 0.4$  condition.**

As for the maximum stress seen in Figure 7.24, the results of Najafi *et al.* and of the model using the pseudo-CCHP particle size distribution are fairly close. The bimodal distribution with a small particle radius of 0.2 also is a good match to these two horizontal data lines. The monodisperse data point (to which the three bimodal curves converge) is the furthest from the experimental data line of Najafi, which could be a function of the impact of packing on strength.



**Figure 7.24 Predicted and measured flexural maximum stress for the coating layer near PVC of 63% for binder components of various levels of starch and latex (three-point bending). CCHP only 2% above Najafi and  $R_s = 0.2$  only off by 3%.**

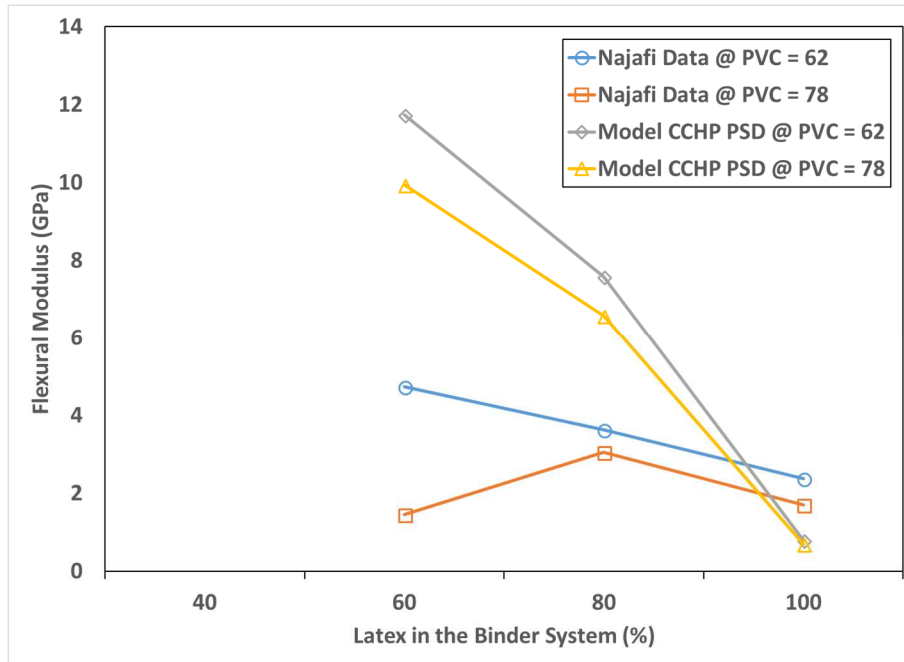
The strain-at-failure of Figure 7.25 shows good agreement between the Najafi data and the CCHP prediction. The three bimodal lines also are reasonably close to the experimental results. As with the maximum stress, the monodisperse data point is significantly different from the other results, be they from the experiments or from the model.



**Figure 7.25 Predicted and measured strain at failure for coating layers near PVC of 63% for various levels of latex and starch in the binder composition (three-point bending).  $R_s = 0.2$  spot on vs. Najafi while CCHP very close as well (0.5 vs. 0.6).**

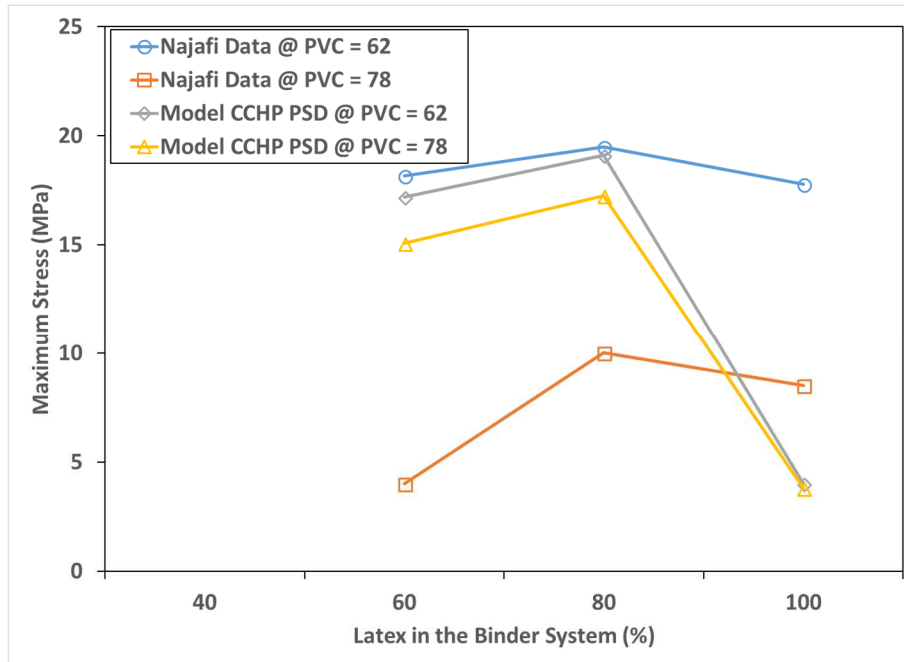
Figures 7.26 – 7.28 show the comparison of the model for the two different PVC concentrations (63 and 78) of Najafi *et al.* (2018). As with the Zhu comparisons in Figures 7.20 – 7.22, the binder bridge radius, for a PVC of 78%, is 90 percent of the particle radius based on equation (2) above. This value reduces the modulus predictions and the maximum stress predictions around that factor, but the strain to failure remains quite similar.

The flexural modulus results in Figure 7.26 overpredicts the experimental data for both PVCs. This result is in contrast to the in-line tension comparison with Zhu’s data, which was more favorable. Regardless, both sets of data show the same trends in that the higher PVC condition has a lower modulus value and the lines trend downwards with increasing latex percentage in the binder system.



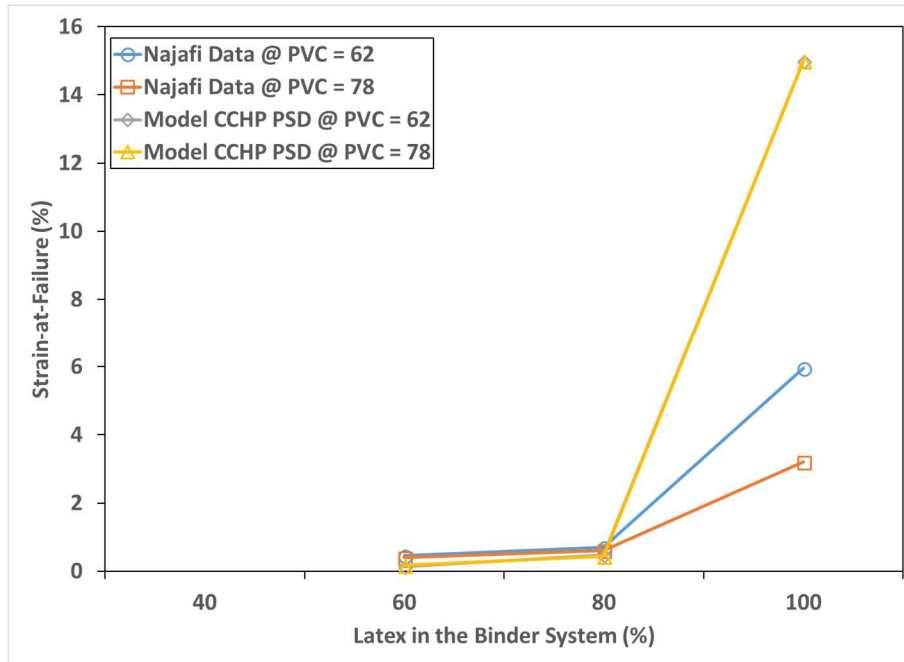
**Figure 7.26 Flexural modulus predictions and experimental results of Najafi at two PVCs (three-point bending).**

Figure 7.27 shows the maximum stress and the reasonably close agreement between the model and the Najafi data at 62 PVC. For some reason, the 78 PVC experimental data is significantly different from the other lines.



**Figure 7.27 Maximum stress predictions for two different PVC values and the predictions (three-point bending).**

The strain-at-failure in Figure 7.28 indicates very good agreement between the Najafi data and the model results. This same scenario was seen in Figure 22 for the in-line tension PVC comparison.



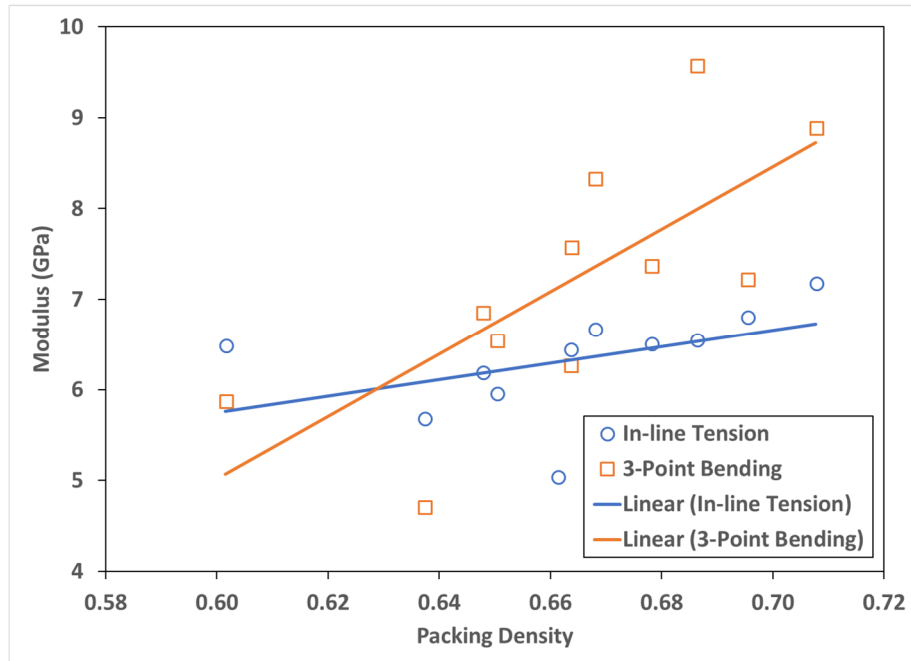
**Figure 7.28** The strain at failure predictions and data for two PVC values (three-point bending).

A number of assumptions are used in these simulations to simplify the model. This list includes perfect adhesion between the binder and the pigment, the initial packing of the particles being similar to that of the real case, and the starch and latex forming a uniform material (Chen *et al.* in 2014 discuss this topic in detail). In addition, the distributions modelled in this paper only approximate the particle size distributions of the actual pigments used in the experiments.

### 7.9 Impact of Packing Density on Mechanical Properties

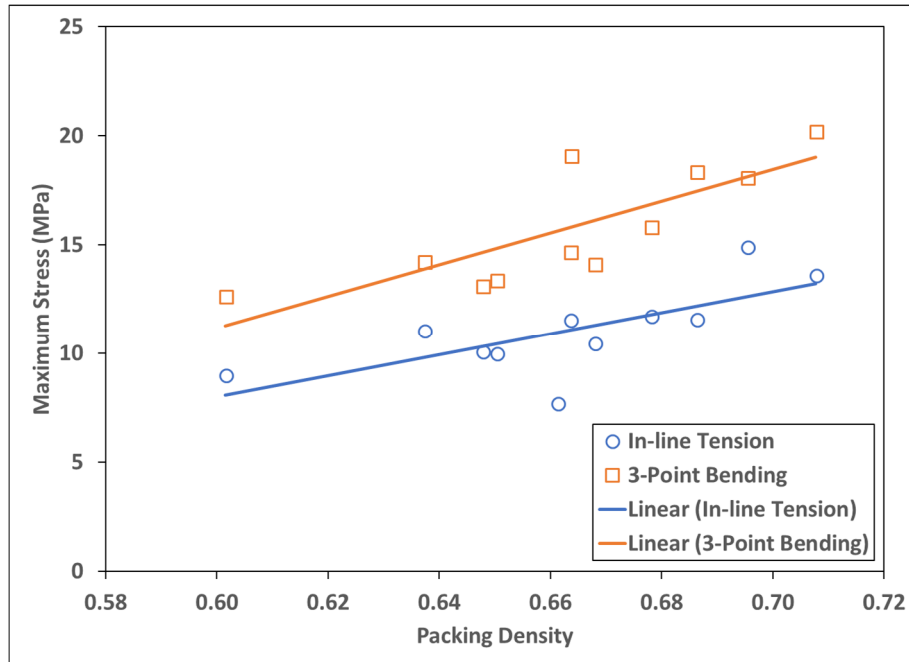
The manner in which the particles were packed in to the three-dimensional matrix was described earlier in brief fashion. This technique produced packing densities ranging from about 0.60 to almost 0.71, with a resulting minimum gap between particles of about 0.005. The impact of the tightness of this initial packing on the final mechanical properties of the simulation are shown in Figures 7.29 – 7.31.

Figure 7.29 shows the modulus for both in-line tension and for three-point bending. The data for both cases shows a slight upward trend in modulus as the packing density increases. As the particles are packed more tightly, the minimum gap decreases, which causes the initial strain to increase, resulting in an increase in the modulus.



**Figure 7.29 Modulus vs. packing density (in-line tension and three-point bending).**

The maximum stress seen in Figure 7.30 follows the same trend. The two curves show an increase in values as the packing density increases (i.e., as the minimum gap between the particles decreases). The same reasoning for the trend with the modulus explains this trend as well.



**Figure 7.30 Maximum stress vs. packing density (in-line tension and three-point bending).**

Figure 7.31 illustrates the impact on strain-at-failure is a bit varied as the packing density increases. The STF for the in-line tension is fairly flat in the plot, but the scale skews the appearance of the trend line, as it actually increases directly with packing density. The STF for the three-point bending shows the data to follow a downward trend, which is contrary to expectations. The reasons for this result are not clear at this time.

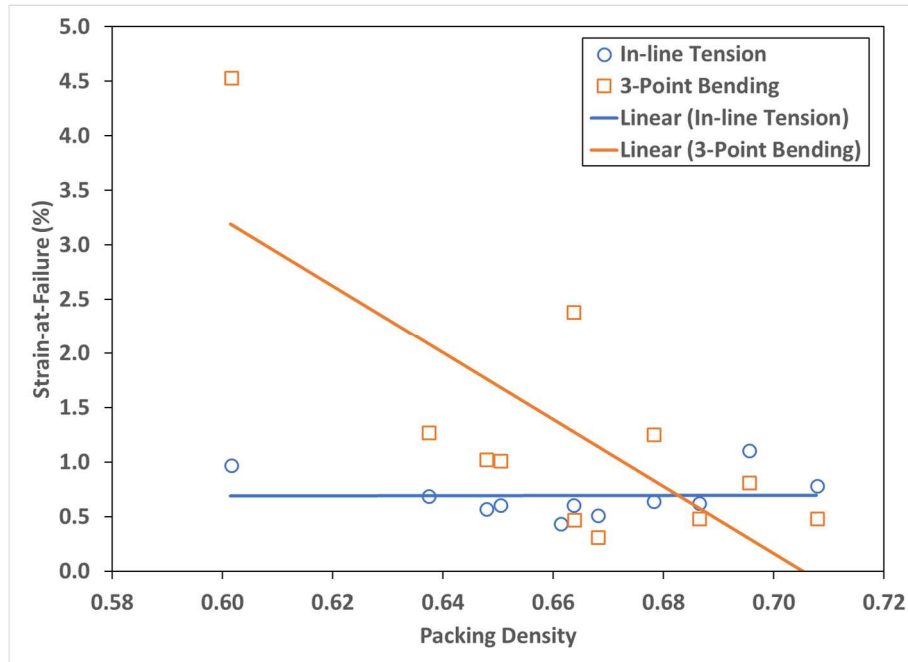


**Figure 7.31 Strain-at-failure vs. packing density (in-line tension and three-point bending).**

## 7.10 Conclusions

A discrete element method model is developed to predict the mechanical properties of pigmented coating layers. The model parameters are the mechanical properties of the binder and the pigment volume concentration. The model gives reasonable predictions in both tensile and flexural tests and does predict all of the correct trends. Expanding the model from its traditional use of uniform spherical particles to bimodal and full particle size distributions of the same particle shape improves the predictions. For both in-line tension and for bending; the model overpredicts the modulus and underpredicts the maximum stress (in-line tension in particular). The results are not consistent between the two deformations types with regard to strain-at-failure. Lastly, the comparisons between the model and the two sets of experimental data show better agreement for three-point bending than for in-line tension.

One possible explanation for the discrepancies between the model and the experimental data is the packing routines used to “assemble” the pigment matrix. They only involve packing of the pigments and do not take the binder in to account in terms of its impact on the packing density and the initial minimum gap. As a consequence, while the binder is assumed to be between and around each particle (at or below the CPVC), the real world situation might be quite different. Some particles might not have much if any binder between or around them (especially at PVCs above the critical value), which can impact the coating strength and the cracking propensity. Thus, somehow incorporating the binder in to the initial packing could improve the predictions even further.

## CHAPTER EIGHT

### SUMMARY AND FUTURE WORK

#### 8.1 Summary

The goal of this thesis was to use the discrete element method (DEM) to model paper coating deformation events to improve the fundamental understanding of the responses resulting from these events. The DEM had been used to simulate tension and compression but it had never modelled bending before. The thesis was able to show that this method could model all three of these events and provide results comparable to experimental data. As for the type of tension, the model could handle in-line as well as out-of-plane modes, which was novel as well. Other firsts with this model was its ability to simulate binder systems comprised of latex and starch in addition to latex-only binders. Plus, the model simulated three-point bending for a two-layer coating, which had not been done in any prior work.

All of the modeling was done using particles represented by spheres. Much of the early work was done in two-dimensions with a uniform distribution of spherical particles. As the model evolved, three dimensional arrays of spheres were modelled. Finally, the particle size distribution being modelled was expanded to both bimodal and two full distributions. In all of these cases, the various deformation modes were simulated and compared to experimental data.

An important point to remember when considering the success of the model in approximating the experimental data is the standard deviation of the lab data itself. While Zhu *et al.* (2014) does not provide this information for the pigmented films, the standard deviations of the pure binder films

ranged from a low of about 3% to over 33% of the absolute values of the three main mechanical properties across the eight binder systems evaluated in his thesis. As for Najafi *et al.* (2018), he provided the standard deviations of the pigmented films. These values fluctuated from less than 1% to over 31% for modulus, maximum stress, and STF across four binder systems. Thus, the model predictions should be even closer to the experimental results when taking the error of the lab data in to account.

The model has some features which make it unique compared to other approaches. First, mechanical properties of the pure binder films are inputs to the model (in addition to the particle positions). This approach is somewhat novel. Secondly, the model is based on a clear set of constitutive equations, which makes it simpler than other types of models.

These mechanical properties are just a few of the input parameters evaluated during the study. As an example, the parameter  $R_n$  and the move to a full particle size distribution were assessed but provided inconsistent results. While a slightly different range of values could be considered for the many input parameters, the results probably would be the same in terms of the predictive ability of the model. As a consequence, the list of input variables for adjustment most likely has been exhausted.

While the model was not perfect, it could predict the correct trends with the same order of magnitude as the experimental data. Modifications made to the model to improve the predictions were based on physical science and not on mathematical adjustments to help the simulation results

better match the experimental data. As such, the model might be considered conceptual in nature as its goal, as stated previously, was to improve fundamental understanding.

The model also has a great deal of versatility. While it can simulate a variety of deformation events for multilayer coatings comprised of various particle size distributions, other possibilities exist as well. It should be capable of simulating a cantilever type of bending event, calendaring as done in paper making, and slitting among other scenarios. This work could be done as part of the next iteration of improvements.

## **8.2 Future Work**

Future work to improve the model should focus on several opportunities. Optimizing it for specific binder systems (e.g., the adhesive force factor), expanding it to model deformation events not included in this thesis, and including the base paper as another layer are some ideas. Another option is to include the binder in the packing routine when the particles are packed. Since this routine only involves the particles, the binder and its impact on the packing density and on the gap between particles is not taken in to account. Currently, the model assumes that a binder bridge exists between each particle, but this situation would not be the case above the critical pigment volume concentration (CPVC). This modification could be instrumental to improving the comparison between the model and the lab data. In a way, it is similar to considering starch as a pigment, which this paper as well as past researchers have investigated. Lastly, modifying the packing routine so that the gap between the particles is not the same should be considered.

In addition, other ideas to consider include the following: the use of non-spherical particles, the consideration of a substrate as another layer, somehow including dispersant on the particle surfaces as occurs with commercial pigments, and the relaxation of the assumption that all failure takes place cohesively within the binder. The first idea would involve attaching small spheres together to form a particle which might mimic a platy clay particle for example. And the notion of considering failure not only to be cohesive but also adhesive (at the binder/particle interface) is addressed in the appendix with the use of an adhesive force fraction factor.

## REFERENCES

- Alam, P., Mathur, S., Byholm, T., Jarvinen, O., Kniivila, J., Toivakka, M., “A Theoretical Approach to Understanding Microstructure Tensile Modulus Relations in Paper Coatings”, 10<sup>th</sup> Advanced Coating Fundamentals Symposium, Montreal, Canada, 2008.
- Alam, P., Toivakka, M., Carlsson, R., Salminen, P., and Sandas, S., “Balancing Between Fold-Crack Resistance and Stiffness”, *Journal of Composite Materials*, Vol. No. 43, No. 11, pp. 1265 – 1283, 2009.
- Alam, P., “A Mixture’s Model for Porous Particle-Polymer Composites”, *Mechanics Research Communications*, Vol. 37, Issue 4, pp. 389 – 393, June 2010.
- Alam, P. and Toivakka, M., “Coupled Spreading Fraction Effects of Polymer Nano- Binder on the Network Connectivity and Tensile Modulus of Porous Mineral Coatings”, *Materials Letters*, Vol. 88, pp. 73 – 75, 2012.
- Alam, P., Toivakka, M., Lazarus, E., and Salminen, P., “On the Mechanisms of Wet and Dry Strength of Paper Coatings: Part II – Modelling and Simulation”, *PaperCon 2012*, April 22 – 25, 2012, New Orleans, Louisiana.
- Azadi, P., Farnood, R., and Yan, N., “Discrete Element Modeling of the Mechanical Response of Pigment Containing Coating Layers Under Compression”, *Computational Materials Science*, Vol. 42, pp. 50 – 56, 2008.
- Azadi, P., Farnood, R., and Yan, N., “Modeling the Effect of Pigment Morphology on the Dynamic Compression of Coating Layers Using DEM”, *Computers and Chemical Engineering*, Vol. 32, pp. 3084 – 3089, 2008.
- Barbier, C., Larsson, P-L, Ostlund, S., “Numerical Investigation of Folding of Coated Papers”, *Composite Structures*, No. 67, pp. 383 – 394, 2005.
- Barbier C., Rättö P., Hornatowska J.,” Coating Models for an Analysis of Cracking Behavior Between Folded Paper and Creased Board”, *Tappi Advanced Coating Fundamentals Symposium*, September 9 – 12, 2012, Atlanta, Georgia.
- Brouwers, H. J. H., “Packing Fraction of Geometric Random Packings of Discretely Sized Particles”, *Physical Review*, Edition 84, No. 042301, 2011.
- Byholm, T., Toivakka, M., and Westerholm, J., “Effective Packing of 3-Dimensional Voxel-Based Arbitrarily Shaped Particles”, *Power Technology*, Vol. 196, No. 2, pp. 139 – 146, 2009.
- Chen, G., Zhu, Z., Salminen, P. and Toivakka, M., ”Structure and Mechanical Properties of Starch/Styrene-Butadiene Latex Composites”, *Advanced Materials Research*, vol 936, pp 74 – 81, 2014.

Corana, A., Marchesi, M., Martini, C., and Ridella, S., “Minimizing Multimodal Functions of Continuous Variables with the ‘Simulated Annealing’ Algorithm”, *ACM Transactions on Mathematical Software*, Vol. 13, No. 3, pp. 262 – 280, 1987.

Dahlvik, P., Bluvol, G., Kagerer, K-H., Arnold, M., and Varney, D., “Factors Influencing the Surface Strength of Coated Papers”, *PaperCon 2011 Proceeding*, pp. 374 – 392, May 1 – 4, 2011, Covington, Kentucky.

Fern, N., Alam, P., Touaiti, F., and Toivakka, M., “Fatigue Life Predictions of Porous Composite Paper Coatings”, *International Journal of Fatigue*, No. 38, pp. 181 – 187, 2012.

Gates, H. and Bousfield, D., “Pressure Pulse Measurements for Coating and Printing”, *PaperCon 2015*, April 19 – 22, 2015, Atlanta, Georgia.

Hashemi-Najafi S.M., M. Tajvidi, and D.W. Bousfield, “Mechanical properties of free standing coating layers: bending and tensile properties”, *TAPPI Advanced Coating Symposium*, October 4 – 6, 2016, Stockholm, Sweden.

Hashemi-Najafi S.M., M. Tajvidi, and D.W. Bousfield, “Measurement of Tensile and Bending Properties of Free Standing Coating Layers”, *PaperCon 2017*, April 23 – 26, 2017, Minneapolis, Minnesota.

Hashemi-Najafi S.M., M. Tajvidi, and D.W. Bousfield, “Cracking at the Fold, In Coatings with Latex and Starch as a Binder”, *PaperCon 2018*, April 15 – 18, 2018, Charlotte, North Carolina.

Hashemi-Najafi, S.M.H., Tajvidi, M. and Bousfield, D.W., “Production and Mechanical Characterization of Free-Standing Pigmented Paper Coating Layers with Latex and Starch as Binder”, *Progress in Organic Coatings*, Vol. 123, pp.138-145, 2018.

Husband, J., Preston, J., Gate, L., Storer, A., and Creaton, P., “The Influence of Pigment Particle Shape on the In-plane Tensile Strength Properties of Kaolin-Based Coating Layers”, *TAPPI Journal*, Vol. No. 5, No. 12, December 2006.

Husband, J., Preston, J., Gate, L., Blair, D., and Creaton, P., “Factors Affecting the Printing Strength of Kaolin-Based Paper Coatings”, *TAPPI Coating and Graphic Arts Conference*, May 2007, Miami, Florida.

Husband, J., Preston, J., Gate, L., Storer, A., and Creaton, P., “A Study of In-Plane and Z-Direction Strength of Coating Layers with Varying Latex Content”, *TAPPI Journal*, pp. 10 – 16, December 2007.

Husband, J., Gate, L., Preston, J., Norouzi, N., and Blair, D., “Mechanistic Insights in to the Weakening Effect of Water and Oils on Latex-Bound Coatings During Printing”, *TAPPI Advanced Coating Fundamentals Symposium Proceedings*, pp. 218 – 227, June 11 – 13, 2008, Montreal, Canada.

Husband, J., Gate, L., Norouzi, N., and Blair, D., “The Influence of Kaolin Shape Factor on the Stiffness of Coated Papers”, TAPPI Journal, pp. 12 – 17, June 2009.

Husband, J., Gate, L., Norouzi, N., and Blair, D., “Using Thin-Crystal Engineered Kaolins to Enhance Mechanical Properties of Coatings”, TAPPI 2010 International Conference on Nanotechnology for the Forest Products Industry, September 27 – 29, 2010, Espoo, Finland.

Lazarus, E., Salminen, P., Alam, P., and Toivakka, M., “On the Mechanisms of Wet and Dry Strength of Paper Coatings: Part I – Experimental Studies”, PaperCon 2012, April 22 – 25, 2012, New Orleans, Louisiana.

Lee, Do-Ik, “The Critical Pigment Volume Concentration Concept for Paper Coatings: I. Model Coating Systems Using Plastic Pigment and Latex Binders for Paper Coating Applications”, 1998 TAPPI Coating Conference Proceedings, May 2 – 5, 1998, Orlando, Florida.

Lyons, A. and Peshave, C., “Measurement of the Coating Bending Modulus and Its Influence on Final Product Stiffness”, TAPPI Advanced Coating Fundamentals Symposium, pp. 11 – 17, October 7 – 9, 2014, Minneapolis, Minnesota.

Ma, D., Carter, D., and Bousfield, D., “Prediction of Coating Structure Change During Calendering”, TAPPI Advanced Coating Fundamentals Symposium Proceedings, June 11 – 13, 2008, Montreal, Canada.

Nutbeem, C., Preston, J., Hiorns, A., and Husband, J., “The Influence of Kaolin Aspect Ratio on Offset Printability”, PaperCon 2010, May 2 – 5, 2010, Atlanta, Georgia.

Oh, KD., Sim, K., Jung, SY., Youn HJ., Lee, HL., Lee, YM., and Yeu, SU., “Effect of Coating Binder on Fold Cracking of Coater Paper”, PaperCon 2014, April 27 – 30, 2014, Nashville, Tennessee.

Oh, K., Sim, K., Jung, Y. B., Youn, H. J., Lee, H. L., Lee, Y. M., & Yeu, S. U. (2015). Effect of coating binder on fold cracking of coated paper. *Nord. Pulp Pap. Res. J*, 30(2), 360-367.

Oh, KD., Seo, D., Youn, HJ, Lee, YM, Yeu, SU, and Lee, HL, “Effects of Coating Composition and Folding Direction on the Fold Cracking of Coated Paper”, Nordic Pulp and Paper Research Journal, Vol. No. 31, No. 2, 2016.

Okomori, K. and Lepoutre, P., “Effect of Pigment Size and Shape Distribution on the Cohesion of Pigmented Coatings”, 1998 TAPPI Coating Conference Proceedings, May 2 – 5, 1998, Orlando, Florida.

Prall, K, Shaler, S., and LePoutre, P., “Pigmented Latex Coatings: Microstructure and Viscoelastic Mechanical Properties”, Nordic Pulp and Paper Research Journal, Vol. 15, No. 5, pp. 564 – 571, 2000.

Prall, K., “The Viscoelastic Behavior of Pigmented Latex Coating Films”, Doctoral Thesis in Chemical Engineering, University of Maine, Orono, Maine, December 2000.

Preston, J., Husband, J., Norouzi, N., Blair, D., Heard, P., “The Measurement and Analysis of the Distribution of Fountain Solution in Kaolin and Calcium Carbonate Containing Coatings”, PaperCon 2008, May 4 – 7, 2008, Dallas, Texas.

Preston, J., Husband, J., Booth, S., and Coldicott, R., “Binder Depletion During the Coating Process and its Influence on Coating Strength”, PaperCon 2012, April 22 – 25, 2012, New Orleans, Louisiana.

Preston, J., Husband, J., Booth, S., “Binder Depletion During the Coating Process and its Influence on the Coating Failure – A Detailed Analysis of the IGT Dry Pick Test”, 12<sup>th</sup> TAPPI Advanced Coating Fundamentals Symposium, September 10 – 12, 2012, Atlanta, Georgia.

Ratto, P., “Mechanical Properties of Coating Layers”, Journal of Pulp and Paper Science, Vol. 30, No. 12, pp. 335 – 340, 2004.

Rättö, P., & Hornatowska, J. (2010). The influence of coating colour composition on the crack area after creasing. *Nordic Pulp & Paper Research Journal*, 25(4), 488-494.

Rättö, P., Hornatowska, J., Changhong, X., and Terasaki, O., “Cracking Mechanisms of Clay-Based and GCC-Based Coatings”, *Nordic Pulp and Paper Research Journal*, Vol. No. 26, No. 4, pp. 485 – 492, 2011.

Rättö P., Barbier C., Hornatowska J., ”Influence of the distribution of the shape and size distribution of pigment particles on cracking of coating layers”, *Nord. Pulp Paper Res. J.*, vol. 27, no. 4, 714 720, 2012.

Salminen, P., Carlsson, R., Sandas, S., Toivakka, M., Alam, P., and Roper, J., “Combined Modeling and Experimental Studies to Optimize the Balance Between Fold Crack Resistance and Stiffness for Multilayered Paper Coatings – Part 2: Pilot Coater Experimental Studies”, TAPPI/PIMA PaperCon 2008 Conference, May 4 – 7, 2008, Dallas, Texas.

Salminen, P., Carlsson, R., Sandas, S., Toivakka, M., Alam, P., and Roper, J., “Combined Modeling and Experimental Studies to Optimize the Balance Between Fold Crack Resistance and Stiffness for Multilayered Paper Coatings – Part 1: Introduction and Modeling Studies”, TAPPI/PIMA PaperCon 2008 Conference, May 4 – 7, 2008, Dallas, Texas.

Sim, K., Youn, H.J., Oh, K.D., Lee, H.L., Han, C.S., Yeu, S.U. and Lee, Y.M., “Fold Cracking of Coated Paper: The Effect of Pulp Fiber Composition and Beating”, *Nordic Pulp and Paper Research Journal*, Vol 27(2), p.445, 2012.

Stenberg, N., “On the Out-of-Plane Mechanical Behavior of Paper Materials”, Doctoral Thesis, Department of Solids Mechanics, Royal Institute of Technology, Stockholm, Sweden, 2002.

Raman, K., Bousfield, D. W., and Shaler, S. M., “Analyzing the Effects of Binder Content on the Mechanical Properties of Paper Coatings”, 1998 TAPPI Coating Conference Proceedings, May 2 – 5, 1998, Orlando, Florida.

Toivakka, M. and Bousfield, D., “Modeling of Coating Layer Mechanical Properties”, TAPPI Advanced Coating Fundamentals Symposium, pp. 197 – 211, May 4 – 5, 2001, San Diego, California.

Toivakka, M., Alam, P., Touatti, F., Oravilahti, A., Oravilahti, T., Knuutinen, J., Nilsson, R., Pahlevan, M., Ahokas, M., and Wilen, C-E, “Molecular and Microscopic Level Understanding of Coating Strength”, PaperCon 2014, April 27 – 30, 2014, Nashville, Tennessee.

Toivakka, M., Alam, P., Touaiti, F., Oravilahti, A., Oravilahti, T., Knuutinen, J., Nilsson, R., Pahlevan, M., Ahokas, M. and Wilen, C., “Understanding Coating Strength at the Molecular and Microscopic Level”, TAPPI J, Vol. 14(6), pp. 373-383, 2015.

Touaiti, F., Alam, P., Toivakka, M., and Bousfield, D., “Polymer Chain Pinning at Interfaces in CaCO<sub>3</sub> – SBR Latex Composites”, Materials Sciences and Engineering A, Vol. 527, pp. 2363 – 2369, 2010.

Touaiti, F., “Microstructural and Environmental Effects on the Mechanical Properties of Porous Particle Polymer Composites”, Doctoral Thesis in Chemical Engineering, Abo Akademi University, Abo/Turku, Finland, 2013.

Varney, D. and Bousfield, D., “Improved Discrete Element Method Model to Predict Coating Layer Mechanical Properties”, PaperCon 2016, May 16 – 18, 2016, Cincinnati, Ohio.

Varney, D. and Bousfield, D., “Discrete Element Method to Predict Bending and Cracking”, Advanced Coating Fundamentals Symposium, October 4 – 6, 2016, Stockholm, Sweden.

Varney, D. and Bousfield, D., “Discrete Element Method to Predict Coating Failure Mechanisms”, PaperCon 2017, April 23 – 26, 2017, Minneapolis, Minnesota.

Varney, D. and Bousfield, D., “Discrete Element Method to Model Cracking for Two Layer Systems”, PaperCon 2018, April 15 – 18, 2018, Charlotte, North Carolina.

Yang, A., Xie, Y., and Renjung, W., “From Theory to Practice: Improving the Foldcrack Resistance of Industrially Produced Triple Coated Paper”, PaperCon 2011, May 1 – 4, 2011, Covington, Kentucky.

Zhu, Z., Salminen, P., Chen, G., and Toivakka, M., “Mechanical Properties of Pigment Coating Composites Containing Starch”, 13<sup>th</sup> TAPPI Advanced Coating Fundamentals Symposium, October 7 – 9, 2014, Minneapolis, Minnesota.

## APPENDIX

### CONSIDERATION OF ADHESIVE FAILURE

#### A. 1 Adhesive Failure Concept

One of the many ideas that were evaluated was the notion of how the binder fails during the various deformation events (tension or bending). Throughout this thesis, the model assumes that failure is cohesive in nature, meaning that it occurs within the binder bridge itself (when the strain-at-failure calculated by the model exceeds the value for the pure binder films). However, failure most likely also occurs at the interface between the binder and the pigment particles – noted as adhesive failure.

To evaluate this idea, a parameter termed Adhesive Force Factor (AFF) was incorporated in to the model. The maximum stress (noted as  $\sigma_{\max}$ , which is the A value) would be multiplied by this factor. If  $\sigma \leq A * \text{AFF}$ , then the traditional non-linear stress/strain relationship discussed earlier in this thesis would apply [i.e.,  $\sigma = A(1 - e^{-B\varepsilon})$ ]. Otherwise, the stress would be set to zero as failure would be assumed to have occurred. This comparison was done using the model in 2D mode with uniform spherical particles.

The data to which this concept was compared was from Najafi's *et al.* (2016 and 2017) three-point bending experiments. His results for both the 62 and the 78 PVC conditions were compared to the model using the following values for AFF: 0.25, 0.50, 0.75, and 1.00. A value of 1.0 for AFF represents no adhesive failure, which means that the failure is cohesive in nature. Figures A.1 – A.3 below show the comparisons.

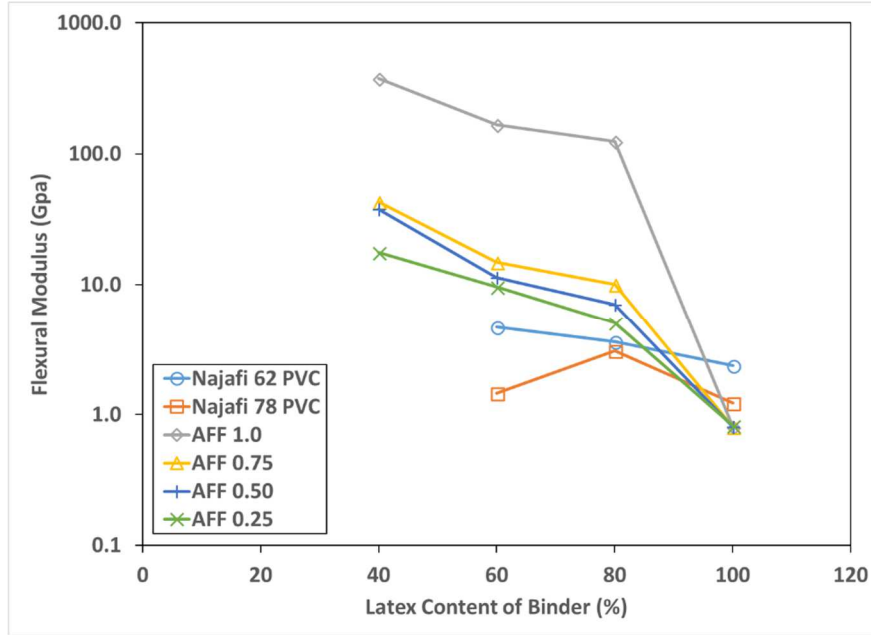


**Figure A.1 Flexural modulus comparison between data of Najafi and the model for various AFF values (three-point bending).**

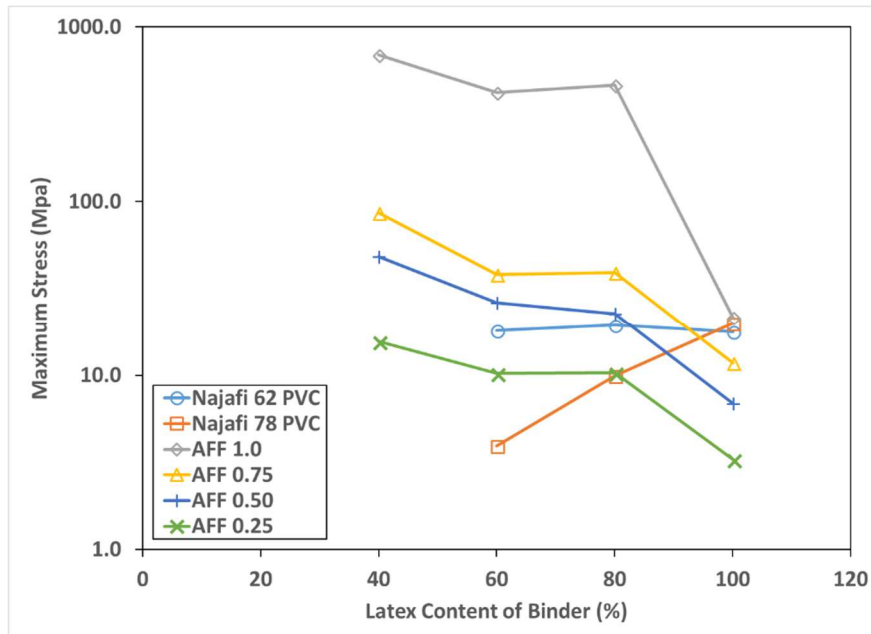


**Figure A.2 Maximum stress comparison between data of Najafi and the model for various AFF values (three-point bending).**

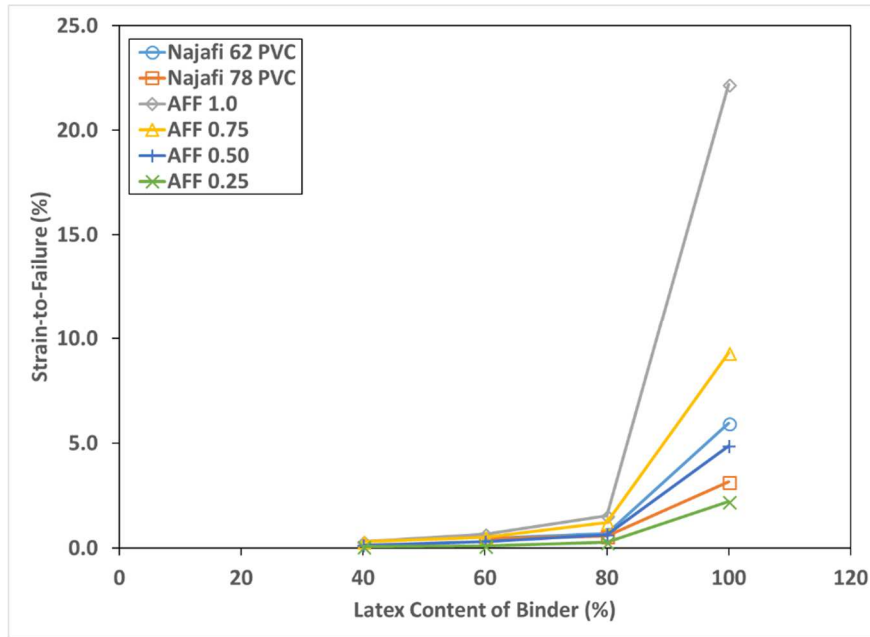


**Figure A.3 Strain-at-failure comparison between data of Najafi and the model for various AFF values (three-point bending).**

These plots show the simulation results come closer to the experimental data when the AFF is used and starch is part of the binder package. For the flexural modulus, the AFF value that comes closest to approximating the data of Najafi is about 0.25. The trends are similar for the maximum stress as values of 0.25 to 0.50 for AFF appear to bring the model results closest to the experimental data. Lastly, the strain-at-failure values are all fairly close, with the AFF of 0.5 appearing to provide the best fit in this case.

Most likely, when starch is present, adhesive failure between the binder bridge and the particles seems to explain the results better than other mechanisms. Each starch level might have a different AFF, but a value of 0.5 seems to work best in these cases.

## **BIOGRAPHY OF THE AUTHOR**

Daniel H. Varney is a married father of one daughter and lives in Vermont. He was born in Waterville, Maine and went to schools in that city before attending the University of Maine in the early 1980s. He graduated with a BS in Chemical Engineering in 1984 and began working for S. D. Warren Company in Westbrook, Maine a few years later. Dan and his wife eventually moved to Vermont for his current job with Omya. He has been performing technical sales to paper companies in the northeast for over 20 years. Along the way, he obtained his MBA degree from a small college in Vermont and then began his current educational pursuits in his early 50s. Dan is a candidate for the Doctor of Philosophy degree in Chemical Engineering from the University of Maine in May 2019.